Atmos. Chem. Phys. Discuss., 14, 769–869, 2014
www.atmos-chem-phys-discuss.net/14/769/2014/
doi:10.5194/acpd-14-769-2014

Atmospheric Chemistry and Physics Discussions

Modelling non-equilibrium secondary organic aerosol formation and evaporation with the aerosol dynamics, gas- and particle-phase chemistry kinetic multi-layer model ADCHAM

P. Roldin[1], A. C. Eriksson[1], E. Z. Nordin[2], E. Hermansson[1], D. Mogensen[3], A. Rusanen[3], M. Boy[3], E. Swietlicki[1], B. Svenningsson[1], A. Zelenyuk[4], and J. Pagels[2]

[1]Division of Nuclear Physics, Lund University, P.O. Box 118, 221 00 Lund, Sweden
[2]Ergonomics and Aerosol Technology, Lund University, P.O. Box 118, 221 00 Lund, Sweden
[3]Department of Physics, P.O. Box 48, University of Helsinki, 00014, Finland
[4]Pacific Northwest National Laboratory, P.O. Box 999, MSIN K8-88, Richland, WA 99354, USA

Received: 13 December 2013 – Accepted: 19 December 2013 – Published: 10 January 2014

Correspondence to: P. Roldin (pontus.roldin@nuclear.lu.se)

Published by Copernicus Publications on behalf of the European Geosciences Union.

ACPD
14, 769–869, 2014

Abstract

We have developed the novel Aerosol Dynamics, gas- and particle-phase chemistry model for laboratory CHAMber studies (ADCHAM). The model combines the detailed gas phase Master Chemical Mechanism version 3.2, an aerosol dynamics and particle phase chemistry module (which considers acid catalysed oligomerization, heterogeneous oxidation reactions in the particle phase and non-ideal interactions between organic compounds, water and inorganic ions) and a kinetic multilayer module for diffusion limited transport of compounds between the gas phase, particle surface and particle bulk phase. In this article we describe and use ADCHAM to study: (1) the mass transfer limited uptake of ammonia (NH_3) and formation of organic salts between ammonium (NH_4^+) and carboxylic acids (RCOOH), (2) the slow and almost particle size independent evaporation of α-pinene secondary organic aerosol (SOA) particles, and (3) the influence of chamber wall effects on the observed SOA formation in smog chambers.

ADCHAM is able to capture the observed α-pinene SOA mass increase in the presence of NH_3(g). Organic salts of ammonium and carboxylic acids predominantly form during the early stage of SOA formation. These salts contribute substantially to the initial growth of the homogeneously nucleated particles.

The model simulations of evaporating α-pinene SOA particles support the recent experimental findings that these particles have a semi-solid tar like amorphous phase state. ADCHAM is able to reproduce the main features of the observed slow evaporation rates if low-volatility and viscous oligomerized SOA material accumulates in the particle surface layer upon evaporation. The evaporation rate is mainly governed by the reversible decomposition of oligomers back to monomers.

Finally, we demonstrate that the mass transfer limited uptake of condensable organic compounds onto wall deposited particles or directly onto the Teflon chamber walls of smog chambers can have profound influence on the observed SOA formation. During the early stage of the SOA formation the wall deposited particles and walls themselves

ACPD
14, 769–869, 2014

serve as a SOA sink from the air to the walls. However, at the end of smog chamber experiments the semi-volatile SOA material may start to evaporate from the chamber walls.

With these three model applications, we demonstrate that several poorly quantified processes, i.e. mass transport limitations within the particle phase, oligomerization, heterogeneous oxidation, organic salt formation, and chamber wall effects can have substantial influence on the SOA formation, lifetime, chemical and physical particle properties, and their evolution. In order to constrain the uncertainties related to these processes, future experiments are needed where as many of the influential variables as possible are varied. ADCHAM can be a valuable model tool in the design and analysis of such experiments.

1 Introduction

Aerosol particles in the atmosphere have substantial impact on the global climate, air quality, and public health. Measurements around the world have demonstrated that a large fraction of the submicron aerosol particles are composed of organic compounds (Jimenez et al., 2009). Today many important biogenic and anthropogenic secondary organic aerosol (SOA) precursors have been identified. However, the scientific knowledge about the SOA formation mechanisms, the SOA composition and properties is still very uncertain (Kroll and Seinfeld, 2008 and Hallquist et al., 2009).

Traditionally, the important SOA formation mechanisms are modelled as pure gas phase oxidation processes followed by equilibrium partitioning between the gas and a liquid organic particle phase (e.g. Pankow, 1994 and Donahue et al., 2011). However, during the last ~ 10 yr other processes occurring in the particle phase have also been identified as important mechanisms for the formation and properties of SOA. These include acid catalysed oligomerization (e.g. Gao et al., 2004; Iinuma et al., 2004; Kalberer et al., 2004, and Tolocka et al., 2004), heterogeneous oxidation reactions (e.g. Knopf et al., 2005; Nash et al., 2006; Rudich et al., 2007; Maksymiuk et al., 2009), or-

ACPD
14, 769–869, 2014

ganic salt formation (e.g. Na et al., 2007; Smith et al., 2010; Kuwata and Martin, 2012 and Yli-Juuti et al., 2013), organosulphate formation (e.g. Liggio and Li, 2006; Surratt et al., 2007) and salting-out effects (e.g. Smith et al., 2011; Bertram et al., 2011). The term salting-out refers to the process in which interactions with dissolved ions (generally inorganic) drive nonpolar organic compounds out of the mixed phase, either into a different organic-rich (liquid) phase or out to the gas phase (Zuend et al., 2011).

Several independent laboratory experiments have also shown that secondary organic aerosol particles can form a solid or semi-solid amorphous phase (e.g. Virtanen et al., 2010; Kuwata and Martin, 2012; Zelenyuk et al., 2012; Vaden et al., 2011; Vaden et al., 2010 and Abramson et al., 2013), at least for relative humidities (RH) below 65 % (Saukko et al., 2012). Recently, Abramson et al. (2013) measured the evaporation rates of pyrene that was imbedded inside SOA particles formed from α-pinene ozonolysis in the presence of pyrene vapour, based on which the authors estimated a diffusion coefficient of 2.5×10^{-17} cm^2 s^{-1} for pyrene in the fresh SOA. For particles aged for $\sim$ 24 h the diffusivity was an additional $\sim$ 3 times slower. Using the Stokes–Einstein relation for the binary diffusion coefficients gives a SOA viscosity of $\sim 10^8$ Pa s for fresh SOA and $\sim 3 \times 10^8$ Pa s for the aged particles. These high viscosity values are typical for tar or pitch like substances (Koop et al., 2011). For a particle with a diameter of 100 nm, this gives a characteristic time of mass-transport (e-folding time of equilibration) of $\sim$ 28 h for fresh SOA and $\sim$ 84 h for the aged SOA particles (Shiraiwa et al., 2011).

If a viscous phase is formed, the mixing within the particle bulk will be kinetically limited and the gas to particle partitioning cannot be well represented by an equilibrium process (Pöschl, 2011), which the traditional partitioning theory assumes (Pankow, 1994). This may not be evident from pure SOA mass formation experiments where the condensable organic compounds are continuously formed by gas phase oxidation of different precursor compounds (see e.g. Odum et al., 1996; Hoffmann et al., 1997; Griffin et al., 1999; Ng et al., 2007; Pathak et al., 2007). However, in the atmosphere the aerosol is exposed to much more variable concentration, temperature and humidity conditions. Hence, the atmospheric aerosol will never be entirely in equilibrium with

ACPD
14, 769–869, 2014

the gas phase. Dzepina et al. (2009) showed that their equilibrium partitioning model substantially overestimate the evaporation of SOA in the Mexico City metropolitan area.

In well controlled laboratory experiments Grieshop et al. (2007) and Vaden et al. (2011) have illustrated that the evaporation of SOA particles formed from α-pinene ozonolysis is a slow process (hours to days). Vaden et al. (2011) showed that this is orders of magnitude slower than expected from equilibrium partitioning. The slow evaporation of SOA can be due to mixing effects, mass transfer limitations, presence of oligomers (Grieshop et al., 2007 and Vaden et al., 2011). Vaden et al. (2011) also illustrated that the evaporation of ambient SOA particles are even slower than for the pure α-pinene SOA and better resembles the evaporation of aged α-pinene SOA particles in the presence of different hydrophobic organic compounds. If the ambient SOA particles studied by Vaden et al. (2011) are representative of typical atmospheric SOA particles, the evaporation due to dilution in the atmosphere (e.g. in urban plumes downwind the source) will be almost negligible. This can increase the lifetime and concentrations of SOA (and e.g. NH_4NO_3) in the atmosphere (Vaden et al., 2011).

For the past decade, large discrepancies between field-measured and model-predicted SOA loadings stimulated an intense research that was mostly focused on the search for additional SOA precursors. However, these models have all treated SOA assuming it to be semi-volatile equilibrated solution. A recent study (Shrivastava et al., 2013) shows that it is possible to improve agreement between measured and modelled SOA loadings by treating SOA, in accord with experimental data as a non-volatile, semi-solid. Similarly, considering the highly viscous, non-volatile nature of SOA offers a simple explanation for the observed long-range transport of persistent organic pollutants by atmospheric particles (Zelenyuk et al., 2012).

A number of model studies have been performed to explore detailed gas phase reaction mechanisms which can be responsible for the SOA formation of known biogenic and anthropogenic SOA precursors (e.g. Bloss et al., 2005a, b; Johnson et al., 2005 and 2006; Li et al., 2007; Hu et al., 2007; Metzger et al., 2008; Rickard et al., 2010; Camredon et al., 2010 and Valorso et al., 2011). However, relatively few at-

ACPD
14, 769–869, 2014

tempts have been made to perform detailed process-based modelling on the influence of phase state (Shiraiwa et al., 2010, 2011 and 2012; Pfrang et al., 2011), oligomerization (Vesterinen et al., 2007; Pun and Seigneur, 2007; Li et al., 2007; Hu et al., 2007; Ervens and Volkamer, 2010), heterogeneous oxidation mechanisms (Shiraiwa et al., 2010, 2011 and 2012; Pfrang et al., 2011), organic-inorganic interactions (e.g. salting-out effects, acidity effects) (Zuend et al., 2010, and Zuend and Seinfeld, 2012), organic salt formation (Barsanti et al., 2009), and non-equilibrium gas-particle partitioning and aerosol dynamics (e.g. Korhonen et al., 2004; Vesterinen et al., 2007; Boy et al., 2006, and Roldin et al., 2011a, b) on the SOA formation and properties, and to our knowledge no one has previously included all these processes in the same model.

In this article we describe and apply a newly developed aerosol dynamics and gas- and particle- phase chemistry model for chamber studies (ADCHAM). As the name implies the model is primarily aimed to be used as a flexible tool for evaluation and design of controlled experiments in smog chambers (e.g. Nordin et al., 2013), thermodenuders (e.g. Riipinen et al., 2010), evaporation chambers (e.g. Vaden et al., 2011), flow-tube reactors (e.g. Jonsson et al., 2008) or hygroscopicity measurements set-ups (e.g. Svenningsson et al., 2006). However, the overall aim is to gain better understanding of which processes (e.g. gas phase chemistry, particle phase reactions, particle phase state, aerosol water uptake, cloud droplet activation, and aerosol dynamics) are relevant for the aerosol properties and formation in the atmosphere.

In the future, we intend to use this knowledge, to develop the ADCHEM model (Roldin et al., 2011a). ADCHEM is a 2-D-Lagrangian model for Aerosol Dynamics, gas phase CHEMistry and radiative transfer which has been used for urban plume studies (Roldin et al., 2011b). One of the main purposes with ADCHEM is to improve the sub-grid scale aerosol particle representation in large-scale chemistry transport models (e.g. Bergström et al., 2012). In the first version of ADCHEM aging of the organic compounds in the atmosphere was simulated with a non-equilibrium 2-D-VBS approach. The 2-D-VBS method treats the oxidation of organic compounds in a simplified way by

ACPD
14, 769–869, 2014

generalized OH reactions rates, functionalization and fragmentation patterns (Jimenez et al., 2009; Roldin et al., 2011a and Donahue et al., 2011).

In ADCHAM the secondary aerosol formation is instead modelled by combining the Master Chemical Mechanism version 3.2 (MCMv3.2) (Jenkin et al., 1997, 2003; Saunders et al., 2003) and an updated version of the aerosol dynamics and particle phase chemistry module from ADCHEM, which now considers acid catalysed oligomerization, oxidation reactions in the particle phase (e.g. secondary ozonide formation) and the diffusion limited transport of compounds between the gas phase, particle surface and particle bulk phase. In this work we test the capability of ADCHAM to simulate (1) the mass transfer limited uptake of NH_3 and formation of organic salts between ammonium and carboxylic acids (Na et al., 2007 and Kuwata and Martin, 2012), (2) the slow and almost particle size-independent evaporation of α-pinene SOA particles (Vaden et al., 2011), and (3) the influence of heterogeneous reactions on the SOA formation and properties.

Regional and global scale chemistry transport models (e.g. the EMEP model (Bergström et al., 2012) rely on semi-empirical parameterizations for the SOA formation (e.g. VBS) derived from smog chamber experiments. This is one of many reasons why it is important to constrain the uncertainties related to specific chamber effects. Hence, as a final application, we illustrate how ADCHAM can be used to study the influence of chamber wall effects on the SOA mass formation, particle number size distribution and gas phase chemistry during a *m*-xylene oxidation experiment from Nordin et al. (2013).

2 Model description

ADCHAM consist of:

1. a detailed gas phase kinetic code (in this work with reactions from MCMv3.2),

ACPD
14, 769–869, 2014

2. an aerosol dynamics code (Roldin et al., 2011a) which include Brownian coagulation, homogeneous nucleation, dry deposition to chamber walls and a detailed condensation/evaporation algorithm,

3. a novel particle phase chemistry module which is closely connected to the condensation/evaporation algorithm and,

4. a kinetic multi-layer model which treats the diffusion of compounds between the particle surface and several bulk layers, analogous to Shiraiwa et al. (2010).

Figure 1 shows a schematic picture of the ADCHAM model structure. The model explicitly treats the bulk diffusion of all compounds (including O_3 and potentially other oxidation agents) between different particle layers and bulk reactions. For all compounds except O_3 the gas-surface exchange is modelled with a condensation/evaporation equation which considers the gas-surface diffusion limitations and non-unity sticking probability at the surface layer (surface mass accommodation) (Eq. 1). In each particle layer the model considers acid catalysed oligomerization, equilibrium reactions between inorganic and organic salts and their dissolved ions, and oxidation of SOA with O_3.

In ADCHAM the different processes are solved with separate modules using operator splitting. For each main model time step (in this work 10 s) ADCHAM considers homogeneous nucleation, followed by dry deposition of particles (Sect. 2.2.3) and potentially gases, emissions of gases and particles, gas phase chemistry (Sect. 2.1) and coagulation (Sect. 2.2.2). After this ADCHAM handles the condensation and evaporation of all organic and inorganic compounds (Sect. 2.2.1) and the uptake, diffusion and reactions of O_3 in the different particle layers (Sect. 2.4.2). For these processes ADCHAM uses a much shorter internal time step (in this work 1–10 ms). The gas-particle partitioning rely upon updated activity coefficients (Sect. 2.3.1), hydrogen ion concentrations (Sect. 2.3.2), water content, concentrations of inorganic and organic salts (Sect. 2.3.3) and their corresponding anion and cations. Therefore, the gas-particle partitioning is usually the most time demanding process in ADCHAM. Finally, the model considers the

ACPD
14, 769–869, 2014

diffusion of organic and inorganic compounds between all particle layers (Sect. 2.4.1) and acid catalysed oligomerization (Sect. 2.3.4).

2.1 Gas phase chemistry

To be able to implement the detailed MCMv3.2 gas phase chemistry together with user specified reactions and reaction rates (e.g. chamber wall effects) in a computationally efficient way in MATLAB, we constructed a program which automatically creates a system of equations which can be used to calculate the concentrations of the user specified compounds. The only required input to the program is the MCMv3.2 names of the compounds which can be downloaded at http://mcm.leeds.ac.uk/MCM. The output from the program is a set of coupled ordinary differential equations (one for each compound) and the Jacobian matrix which is used by the ode15s solver in MATLAB. The constructed code can either be used as a standalone code for separate gas phase chemistry simulations, or used as a module in the ADCHEM or ADCHAM model. The ode15s solver in MATLAB is intended to be used for stiff ordinary differential equation systems. The solver uses an adaptive and error tolerance controlled internal time step in order to solve the gas phase chemistry.

In Sects. 3.2 and 3.3 we simulate the SOA formation from ozonolysis of α-pinene in the presence of CO or cyclohexane as OH scavenger. We constructed an equation system consisting of all MCMv3.2 reactions involving inorganic gas phase chemistry and all oxidation products of α-pinene and cyclohexane (in total 668 compounds and 2093 reactions). In Sect. 3.4 we also model the SOA formation oxidation of *m*-xylene with the MCMv3.2 gas phase chemistry (273 compounds and 878 reactions).

2.2 Aerosol dynamics

The aerosol dynamics module in ADCHAM is based on the aerosol dynamics code from the ADCHEM model (Roldin et al., 2011a). A shorter description with focus on the important updates is given below.

ACPD
14, 769–869, 2014

2.2.1 Condensation and evaporation

In ADCHAM the gas-particle partitioning depends on the chemical composition in the particle surface layer. Dissolution of ammonia into the particle water and/or organic phase surface layer is treated as an equilibrium process, considered after the diffusion limited condensation/evaporation of HNO_3, H_2SO_4 and organic compounds (Eq. 1) (of which carboxylic acids influence the particle acidity and hence the ammonia dissolution).

$$I_i = 2D_i D_\mathrm{p} f_i(Kn_i, \alpha_{\mathrm{s},i})(C_{i,\infty} - C_{i,\mathrm{s}}),$$
$$f_i(Kn_i, \alpha_{\mathrm{s},i}) = \frac{0.75\alpha_{\mathrm{s},i}(1 - Kn_i)}{Kn_i^2 + Kn_i + 0.283Kn_i\alpha_{\mathrm{s},i} + 0.75\alpha_{\mathrm{s},i}} \quad (1)$$

In Eq. (1) I_i is the contributions of species i to the particle molar growth rates, f_i is the Fuchs-Sutugin correction factor in the transition region, $C_{i,\infty}$ is the gas phase concentration of species i far from the particle surface (mol m^{-3} air), $C_{i,\mathrm{s}}$ is the saturation gas phase concentration at the particle surface, D_i is the gas phase diffusion coefficient, D_p is the particle diameter, Kn_i is the non-dimensional Knudsen number and $\alpha_{\mathrm{s},i}$ is the surface mass accommodation coefficient.

In this work we estimate the pure-liquid saturation vapour pressures (p_0) of the MCMv3.2 oxidation products using either the group contribution method SIMPOL (Pankow and Asher, 2008) or the method by Nannoolal et al. (2008) (here referred to as the Nannoolal method). The corresponding equilibrium vapour pressures ($p_{\mathrm{s},i,j}$) for each particle size bin (j) are derived with Raoult's law, using the mole fractions of each organic compound ($x_{i,j}$), the activity coefficients ($\gamma_{i,j}$) calculated with the AIOMFAC thermodynamic model (Zuend et al., 2008 and 2011) (Sect. 2.3.1), and the Kelvin effect ($C_{k_{i,j}}$) (Eq. 2). The surface tension (σ_i) of the organic compounds were assumed

ACPD
14, 769–869, 2014

to be 0.05 Nm^{-1} following Riipinen et al. (2010).

$$p_{s,i,j} = p_{0,i} x_{i,j} \gamma_{i,j} C_{k_{i,j}}, \quad C_{k_{i,j}} = e^{\left(\frac{4M_i\sigma_i}{RT\rho_p D_{p,j}}\right)} \tag{2}$$

T is the temperature in Kelvin, R is the universal gas constant ($\mathrm{J\,mol^{-1}\,K^{-1}}$), M_i is the molar mass of compound i and ρ_p is the density of the phase which the compound partition to.

The mole fraction for compound i in Eq. (2) is the mole fraction of the organic compound in the surface layer organic phase which compound i partitions into (dissolves). In this article we either treat all SOA (monomers + oligomers + organic salts) as one phase or as two completely separated phases. Hence, if the model treats the oligomers and organic salts as a separate phase, then this material has no influence on the saturation vapour pressures of the monomers (Eq. 2). However, adsorption of low-volatility oligomers at the surface layer still affects the gas-particle partitioning of monomer SOA, by altering the surface mass accommodation (Sect. 2.4.1) and by decreasing the monomer SOA fraction in the surface layer.

In this work the condensation and evaporation mechanism includes all organic compounds with modelled pure-liquid saturation vapour pressures less than 1 Pa. For the α-pinene oxidation experiments which we model in Sects. 3.2 and 3.3 this involves 154 non-radical MCMv3.2 organic compounds, while for the m-xylene SOA formation experiment modelled in Sect. 3.4 we consider 112 condensable organic MCMv3.2 compounds.

2.2.2 Coagulation

ADCHAM also includes a Brownian coagulation algorithm (Roldin et al., 2011a). However, it still remains a challenge to combine the coagulation algorithm with the kinetic multilayer model, when the number of particle layers depends on the particle size. In this first version of ADCHAM it is only possible to treat coagulation between particles

ACPD
14, 769–869, 2014

composed of maximum three layers (e.g. a surface monolayer layer, a bulk layer and a seed aerosol core). When two particles composed of such a layer structure collide the layers are simply assumed to merge together forming a new spherical particle with a surface layer, a bulk layer and a seed aerosol core. Because the surface area of the formed particle is always less than the sum of the surface areas of the two original particles the width of the surface layer increases. Hence, in order to keep the width of the surface layer at approximately the thickness of one monolayer, part of the surface layer material (by default with identical composition as the remaining surface layer) is transferred to the particle bulk.

2.2.3 Dry deposition and chamber wall effects

It is well known that dry deposition losses of particles onto the chamber walls have large influence on many chamber experiments (see e.g. Pierce et al., 2008). A commonly used method (see e.g. Hildebrandt et al., 2009 and Loza et al., 2012) is to scale the formed SOA mass with the measured relative seed aerosol (typically ammonium sulphate) loss rate. With this method it is assumed that the particles deposited on the chamber walls continue to take up SOA as if they were still present in the gas phase. A second method which was also used by Hildebrandt et al. (2009) and Loza et al. (2012) is to assume that once the particles have deposited on the chamber walls the gas-particle partitioning stops. These two correction methods can be considered to be two extremes, where the first method gives an upper bound of the SOA mass formed during the experiments while the second method gives a lower bound of the SOA formed during the experiments (at least if the SOA particles on the chamber walls are not evaporating and the gas phase losses directly to the chamber walls are negligible).

ADCHAM considers the dry deposition of particles onto chamber walls and also keeps track of the particles deposited on the walls. The model also treats the mass transfer limited gas to particle partitioning between the gas phase and the wall deposited particles. Hence, ADCHAM can be used to study the influence of chamber

ACPD
14, 769–869, 2014

wall effects on the SOA mass formation and help constraining the uncertainties of the formed SOA mass (SOA mass yield).

For non-charged particles, ADCHAM uses the indoor dry deposition loss rate model from Lai and Nazaroff (2000) which accounts for different dry deposition loss rates on upward, downward and vertical facing surfaces. However, if a considerable fraction of the particles are charged (e.g. at Boltzmann charge equilibrium) the effective dry deposition loss rate of particles can be considerably enhanced (Pierce et al., 2008). Hence, in order to be able to model realistic dry deposition loss rates of charged particles, ADCHAM keeps track of the fraction of particles suspended in the air with zero, one, two or three elemental charges in each particle size bin. The first order deposition loss rate (s^{-1}) due to charge (k_{charge}) is calculated with Eq. (3) where v_e is the characteristic average deposition velocity due to electrostatic forces ($m\ s^{-1}$) (McMurry and Rader, 1985). The dry deposition loss rates depend on the friction velocity and for charged particles also on the mean electrical field strength within the chamber ($\overline{E}$). Unfortunately both of these parameters are usually poorly known and need to be estimated.

McMurry and Rader (1985) found that $\overline{E}$ was $\sim 45\,V\,cm^{-1}$ in an almost spherical $\sim 0.25\,m^3$ Teflon chamber. On the chamber surfaces they measured a negative electrical field strength of $-300 \pm 150\,V\,cm^{-1}$. They attributed the lower empirically derived electric field within the chamber to the fact that the particles in the bag will be influenced by a net electrical field, which has contributions from all points on the chamber surfaces. Hence, the shape and size of the chamber will also influence the mean electrical field.

$$k_{charge} = \frac{A_{chamber} v_e}{V_{chamber}}, \quad v_e = \frac{neC_c\overline{E}}{3\pi\mu D_p} \tag{3}$$

$A_{chamber}$ is the chamber surface area, $V_{chamber}$ is the chamber volume, n is the number of elemental charges of the particle, e is the elementary charge, C_c is the Cunningham slip correction factor and μ is the dynamic viscosity of air.

ACPD
14, 769–869, 2014

The mass transfer limited uptake of gases to and from the chamber walls need to be considered in order to take into account the potential uptake (dissolution) of organic compounds in the SOA particles deposited on the chamber walls (Hildebrandt et al., 2009), as well as direct uptake of gas phase molecules onto the Teflon chamber surfaces (Matsunaga and Ziemann, 2010). For the condensation uptake or evaporation loss of SOA from the particles deposited on the walls, we assume that the particles deposited on the walls behave as if they were still suspended in (direct contact with) a thin (1 mm) air layer adjacent to the chamber walls. As more particles get deposited on the walls, the SOA concentration on the chamber wall will increase. The condensable organic compounds in the thin air layer next to the chamber walls then have an increased probability to dissolve into the organic particle phase on the walls. However, semivolatile organic compounds may also evaporate from the particles on the walls, when the gas-phase concentrations in the chamber are reduced. The gas-particle partitioning between the wall-deposited particles and the thin air layer next to the chamber walls is modelled with the condensation and evaporation module described in Sect. 2.2.1.

ADCHAM also considers the adsorption and desorption of condensable organic compounds onto the Teflon surface film. This is modelled as a reversible process in accordance with Matsunaga and Ziemann, 2010. The adsorption of gas phase organic compounds onto the chamber walls is represented by a first order loss rate from the near wall gas phase to the walls ($k_{g,w}$). The desorption rate from the Teflon surfaces out to the thin layer next to the chamber walls ($k_{w,g,i}$) depends on the pure-liquid saturation vapour pressures ($p_{0,i}$) of the adsorbed compounds (Eq. 4) (Matsunaga and Ziemann, 2010). Equations (5) and (6) describe the rate of change of the organic compound (X_i) (due to adsorption and desorption) on the chamber walls and in the air layer adjacent to the wall, respectively. [$X_{i,g,w}$] is the concentrations of compound X_i in the thin layer adjacent to the chamber walls. The concentration at the chamber wall ([$X_{i,w}$]) is given as an effective chamber volume concentration (total number of X_i molecules on the walls divided by the total chamber volume ($V_{chamber}$)).V_{wall} is the air volume of the thin (1 mm) layer adjacent to the chamber walls, C_w is an effective wall equivalent mass

ACPD
14, 769–869, 2014

concentration which the organic compounds can dissolve into, M_w is the average molar mass of the Teflon film, and $\gamma_{w,i}$ is the activity coefficient of compound i in the Teflon film. $k_{g,w}$ and $C_w/(M_w\gamma_{w,i})$ in Eq. (4) was experimentally determined by Matsunaga and Ziemann (2010) for *n*-alkanes, 1-alkenes, 2-alcohols and 2-ketones to 9, 20, 50 and 120 µmol m^{-3}, respectively.

$$k_{w,g,i} = \frac{k_{g,w}}{(RT/p_{0,i}C_w/(M_w\gamma_{w,i}))} \quad (4)$$

$$\frac{d[X_{i,w}]}{dt} = (k_{g,w}[X_{i,g,w}] - k_{w,g,i}[X_{i,w}])\frac{V_{wall}}{V_{chamber}} \quad (5)$$

$$\frac{d[X_{i,g,w}]}{dt} = -k_{g,w}[X_{i,g,w}] + k_{w,g,i}[X_{i,w}] \quad (6)$$

A compound with $p_0 = 2.5 \times 10^{-2}$ Pa and $C_w/(M_w\gamma_{w,i}) = 10$ µmol m^{-3}, partitions ∼ 50 % to the gas phase and ∼ 50 % to the chamber walls, at equilibrium and room temperature Eq. (4). At equilibrium, compounds with a vapour pressure $< 10^{-3}$ Pa and $C_w/(M_w\gamma_{w,i}) > 10$ µmol m^{-3} will almost exclusively be found at the walls, if they are not able to form SOA rapidly enough. Hence, the SOA formation in the smog chamber will depend on: Eq. (1) the formation rate of condensable organic compounds, Eq. (2) the particle deposition losses, Eq. (3) the magnitude of the condensation sink to the particles in the air and onto the chamber walls, and Eq. (4) the diffusion limited uptake onto the chamber walls and particles on the walls.

The concentration gradient in the laminar layer adjacent to the chamber walls generally drives condensable gas phase components from the well mixed chamber volume to the chamber walls (thin model layer next to the wall). We explicitly model this mass transfer with Fick's first law of diffusion, assuming a linear concentration gradient across the laminar layer next to the chamber wall (see Fig. 2).

The width of the laminar layer was used as a model fitting parameter. The gas phase chemistry and the gas to particle mass transfer (condensation) in the well mixed cham-

ACPD
14, 769–869, 2014

ber volume and in the thin layer adjacent to the chamber wall were solved using operator splitting with a model time step of 10 ms. The mass transfer between the well-mixed chamber volume and the thin layer next to the chamber wall was modelled with a time step of 0.1 ms. The model needs to take short time steps because of the large condensation sink (or evaporation source) of the wall deposited particles and the Teflon surfaces which may rapidly alter the concentrations in the thin air layer next to the chamber walls.

2.2.4 Size distribution structures

Analogous to ADCHEM (Roldin et al., 2011a) ADCHAM include several methods (full-stationary, full-moving and moving-centre) in order to treat the changes in the particle number size distribution upon condensation/evaporation or coagulation. These methods are all mass and number conserving and have different advantages and disadvantages (Korhonen et al., 2004; Jacobson, 2005 and Roldin et al., 2011a). For all simulations performed in this article, we have used the full-moving method where the diameter grid moves with the particles. Hence, this method has no numerical diffusion problems when particles grow by condensation or evaporate. Homogeneous nucleation is considered by adding new particle size bins when new particles are formed (Sects. 3.2 and 3.3).

2.3 Particle phase chemistry

2.3.1 Activity coefficients and organic-inorganic interactions

The AIOMFAC model is based on the UNIFAC model for organic mixtures but also considers organic-inorganic interaction which allows us to study salt-effects on the SOA formation. AIOMFAC considers interactions between 12 different ions (including NH_4^+, NO_3^-, H^+, SO_4^{2-} and HSO_4^-) and alkyls, hydroxyls, carboxyls, ketones, aldehydes, ethers, esters, alkenyls, aromatic carbon-alcohols and aromatic hydrocarbons

ACPD
14, 769–869, 2014

(Zuend et al., 2008 and 2011). For other important functional groups i.e. nitrates, nitros, PANs and peroxides no ion-organic functional group interaction parameterizations are available. Hence, for these functional groups we only consider organic-organic functional group interactions. In total the model considers 52 different UNIFAC functional subgroups, with interaction parameters from Hansen et al. (1991), except for alcohols (Marcolli and Peter, 2005) and nitrates, PANs and peroxides for which we use the parameterization from Compernolle et al. (2009). In ADCHAM, the activity coefficients are calculated before the condensation algorithm is used and when updating the hydrogen ion concentration ($[H^+]$) for the acid catalysed oligomerization.

2.3.2 Acidity and dissociation of inorganic compounds in organic rich phases

The hydrogen ion concentration is calculated in the condensation algorithm and when considering acid catalysed oligomerization. Analogous to the procedure in ADCHEM (Roldin et al., 2011a) $[H^+]$ in the particle water or particle water + organics phase is calculated by solving the ion balance equation (Eq. 7). In ADCHAM we have extended the ion balance equation with dissociation products of carboxylic acids ($RCOO^-$). In this work we assume that all carboxylic acids have identical dissociation constants (see Sect. 3.2). Hence, $[RCOO^-]$ in Eq. (7) represent the total concentration (mol kg^{-1} solvent) of dissociated carboxylic acids.

$$[H^+] + [NH_4^+] + [Na^+] = [NO_3^-] + 2[SO_4^{2-}] + [HSO_4^-] + [Cl^-] + [OH^-] + [HCO_3^-] + 2[CO_3^{2-}] + [RCOO^-] \quad (7)$$

In order to calculate $[H^+]$, all concentrations except the hydrogen ion concentration in Eq. (7) is replaced with known equilibrium coefficients, activity coefficients from AIOMFAC, and the total concentration of dissolved dissociated and non-dissociated compounds, $([RCOOH] + [RCOO^-])$, $([NH_3(aq)] + [NH_4^+])$, $([SO_4^{2-}] + [HSO_4^-])$, $([HNO_3] + [NO_3^-])$ and $([HCl(aq)] + [Cl^-])$. In this work the uptake of

ACPD
14, 769–869, 2014

CO_2 in the particles was treated as an equilibrium process. The HCO_3^- and CO_3^{2-} concentrations depend on the hydrogen ion concentration and the CO_2 partial pressure (390 ppbv). When all unknown ion concentrations have been replaced with the known parameters, Eq. (7) becomes an 8th order polynomial with $[H^+]$ as the only unknown variable. The hydrogen ion concentration is given by the maximum real root of this polynomial.

To treat the CO_2 uptake as an equilibrium process may not be realistic if the particles are very viscous (see Sect. 1). However, the estimated diffusion coefficients of other small "guest" molecules (e.g. O_3, OH and H_2O) in an amorphous glassy organic matrix is in the order of 10^{-10}–10^{-12} $cm^2\,s^{-1}$ at room temperature (Koop et al., 2011; Zobrist et al., 2011). This gives corresponding e-folding times of equilibration for submicron particles in the range of seconds.

All experiments which we model in this paper were performed at dry conditions (RH ≤ 5 %). For the α-pinene SOA experiments (Sects. 3.2–3.3), the modelled particle water mass content is only ∼ 0.4 % at a RH of 5 %. For these particles the solvent will therefore mainly be the organic compounds and not water. Hence, in this work the concentrations of the inorganic ions (including H^+) is not given for the aqueous but for the combined organics and water phase. Henry's law coefficients (K_H) and dissociation rates (K_a) of the inorganic compounds and carboxylic acids, are (if at all) usually only available for aqueous solutions. However, there is often a relationship between the ΔpK_a ($-\log_{10}(K_{a,\,base}) + \log_{10}(K_{a,\,acid})$) and the proton transfer between the Brønsted acid and the Brønsted base, in protic ionic liquids (Greaves and Drummond, 2008). Thus, we will use the aqueous dissociation rates and Henry's law coefficients for the organic amorphous SOA and water mixtures, and take into account the non-ideal interactions between the ions, organic solvents and water using AIOMFAC (Sect. 2.3.1).

With these assumptions in mind, the modelled absolute values of $[H^+]$ should be interpreted with caution. However, we believe that the model can give a realistic representation of the relative influence of different types of dissolved compounds on the particle acidity. For instance, carboxylic acids will most likely increase $[H^+]$ also in an

ACPD
14, 769–869, 2014

organic rich phase, while dissolved ammonia will decrease $[H^+]$. For all other organic compounds except the carboxylic acids, the dissociation rates were assumed to be equal to that of pure water ($pK_a = 14$). Hence, equivalent to aqueous solutions the acidity will mainly be governed by the carboxylic acids and inorganic compounds.

2.3.3 Inorganic and organic salt formation

In ADCHAM the inorganic salts $(NH_4)_2SO_4$, NH_4HSO_4 and NH_4NO_3 and the organic salts of ammonium and different carboxylic acids (NH_4RCOO) can be considered to form. All these salts contain NH_4^+ and which of these salts that will be formed depend on the solubility constants, the ammonium concentration, the concentration of the different anions and the activity coefficients. Because all these salts contain ammonium the salt which forms first will limit the formation of other salts. In this work, we only simulate experiments performed on pure organic particles or organic particles which take up NH_3(g). Hence, NH_4RCOO(s) was the only (solid) salt which was considered to be formed in the particle organics-water phase. The solid salt concentrations are updated iteratively every time step which the condensation/evaporation algorithm is used.

When updating the NH_4RCOO(s) concentration, ADCHAM starts by estimating the activity coefficients and the hydrogen ion concentration (Eq. 7). After this non-equilibrium NH_4^+ and $RCOO^-$ concentrations ($[NH_4^+]^*$ and $[RCOO^-]^*$) can be derived, and the total concentrations of NH_4 ($[NH_{4,tot}] = [NH_4^+]^* + [NH_4RCOO]_{t-1}$) and RCOO ($[RCOO_{tot}] = [RCOO^-]^* + [NH_4RCOO]_{t-1}$) are estimated. These values are then inserted into the solubility product equation (Eq. 8). Rearranging Eq. (8) gives a second order polynomial where the new NH_4RCOO concentration ($[NH_4RCOO]_t$) is given by the smallest positive real root. Finally the NH_4^+ and $RCOO^-$concentrations are updated and the iteration starts from the beginning by deriving the hydrogen ion concentration again. The iteration proceeds until the relative change in the NH_4^+, $RCOO^-$ and

ACPD
14, 769–869, 2014

H^+ concentrations all are less than 10^{-3} between one iteration step.

$$K_{NH_4RCOO} = \gamma_{NH_4}\gamma_{RCOO}\left[NH_4^+\right]\left[RCOO^-\right] = \gamma_{NH_4}\gamma_{RCOO}\left([NH_{4,tot}] - [NH_4RCOO]\right)\left(RCOO_{tot} - [NH_4RCOO]\right) \quad (8)$$

2.3.4 Acid catalysed oligomerization

Any oligomerization mechanisms in the gas phase, particle phase or on the particle surfaces (including different functional groups, ozonolysis, acid catalysed reactions, and radicals), can easily be implemented in ADCHAM. In this work we consider six different oligomerization mechanisms (R1–R6) which have been listed as possible reaction pathways for oligomer formation in the overview by Hallquist et al. (2009). Currently ADCHAM only considers the reactions between monomers which form dimers and not the possible reactions between dimers and dimers with monomers.

$$\text{hydroperoxides(p)} + \text{aldehydes(p)} \overset{H^+}{\leftrightarrow} \text{peroxyhemiacetals(p)} \quad \text{(R1a)}$$

$$\text{hydroperoxides(p.s.)} + \text{aldehydes(g)} \overset{H^+}{\leftrightarrow} \text{peroxyhemiacetals(p.s.)} \quad \text{(R1b)}$$

$$\text{aldehydes(p)} + \text{aldehydes(p)} \overset{H^+}{\leftrightarrow} \text{aldol reaction prod.(p)} \quad \text{(R2a)}$$

$$\text{aldehydes(p.s.)} + \text{aldehydes(g)} \overset{H^+}{\leftrightarrow} \text{aldol reaction prod.(p.s.)} \quad \text{(R2b)}$$

$$\text{alcoholes(p)} + \text{aldehydes(p)} \overset{H^+}{\leftrightarrow} \text{hemiacetals(p)} \quad \text{(R3)}$$

$$\text{alcoholes(p)} + \text{carboxylic acids(p)} \overset{H^+}{\leftrightarrow} \text{esters(p)} + H_2O\text{(p)} \quad \text{(R4)}$$

$$RO_2\text{(g)} + RO_2\text{(g)} \leftrightarrow \text{ROOR-type peroxides(g)} \quad \text{(R5)}$$

$$\text{carbonyls(p)} + \text{carbonyls(p)} + O_3\text{(p)} \leftrightarrow \text{secondary ozonides(p)} \quad \text{(R6)}$$

The notation within the brackets denotes weather the compounds are in the gas phase (g), particle phase (p) or particle-surface layer (p.s.) upon reaction. If H^+ is included in the reaction, the formation of oligomer is acid catalysed, which is generally the case in

ACPD
14, 769–869, 2014

the particle phase (Hallquist et al., 2009). The acid catalysed formation rate of a dimer can generally be considered to be proportional to the hydrogen ion concentration (see e.g. schemes by Tolocka et al., 2004 and Iinuma et al., 2004). ADCHAM explicitly treats the formation and the degradation of dimers back to monomers as separate reactions (R7 and R8) and not as an equilibrium process.

$$\text{monomer}_j + \text{monomer}_i \rightarrow \text{dimer}_{ji} \quad \text{(R7)}$$

$$\text{dimer}_{ji} \rightarrow \text{monomer}_j + \text{monomer}_i \quad \text{(R8)}$$

The acid catalysed dimer formation rates in the particle bulk phase ($F_f(p)$) or particle surface ($F_f(p.s.)$) between monomer i and j depend on a reaction specific formation rate constant (k_f) and the hydrogen ion concentration (c_{H^+}) (Eqs. 9 and 10). The dimer formation rate in the particle surface layer formed between compound j found in the gas phase and compound i found at the particle surface is treated as a reactive uptake. The dimer degradation rate in the particle bulk or at the particle surface ($F_d(p)$ and $F_d(p.s.)$) simply depends on the dimer concentration and a dimer specific degradation reaction rate constant (k_d) (Eqs. 11 and 12).

$$F_f(p) = k_f(p) c_{H^+}(p) c_{m,i}(p) c_{m,j}(p) \quad (9)$$

$$F_f(p.s.) = k_f(p.s.)\, c_{H^+}(p.s.) c_{m,i}(p.s.) c_{m,j}(g) \quad (10)$$

$$F_d(p) = k_d(p) c_{d,i}(p) \quad (11)$$

$$F_d(p.s.) = k_d(p.s.) c_{d,i}(p.s.) \quad (12)$$

The temporal evolution of the dimer and monomer concentrations (c_d and c_m) in the particle bulk layers and surface layer are derived with a kinetic model. This code solves a coupled ordinary differential equation system, consisting of one ordinary differential equation for each SOA monomer (Eq. 13), and one ordinary differential for each dimer (Eq. 14). The equations are given by the sum of all dimer degradation and formation

ACPD
14, 769–869, 2014

rates for the individual reactions which each compound i is involved in.

$$\frac{dc_{m,i}}{dt} = \sum_{k=1}^{Z} F_{d,i,k} x_{m,i} - \sum_{k=1}^{N} F_{f,i,k} \quad (13)$$

$$\frac{dc_{d,i}}{dt} = -\sum_{k=1}^{P} F_{d,i,k} + \sum_{k=1}^{Q} F_{f,i,k} x_{d,i} \quad (14)$$

In order to not end up with an enormous coupled ordinary differential equation system, the different dimers are classified into 7 different categories depending on the type of reaction (R1a–R5). Secondary ozonide formation (R6) is treated by a separate kinetic multilayer module for ozone uptake, diffusion and reactions with SOA (see Sect. 2.4.2). In order to be mass conserving the number of moles of dimer formed is corrected with the molar ratio (x_d) between the molar mass of the product(s) and the sum of the molar masses of the reacting compounds. In ADCHAM all dimers have by default a molar mass of 400 g mol^{-1}. When we lump the dimers into different categories the information about their exact chemical composition and origin are lost. This can be a problem when considering the reversible reactions back to monomers. In this work we have assumed that the dimer SOA is converted back to the different monomers with fractions (x_m) corresponding to the (current time step) relative abundance of each monomer SOA compound which is involved in the dimer formation. This is a reasonable assumption if the monomer SOA composition does not change substantially on a time scale longer than the lifetime of the dimer.

The modelled relative amount and composition of oligomer SOA in each particle layer depends on: (1) the monomer SOA composition, (2) the hydrogen ion concentration, (3) the dimer formation rates, (4) the oligomer degradation reaction rates, (5) possible evaporation and condensation of monomers and dimers (vapour pressures), (6) the mixing between different particle layers (diffusion coefficients of monomers and dimers), (7) the ozone uptake at the particle surface, (8) the ozone diffusion rate within

ACPD
14, 769–869, 2014

the particle bulk phase, (9) the reaction rates of ozone with unsaturated organic compounds in the particle phase, and (10) the time of aging.

2.4 Kinetic multi-layer model

To be able to model the diffusion limited mass transfer of ozone from the gas-particle interface to the particle core, and the reaction between ozone and the organic compounds in the particle phase, Shiraiwa et al. (2010) developed the kinetic multilayer model KM-SUB which is based on the PRA concept of gas-particle interactions (Pöschl et al., 2007 and Ammann and Pöschl, 2007). This model divides the particles into a sorption layer, a quasi-static surface layer, near-surface bulk, and multiple bulk layers and considers the gas-surface transport, reversible adsorption, surface layer reactions, surface-bulk transport, bulk diffusion and bulk reactions. Recently, Shiraiwa et al. extended the kinetic multilayer model to also include condensation, evaporation and heat transfer (KM-GAP) (Shiraiwa et al., 2012).

In ADCHAM we do not separate the quasi-static surface layer and near-bulk surface layer into two separate layers, but instead use a one monolayer thick surface layer. The uptake of all organic and inorganic compounds except O_3 into the surface layer from the gas phase is modelled as a condensation/evaporation process where we take into account the possibility of non-unity sticking probability (surface mass accommodation) (Sect. 2.2.1). Analogous to KM-SUB and KM-GAP, ADCHAM explicitly treats the bulk diffusion of all compounds between the surface and the different bulk layers using first-order mass transport rate equations.

The kinetic multilayer model in ADCHAM consists of two separate modules. The first module (Sect. 2.4.1) treats the diffusion of all organic and inorganic compounds (except O_3 and potentially other oxidation agents) between the different bulk layers. The second module (Sect. 2.4.2) considers the exchange of O_3 between the gas phase, particle surface and particle bulk and the reactions with organic compounds in the particle phase.

ACPD
14, 769–869, 2014

2.4.1 Diffusion of organic and inorganic compounds

The transport velocity of compound X_i between the bulk layers or the surface and first-bulk layer is given by Eq. (15).D_{X_i} is the diffusion coefficient of compound X_i, and δ_k and δ_{k+1} represent the width of the two adjacent layers (k and $k+1$) which X_i is transported between. Shiraiwa et al. (2010, 2012) use identical layer width for all bulk-layers. Hence, in their expression for the bulk to bulk transport velocity the average travel distance of molecular diffusion between two layers is simply given by the layer width and not the more general $(\delta_{k+1}+\delta_k)/2$.

$$k_{k+1,k,X_i} = k_{k,k+1,X_i} = \frac{4D_{X_i}}{\pi(\delta_{k+1}+\delta_k)/2} \tag{15}$$

The transport of compound X_i between the particle layers (including the exchange between the surface and first-bulk layer) is modelled with Eq. (16). A_k and V_k represent the area of exchange between layer $k-1$ and k and the volume of layer k, respectively. $[X_i]_k$ is the volume concentration (volume fraction) of compound X_i in layer k.

$$\frac{\mathrm{d}[X_i]_k}{\mathrm{d}t} = (k_{k-1,k}[X_i]_{k-1} - k_{k,k-1}[X_i]_k)\frac{A_k}{V_k} + (-k_{k,k+1}[X_i]_k + k_{k+1,k}[X_i]_{k+1})\frac{A_{k+1}}{V_k} \tag{16}$$

In order to keep the volume of each layer intact, the total volume flux from one layer should be identical to the volume flux into that layer. In order to accomplish this we use a volume flux matching approach where the total net volume transport between each A_k is zero. With this method the flux of each compound from the direction with the larger total volume flux is simply corrected down with a factor (x_k) equal to the ratio between the smaller and larger of the two total volume fluxes (Eq. 17). Hence, if one bulk layer consists of completely solid non-diffusing material (e.g. crystalline salt) no material can be moved in or from this layer and the transport across this layer is

ACPD
14, 769–869, 2014

completely shut down.

$$x_k = \frac{\min\left(\sum_{i=1}^{N}(k_k[X_i]_k), \sum_{i=1}^{N}\left(k_{k-1}[X_i]_{k-1}\right)\right)}{\max\left(\sum_{i=1}^{N} k_k[X_i]_k\right), \sum_{i=1}^{N}\left(\left(k_{k-1}[X_i]_{k-1}\right)\right)}, \; N = \text{total number of compounds} \quad (17)$$

The equations describing the concentration change of all compounds in all layers (Eq. 16) comprise a system of $N \times N_L$ coupled ordinary differential equations (N_L = number of particle layers) which we solve with the ode15s solver in MATLAB.

Figure 3 shows a schematic picture of the kinetic multilayer module in ADCHAM. In contrast to the kinetic multilayer model by Shiraiwa et al. (2010, 2012) the number of particle layers increases when the particles grow. Hence, particles of different sizes are composed of different number of layers.

Once the depth of the surface layer becomes larger than 1.1 nm, material is moved from this layer to the first bulk-layer, leaving a 1 nm thick surface layer. If the first bulk-layer becomes larger than a certain value (by default 3 nm thick) it is split into a first and second bulk layer with identical compositions, 1 and 2 nm thick, respectively.

By default the material which moves from the surface layer to the first bulk-layer has the same composition as the surface layer. However, it is also possible to treat certain compounds as a separate phase which accumulate in the surface layer (adsorb) and do not move into the particle bulk when the particles grow. These compounds will limit the uptake of other compounds. In ADCHAM this is represented by scaling the surface mass accommodation coefficient of the condensable compound X with the relative surface coverage of the adsorbed species (θ_s) Eq. (18) (Pöschl et al., 2007). In Sect. 3.3 we illustrate that the adsorption of material in the surface layer can be important to consider when modelling partitioning of SOA between the gas and particle phase.

$$\alpha_{s,X} = \alpha_{s,0,X}(1 - \theta_s) \quad (18)$$

ACPD
14, 769–869, 2014

Upon evaporation material is lost from the surface layer and if the layer thickness becomes less than 0.99 nm, material is moved from the first bulk layer to the surface layer, to keep the surface layer width intact. If the first bulk layer width becomes less than a certain value (by default 0.8 nm), this layer is merged together with the second bulk layer and together they form a new first bulk layer. The rest of the particle bulk is divided into layers of almost constant width (by default 2 nm thick). The width of these layers may vary somewhat due to chemical reactions (e.g. between O_3 and unsaturated hydrocarbons and mass transfer limited water uptake).

In each particle layer the model considers different oligomerization reactions and the equilibrium reactions between salts and their dissolved ions in the organic + water phase (Sects. 2.3.3 and 2.3.4). The formed oligomers and salts make up a particle volume fraction (f_p) with much lower diffusivity than the rest of the compounds. Hence, oligomerization and solid salt formation increases the viscosity which also limits the diffusion of the liquid compounds according to the obstruction theory (Stroeve, 1975). The treatment of the oligomers as solid non-diffusing compounds which limits diffusion of the liquid compounds were adopted from Pfrang et al. (2011) which used KM-SUB to model degradation of an organic 12-component mixture with ozone.

According to the obstruction theory the diffusivity of compound X_i (D_{X_i}) is a function of the fraction of solid or semi-solid material and the diffusivity (D_{0,X_i}) without any solid or semi-solid material (Eq. 19). The diffusivity of organic compounds can vary from $\sim 10^{-5}\,\mathrm{cm^2\,s^{-1}}$ in a liquid to $\sim 10^{-20}\,\mathrm{cm^2\,s^{-1}}$ in a solid organic matrix (Shiraiwa et al., 2011).

$$D_{X_i} = D_{0,X_i}(2 - 2f_p)/(2 + f_p) \tag{19}$$

2.4.2 O_3 diffusion and reactions with SOA

The diffusion of O_3 and potentially other oxidation agents between the particle bulk layers is equivalent to the treatment of other compounds (Eqs. 15 and 16), except that we do not consider that the dissolved O_3 in the particle phase take up a bulk volume of its own.

ACPD
14, 769–869, 2014

The uptake of ozone from the gas phase to the particle surface is treated as a reversible adsorption process (Fig. 3). This approach was adopted from Shiraiwa et al. (2010). The surface accommodation coefficient of O_3 is given by Eq. (20). θ_{s,O_3} is the relative coverage of adsorbed O_3 on the particle surface. The adsorption of O_3 from the near surface gas phase (gs) to the sorption layer (so) and the desorption from the sorption layer to the near surface-gas phase is given by Eqs. (21) and (22), respectively. ω_{O_3} is the mean thermal velocity of O_3 and τ_{d,O_3} is the desorption lifetime of O_3.

The transport velocity of O_3 from the surface layer to the sorption layer is given by Eq. (23). δ_s is the width of the monolayer thick surface layer and d_{O_3} is the width of the sorption layer. Hence, $(\delta_s + d_{O_3})/2$ in Eq. (23) represents the average travel distance between the sorption and surface layer. The transport velocity of O_3 from the sorption layer to the surface layer can then be calculated from Eq. (24). K_{H,O_3} is the Henry's law coefficient of O_3.

$$\alpha_{s,O_3} = \alpha_{s,0,O_3}(1-\theta_{s,O_3}), \theta_{s,O_3} = \frac{[O_3]_{so} d_{O_3}^2 \pi}{4} \quad (20)$$

$$J_{ads,O_3} = [O_3]_{gs} \omega_{O_3} \alpha_{s,O_3}/4 \quad (21)$$

$$J_{des,O_3} = \tau_{d,O_3}^{-1} [O_3]_{so} \quad (22)$$

$$k_{su,so,O_3} \approx \frac{4D_{O_3}}{\pi\left(\delta_s + d_{O_3}\right)/2} \quad (23)$$

$$k_{so,su,O_3} = \frac{4k_{su,so,O_3} K_{H,O_3} \tau_{d,O_3}^{-1}}{\alpha_{s,O_3}\omega_{O_3}} TR \quad (24)$$

Equations (25)–(27) form a differential equation system which describes the rate of change of the ozone concentration in the particle sorption layer, particle surface layer, and particle bulk layers. The chemical oxidation reactions between ozone and the or-

ACPD
14, 769–869, 2014

ganic compounds (X_i) are represented by the last term in Eqs. (26) and (27), where the summation is over all compounds which react and consume O_3 in the particle phase. The module also calculates the temporal evolution of the organic compounds (X_i) which are consumed by ozone and the organic compounds which are formed from the oxidation reactions (Y_i) (Eqs. 28 and 29). The diffusion of these compounds is treated by the kinetic multilayer module described in Sect. 2.4.1.

$$\frac{\mathrm{d}[\mathrm{O_3}]_{\mathrm{so}}}{\mathrm{d}t} = J_{\mathrm{ads,O_3}} - J_{\mathrm{des,O_3}} - k_{\mathrm{so,su,O_3}}[\mathrm{O_3}]_{\mathrm{so}} + k_{\mathrm{su,so,O_3}}[\mathrm{O_3}]_{\mathrm{su}} \tag{25}$$

$$\frac{\mathrm{d}[\mathrm{O_3}]_{\mathrm{su}}}{\mathrm{d}t} = (k_{\mathrm{so,\,su}}[\mathrm{O_3}]_{\mathrm{so}} - k_{\mathrm{su,\,so}}[\mathrm{O_3}]_{\mathrm{su}})\frac{A_{\mathrm{su}}}{V_{\mathrm{su}}} + (-k_{\mathrm{su,b1}}[\mathrm{O_3}]_{\mathrm{su}} + k_{\mathrm{b1,su}}[\mathrm{O_3}]_{\mathrm{b1}})\frac{A_{\mathrm{b1}}}{V_{\mathrm{su}}} - \sum_{i=1}^{N} k_{\mathrm{Ox},i}[X_i]_{\mathrm{su}}[\mathrm{O_3}]_{\mathrm{su}} \tag{26}$$

$$\frac{\mathrm{d}[\mathrm{O_3}]_{\mathrm{bk}}}{\mathrm{d}t} = (k_{\mathrm{bk-1,bk}}[\mathrm{O_3}]_{\mathrm{bk-1}} - k_{\mathrm{bk,bk-1}}[\mathrm{O_3}]_{\mathrm{bk}})\frac{A_{\mathrm{bk}}}{V_{\mathrm{bk}}} + (-k_{\mathrm{bk,bk+1}}[\mathrm{O_3}]_{\mathrm{bk}} + k_{\mathrm{bk+1,bk}}[\mathrm{O_3}]_{\mathrm{bk+1}})\frac{A_{\mathrm{bk+1}}}{V_{\mathrm{bk}}} - \sum_{i=1}^{N} k_{\mathrm{Ox},i}[X_i]_{\mathrm{bk}}[\mathrm{O_3}]_{\mathrm{bk}} \tag{27}$$

$$\frac{\mathrm{d}[X_i]_{\mathrm{bk}}}{\mathrm{d}t} = -k_{\mathrm{Ox},i}[X_i]_{\mathrm{bk}}[\mathrm{O_3}]_{\mathrm{bk}} \tag{28}$$

$$\frac{\mathrm{d}[Y_i]_{\mathrm{bk}}}{\mathrm{d}t} = k_{\mathrm{Ox},i}[X_i]_{\mathrm{bk}}[\mathrm{O_3}]_{\mathrm{bk}} \tag{29}$$

Table 1 gives the values of different parameters used in the multilayer module for ozone uptake, diffusion and reactions within the particle phase. Most of the values were adopted from Table 1 in Pfrang et al. (2011).

The coupled ordinary differential equation system describing the temporal evolution of O_3 and the concentration of compounds which are consumed or formed from the O_3 oxidation is solved with the ode15s solver in MATLAB.

ACPD
14, 769–869, 2014

3 Model applications

In order to test and illustrate the capability of ADCHAM we apply the model to four types of published experimental results. In Sect. 3.1 we model the evaporation experiments of liquid dioctyl phthalate (DOP) particles presented in Vaden et al. (2011), which have been modelled by Shiraiwa et al. (2012) with the KM-GAP model. In Sect. 3.2 we model the SOA formation, ammonia uptake, and organic salt (NH_4RCOO) formation in the α-pinene-NH_3-O_3 experiments by Na et al. (2007). In Sect. 3.3 we model the evaporation experiments of α-pinene SOA particles by Vaden et al. (2011). Finally, we apply ADCHAM to a *m*-xylene oxidation experiment from Nordin et al., 2013 (Sect. 3.4). These examples serve to illustrate the wide applicability of ADCHAM.

For the simulations in Sects. 3.2 and 3.3 we model the condensational growth of particles formed by homogeneous nucleation using the condensation module described in Sect. 2.2.1 using the full moving method (see Sect. 2.2.4). We start with one particle size and add new particle size bins during the early stage of particle formation. The new particles are assumed to be composed of non-volatile SOA material and are introduced into the model at an initial diameter of 5 nm. Hence, in this work we do not treat the initial activation and growth of the formed molecular clusters. The new particle formation rate ($J_{5\,nm}$) is assumed to be constant during the experiments. A new size bin is added for the time step when the smallest particle size grows larger than 10 nm in diameter. For the experiments which we simulate in this work the SOA mass (condensation sink) increases rapidly during the early stage of SOA formation. This effectively prevents the newly formed particles from growing and thus generally keeps the number of model particle size bins down to less than 20 (see Fig. S1 in the Supplement).

3.1 Simulations of DOP particle evaporation

Before modelling complex multicomponent SOA particle formation, growth and evaporation we test ADCHAM on the evaporation experiments of single component, liquid DOP particles (Vaden et al., 2011). The particles, in that study, were evaporated in

ACPD
14, 769–869, 2014

a 7 L chamber with 1 L of activated charcoal at the bottom of the chamber. The particle number concentration was kept low ($\sim 150\,\mathrm{cm}^{-3}$) in order to keep the gas phase concentration close to zero. Before the aerosol was introduced into the chamber, it was passed through two charcoal denuders in order to remove most of the gas phase DOP (Vaden et al., 2011).

Here we adopt the approach from Shiraiwa et al. (2012) who modelled the gas phase loss to the charcoal denuder using Fick's first law, on a laminar layer (Δx) adjacent to the charcoal denuder, on the bottom of the chamber. Since the layer thickness is poorly known, we modelled the DOP(g) loss rate using different Δx. Coagulation and particle wall losses were not considered. In this small chamber, the wall losses can be substantial, however particles deposited on the chamber walls not coated with charcoal will likely continue to evaporate and contribute to the gas phase DOP. Neglecting the particle wall losses is equivalent to assuming that the particles deposited on the walls behave as if they were still in the gas phase (Sect. 2.2.3).

Vaden et al. (2011) and Shiraiwa et al. (2012) used a binary diffusion coefficient for DOP in air of $4.4 \times 10^{-2}\,\mathrm{cm}^2\,\mathrm{s}^{-1}$ from Ray et al. (1988). This value was measured at a pressure of 98 Torr (0.13 atm), which is lower than the pressure used in experiments. We have therefore estimated the diffusion coefficient (D_{DOP}) with Eq. (30) (Jacobson, 2005) or with Eq. (31) (Chapman and Cowling, 1970, in accordance with Zhang et al., 1993). Eq. (30) gives a D_{DOP} of $1.5 \times 10^{-2}\,\mathrm{cm}^2\,\mathrm{s}^{-1}$, while with the Chapman–Enskog theory, utilizing a value of 1.34 for the collision integral ($\Omega^{(1,1)}_{\mathrm{DOP,air}}$) (Hirschfelder et al., 1954), yields $2.9 \times 10^{-2}\,\mathrm{cm}^2\,\mathrm{s}^{-1}$, for D_{DOP} at 1 atm and 296 K.

$$D_i = \frac{5}{16 N_{\mathrm{a}} d_i^2 \rho_{\mathrm{air}}} \sqrt{\frac{R T M_{\mathrm{air}}}{2\pi} \left(\frac{M_i + M_{\mathrm{air}}}{M_i} \right)} \tag{30}$$

$$D_i = \frac{3}{8\pi \Omega^{(1,1)}_{i,\mathrm{air}} p d^2_{\mathrm{i,\,air}}} \sqrt{\frac{\pi k_{\mathrm{b}}^3 T^3 (m_i + m_{\mathrm{air}})}{2 m_i m_{\mathrm{air}}}}, d_{\mathrm{i,\,air}} = \frac{d_i + d_{\mathrm{air}}}{2} \tag{31}$$

ACPD
14, 769–869, 2014

N_a is Avogadro's number, ρ_{air} is the density of air, M_{air} is the molar mass of air, M_i is the molar mass of compound i (M_{DOP} = 390.56 g mol^{-1}), d_i is the collision diameter of compound i (d_{DOP} = 1.012 nm, Ray et al., 1979), $d_{i,\,air}$ is the collision diameter for binary collisions between compound i and air molecules (d_{air} = 0.362 nm), m_{air} is the molecular mass of air, m_i is the molecular mass of compound i, k_b is the Boltzmann constant and p is the total pressure.

When we use Eq. (30), a laminar layer of 0.1 cm adjacent to the charcoal denuder wall and unity $\alpha_{s,DOP}$, the model is in good agreement with the observed evaporation rates for all particle sizes. Similar results are also achieved when using Eq. (31), unity $\alpha_{s,DOP}$ and a laminar layer of 0.6 cm adjacent to the charcoal denuder (Fig. 4).

In Sect. 3.3 we compare the modelled and measured α-pinene SOA evaporation rates using the same evaporation chamber. Based on the DOP evaporation experiments the simulations of the α-pinene SOA particle experiments were performed with a Δx of 0.1 cm, binary diffusion coefficients calculated with Eq. (30), and unity surface mass accommodation coefficients, for particle surfaces free from adsorbing material ($\alpha_{0,s}$ = 1).

3.2 Modelling of organic salt formation between carboxylic acids and ammonia

Here we model the SOA formation in the α-pinene-NH_3-O_3 experiments by Na et al. (2007), in a dark indoor 18 m^3 Teflon chamber. In the experiments CO (~ 200 ppm) was used as OH-scavenger. The chamber was operated at a temperature of 21 ± 1 °C, and dry conditions. For the simulations we use a RH of 5 % and a temperature of 21 °C. Once the α-pinene and NH_3 initial target concentrations were reached, the experiments started by injecting O_3 for approximately 20 min, to produce an O_3 concentration of 200 ± 5 ppb. In the model, emissions corresponding to 250 ppb unreacted O_3 were added during the first 20 min, in order to simulate the experimental target O_3 concentrations.

ACPD
14, 769–869, 2014

In the experiments Na et al. (2007) observed a substantially higher SOA formation when NH_3(g) was present. The authors also performed experiments on *cis*-pinonic acid (a common α-pinene oxidation product), and found a dramatic increase in particle number and volume concentration when NH_3 was added to the system. From these experiments they concluded that most of the observed SOA mass enhancement in the presence of NH_3 could be explained by acid-base reactions which drive the carboxylic acids into the particle phase. Similar organic salt formation in the presence of NH_3 was observed both at dry and humid conditions (RH = 50 %).

Several experiments were performed at initial NH_3(g) concentration between 0–400 ppb and an α-pinene concentration of $\sim$ 220 ppb (see Table 1 in Na et al., 2007). The formed aerosol particle mass increases when more NH_3 is added. However, when the ammonia concentration exceeded 200 ppb no substantial additional mass formation was observed. The reason for this could be that in principle all gas phase carboxylic acids already have formed particle mass at 200 ppb NH_3 (Na et al., 2007).

Recently, Kuwata and Martin (2012) conducted experiments with an Aerosol Mass Spectrometry (AMS) on SOA formed from ozonolysis of α-pinene at low and high relative humidity (RH < 5 % and RH > 94 %). In these experiments, the α-pinene SOA particles were formed at dry conditions before they were exposed to varying degree of humidification and ammonia (see Fig. 1 in Kuwata and Martin, 2012). An $\sim$ 10 times greater uptake of ammonia was observed at high RH compared to low RH, which was attributed to a more rapid diffusion uptake of ammonia in the less viscous humidified aerosol particles. However, since the gas phase was not removed from the aerosol between the generation and the exposure to ammonia, part of the ammonia uptake could be attributed to reactive uptake of NH_3 and organic acids from the gas phase (Kuwata and Martin, 2012).

In this work we model the organic salt formation between ammonium and carboxylic acids as a process occurring in the particle surface layer and particle bulk and not in the gas phase. The partitioning of carboxylic acids and ammonia between the gas phase and particle surface layer are modelled as separate pH dependent dissolution

ACPD
14, 769–869, 2014

processes using the condensation/evaporation module (Sect. 2.2.1). The amount of organic acids, ammonia/ammonium and organic salts which exists in the particles depend on the pure-liquid saturation vapour pressures or Henry's law constant (K_H), acid dissociation constants (K_a), activity coefficients, surface tension (Barsanti et al., 2009) and the solubility product of the formed salts (K_s) (R9–R13). The aerosol particle formation will be favoured by low pure-liquid saturation vapour pressures of the carboxylic acids, large solubility (Henry's law coefficient) of NH_3, large difference between the carboxylic acids and NH_4^+ K_a values (Greaves and Drummond, 2008) and low solubility of the formed salts (K_s).

$$\mathrm{RCOOH(g)} \leftrightarrow \mathrm{RCOOH(l)} \tag{R9}$$

$$\mathrm{RCOOH(l)} \leftrightarrow \mathrm{RCOO^-} + \mathrm{H^+}, \quad K_a = \frac{[\mathrm{RCOO^-}][\mathrm{H^+}]\gamma_{\mathrm{H^+}}\gamma_{\mathrm{RCOO^-}}}{[\mathrm{RCOOH}]\gamma_{\mathrm{RCOOH}}} \tag{R10}$$

$$\mathrm{NH_3(g)} \leftrightarrow \mathrm{NH_3(l)}, \quad K_H = \frac{[\mathrm{NH_3(l)}]\gamma_{\mathrm{NH_3}}}{p_{\mathrm{NH_3}}} \tag{R11}$$

$$\mathrm{NH_3(l)} + \mathrm{H^+} \leftrightarrow \mathrm{NH_4^+}, \quad \frac{1}{K_{a,\mathrm{NH_4^+}}} = K_{\mathrm{NH_3}} = \frac{[\mathrm{NH_4^+}]\gamma_{\mathrm{NH_4^+}}}{[\mathrm{NH_3(l)}][\mathrm{H^+}]\gamma_{\mathrm{NH_3}}\gamma_{\mathrm{H^+}}} \tag{R12}$$

$$\mathrm{NH_4^+} + \mathrm{RCOO^-} \leftrightarrow \mathrm{NH_4RCOO(s)}, \quad K_s = [\mathrm{NH_4^+}][\mathrm{RCOO^-}]\gamma_{\mathrm{NH_4^+}}\gamma_{\mathrm{RCOO^-}} \tag{R13}$$

Table 2 lists different model parameter values used for the base case simulations in this section. The K_a values are unknown for most carboxylic acids, even in aqueous solutions. However, for two major ozonolysis products (*cis*-pinic acid) and (*cis*-pinonic acid) (Hallquist et al., 2009), aqueous pK_a values were found in the literature (see e.g. Hyder et al., 2012 and Barsanti et al., 2009). These acids have nearly the same pK_a values (~ 4.6). Hence, in this work we will assume that all carboxylic acids from α-pinene ozonolysis which partition into the particle organic rich phase have pK_a values equal to 4.6.

ACPD
14, 769–869, 2014

Unfortunately we could not find any values of solubility products between carboxylic acids and ammonium in the literature. Hence, we decided to define an effective solubility product (K_s^*) as the product between the ammonium concentration and the total deprotonated carboxylic acid concentration ($[RCOO^-]_{tot}$) (Eq. 32). K_s^* was used as an unknown parameter which we varied in order to find the best agreement between the model and measurements.

$$K_s^* = \left[NH_4^+\right] [RCOO^-]_{tot} \quad (32)$$

If not otherwise specified, the pure-liquid saturation vapour pressures of the organic compounds were estimated with the SIMPOL method, K_s^* was set to $0.1\,mol^2\,m^{-6}$, and the NH_4RCOO salts were mixed with the other organic compounds (no separate phase). Because the interactions between the NH_4RCOO and other organic compounds and inorganic ions are unknown (see Sect. 2.3.1), NH_4RCOO was not considered to influence the activity coefficients of the other compounds. However, as a second extreme condition we performed simulations where we treated NH_4RCOO and the other organic compounds + inorganics as two completely separate phases (liquid-liquid phase separated or NH_4RCOO as crystalline salts (see Sect. 1)). The diffusion coefficients for monomer SOA and ammonia/ammonium were estimated with the Stoke–Einstein relationship using a viscosity of $\sim 10^8$ Pa s (see Sect. 1). Because the viscosity of the SOA is uncertain and depend on the experimental conditions and time of aging, we also performed simulations with less viscous particles ($D_{0,monomer,SOA} = 10^{-15}\,cm^2\,s^{-1}$, $D_{0,ammonium} = 10^{-13}\,cm^2\,s^{-1}$).

In Table 3 we have listed the measured and model initial concentrations, concentration change of ozone ($\Delta[O_3] = [O_3]_{max} - [O_3]_{t=6h}$) and α-pinene $\Delta[\alpha - pin.]$, and SOA yields. Figure 5 shows the modelled temporal evolution of the α-pinene, O_3, NH_3 and OH concentrations in the gas phase. The O_3 concentration rises during the first 20 min while O_3 is continuously applied to the chamber. The OH concentration reaches a maximum of $\sim 10^6$ molecules cm^{-3} at the same time as the maximum O_3 concentration. Hence, according to the model the experiments with CO as OH scavenger is not a pure

ACPD
14, 769–869, 2014

O_3 oxidation experiments, but a fraction of the α-pinene and the oxidation products are also oxidized with OH. Figure S2 in the Supplement shows the cumulative fraction of reacted α-pinene which was oxidized by O_3 during the evolution of the experiment. In the beginning of the experiment only 86 % of the consumed α-pinene was oxidized by O_3, while at the end of the experiment 92 % of the consumed α-pinene was oxidized by O_3.

In Fig. 6 we compare the modelled and measured SOA yields from experiments conducted with approximately 220 ppb α-pinene, 200 ppb O_3 and varying initial NH_3 concentrations. The model results in Fig. 6a is from the base case simulation set-up (Table 2). Figure 6b shows model results from simulations performed with pure-liquid saturation vapour pressures from Nannoolal et al. (2008). The results in Fig. 6c are from model runs with unity activity coefficients (Raoult's law for ideal solution) and Fig. 6d shows results from simulations with less viscous particles ($D_{0,\mathrm{monomer,SOA}} = 10^{-15}\,\mathrm{cm^2\,s^{-1}}$, $D_{0,\mathrm{ammonium}} = 10^{-13}\,\mathrm{cm^2\,s^{-1}}$ and $D_{0,\mathrm{NH_4RCOO}} = 0\,\mathrm{cm^2\,s^{-1}}$). For a particle with a diameter of 250 nm these values of the diffusion coefficients give an e-folding time of equilibration of 2.6 min for NH_3 and 4.4 h for SOA monomers.

For the base case simulations the agreement between the modelled and measured SOA mass and SOA yields are surprisingly good, both with and without addition of NH_3. One reason for this is that the organic salt effective solubility product (Eq. 32) was used as a model fitting parameter. However, in order for the model to agree with the measurements the amount of semi-volatile carboxylic acids formed from the α-pinene oxidation still needs to be reasonably well predicted, which seems to be the case. Figure S3 in the Supplement shows the modelled temporal evolution of the total carboxylic acid concentration (gas + particle phase).

We find the largest difference between the model runs, and between the model and measurements, when we use the pure-liquid saturation vapour pressure method from Nannoolal et al. (2008) instead of SIMPOL (Pankow and Asher, 2008) (Fig. 6b). The model then underestimates the SOA mass with $\sim 200\,\mu\mathrm{g\,m^{-3}}$ (~ 30 %), irrespectively of the amount of NH_3 added.

ACPD
14, 769–869, 2014

Figure S4 in the Supplement shows a comparison of the volatility basis set (VBS) parameterization from Pathak et al. (2007) and VBS parameterizations which we have derived from the MCMv3.2 condensable α-pinene oxidation products using either the method from Nannoolal et al. (2008) or SIMPOL. The MCMv3.2 α-pinene oxidation product VBS parameterizations are given both for CO and cyclohexane as OH-scavenger. The VBS parameterizations show large differences both between the vapour pressure methods and the type of OH scavenger used. By comparing the VBS parameterizations we can conclude that SIMPOL gives the largest SOA mass at high α-pinene concentrations (this work). However, at low (atmospherically more realistic) α-pinene concentrations the Nannoolal method will give the least volatile SOA and highest SOA mass.

Barley and McFiggans, 2010 have shown that the uncertainties of the calculated pure-liquid saturation vapour pressures are large, especially for low-volatility compounds with several functional groups. However, because of other large uncertainties, e.g. oligomerization processes and gas phase chemistry mechanisms (see Sect. 1), we cannot predict which of the two liquid saturation vapour pressure methods that give the most realistic vapour pressures. In Sect. 3.3 we illustrate how the estimated volatility of the α-pinene gas phase oxidation products can have substantial effects on the particle evaporation loss rates.

In contrast to the vapour pressures, the modelled activity coefficients have only small influence on the simulated SOA mass formation (compare Fig. 6a and c). This is consistent with the conclusions from McFiggans et al. (2010), and Zuend and Seinfeld (2012) for conditions without dissolved inorganic ions and low relative humidity. The mass difference between the model runs ($[OA_{ideal}] - [OA_{activity}]$) is small without added NH_3, but increases when the free particle ammonium concentration increases. The reason for this is that the dissolved ammonium ions generally increase the organic molecule activity coefficients (salting-out effect). At atmospheric more realistic relative humidities ($> 30\,\%$), salt effects which either cause liquid-liquid phase separation or

ACPD
14, 769–869, 2014

drive the organic compounds out from the particles, may have large effects on the SOA formation (see e.g. Zuend and Seinfeld, 2012).

If we assume that the SOA is less viscous (Fig. 6d), the mass yields are slightly larger (60.7 % compared to 57.5 % without NH_3 addition, and 69.1 % compared to 67.0 % when 200 ppb NH_3 is added at the start of the experiments).

Figure S5 in the Supplement shows the total SOA mass and NH_4RCOO mass for varying initial NH_3 concentration, $K_s^* = 0.01$ or $0.1\,mol^2\,m^{-6}$and semi-solid SOA particles. As expected the NH_4RCOO mass concentration, and the total particle mass increases when K_s^* is lowered. However, for 200 ppb NH_3 the difference becomes negligible since almost all carboxylic acids are anyhow found in the particle phase. The results also reveal a moderate salting-out effect of the ammonium on the SOA (see the decrease in the total particle mass with increasing NH_3 when $K_s^* = 0.01\,mol^2\,m^{-6}$).

In order to test which processes that can explain the observed NH_3 uptake in α-pinene SOA particles, exposed to NH_3(g) after particle formation (Kuwata and Martin, 2012 and Na et al., 2007), we also performed simulations where the SOA particles were allowed to age for 6 h before they were exposed to 200 ppb NH_3(g). To test the effect of mass transfer limited uptake of NH_3, the particles were either treated as glassy solids (no mixing) or semi-solids ($D_{0,monomer,SOA} = 10^{-15}\,cm^2\,s^{-1}$, $D_{0,ammonium} = 10^{-13}\,cm^2\,s^{-1}$).

In Fig. 7a the temporal evolution of the modelled SOA mass from these simulations are shown. As a comparison, the results from simulations with 200 ppb NH_3(g) added at the start of the experiments are also plotted. After the addition of NH_3, the SOA mass increases rapidly both with and without mass transfer limited diffusion uptake in the particles (semi-sold or solid particles). This indicates that the rapid uptake of NH_3(g), by the particles, mainly is caused by reactive uptake of carboxylic acids(g) and NH_3(g) and not by the diffusion of NH_3/NH_4^+ into the particle bulk. However, the temporal evolution of the formed NH_4RCOO salts and dissociated and non-dissociated carboxylic acids (Fig. 7b), reveal that the mass of NH_4RCOO salts formed in the semi-solid particles are twice as high, and the carboxylic acid mass concentration is substantially lower,

ACPD
14, 769–869, 2014

than if treating the SOA as solid. This difference is attributed to the mass transfer limited uptake and reaction of NH_3/NH_4^+ with the carboxylic acids found in the semi-solid particle bulk interior.

However, although the NH_4RCOO concentration becomes higher if the particles are semi-solid (less viscous), the total aerosol mass 3 h after the addition of ammonium is lower than if the particles are solid (compare simulation Nr. 4 and 5 in Fig. 7a). The reason for this is the salting-out effect of NH_4^+ which causes the nonpolar organic compounds to evaporate. For these simulations, the salting-out effect is mainly important if both the NH_3/NH_4^+ and the organic compounds can be transported between the bulk and particle surface layer. In the laboratory experiments (see Fig. 2a in Na et al., 2007) no SOA mass loss could be seen after the NH_4RCOO formation. This experiment continued less than 1 h after the addition of NH_3, but it at least indicates that the mixing of organic compounds within the particle phase is mass transfer limited, and/or that the NH_4RCOO salts form a separate phase, which limits the salting-out of other SOA compounds from the particles to the gas phase.

Figure 7a also shows the simulated SOA mass formation when we treat the NH_4RCOO salts as a separate phase (e.g. crystalline salt) which other condensable organic compounds cannot dissolve into. When NH_3(g) is added during the start of the experiments the difference between the model runs with and without a separate NH_4RCOO phase is relatively small. However, if the NH_3(g) is added after the solid SOA particles have formed, only a moderate SOA mass increase is accomplished ($\sim 9\,\%$). This is in sharp contrast to the results from the simulations with solid particles and only one organic phase (mass increase of $\sim 39\,\%$). The reason for this is that the ammonium salts are enriched in the particle surface layer, and if no other compounds can dissolve into this phase their uptake is limited. On the other hand if NH_4RCOO is part of a single amorphous organic phase, it will lower the mole fractions of the other compounds and hence increase (at least for ideal conditions) the uptake of them (see Eq. 2). This is the reason why the total SOA mass increase is larger ($\sim 270\,\mu g\,m^{-3}$, $\sim 39\,\%$), than the increase explained purely by the carboxylic acids and NH_4RCOO

ACPD
14, 769–869, 2014

($46 + 84 = 130\,\mu g\,m^{-3}$, ~ 19 %) (see simulation Nr. 4 in Fig. 7a and b). Na et al. (2007) observed a mass increase of 15 % when 1000 ppb NH_3 was added after the α-pinene SOA particle mass formation had ceased. This increase is larger than the modelled increase when considering complete phase separation between NH_4RCOO and the other condensable organic compounds, but substantially smaller than for the simulations with only one organic phase. This indicates that in reality, there will neither be perfect (ideal) mixing between NH_4RCOO and the other condensable organic compounds, nor a complete phase separation.

Figure 8 shows (a) the modelled pH, (b) the total ammonium mass fraction (free and bonded in ammonium salts), (c) the NH_4RCOO mass fraction and (d) the carboxylic acid mass fraction ($[RCOO^-] + [RCOOH]$) for a semi-solid SOA particle, at different distances from the particle core. The figure includes results from simulations with initial NH_3(g) concentrations of 50, 100 and 200 ppb, respectively, and at 1 or 6 h of aging. A large fraction of the SOA formed early during the experiments are due to condensation of carboxylic acids. This explains the large mass fractions of carboxylic acids and the lower pH in the particle cores (Fig. 8a and b). For the simulations with 200 ppb NH_3, a large fraction of the carboxylic acids and ammonium form salts (Fig. 8c), while when only 50 ppb NH_3 is added, ammonium salts are only present during the early stage of particle formation, when the carboxylic acid mass fraction is large. Because of the assumed relatively rapid mixing of ammonium (e-folding time of a few minutes), the free ammonium concentration (not bound in organic salts) are almost constant in all particle layers. Hence, the differences in the NH_4RCOO concentrations between different layers are largely caused by differences in the carboxylic acid concentrations, which even after 6 h of aging are not uniformly mixed.

Form the simulations in this section we can conclude that ADCHAM (with the pure-liquid saturation vapour pressures from SIMPOL and activity coefficients from AIOMFAC), are able to reproduce the observed SOA formation at different concentrations of NH_3(g). With NH_3 present during the formation, reactive uptake of carboxylic acids contributes substantially to the modelled early growth of the particles formed by homo-

ACPD
14, 769–869, 2014

geneous nucleation. However, because of the relatively high concentrations, we cannot conclude whether this mechanism is important in the atmosphere.

3.3 Evaporation of α-pinene SOA

Here we use ADCHAM to explore which processes are responsible for the slow and nearly size independent evaporation loss rates of α-pinene SOA particles observed by Vaden et al. (2011). α-pinene SOA particles were produced by homogeneous nucleation in a 0.1 m^3 Teflon chamber under dark conditions with ~ 200 ppb α-pinene, ~ 250 ppm cyclohexane as OH-scavenger and ~ 500 ppb O_3. Once SOA particles stopped growing (approximately after 1.5 h, fresh particles), monodisperse aerosol particles were selected with a differential mobility analyser (DMA), passed through two charcoal denuders (residence time ~ 2 min), and introduced at low concentration (~ 10–200 cm^{-3}) into the evaporation chamber described in Sect. 3.1 (Vaden et al., 2011). Alternatively, the particles were aged for 10–15 h (aged particles) in the Teflon chamber before being transferred into the evaporation chamber.

Vaden et al. (2011) showed that the evaporation rate of the pure α-pinene SOA particles is more than 100 times slower than expected from modelled evaporation rates of liquid-like monomer SOA and that it consists of two stages. ~ 50 % of the particle mass evaporates during the first 100 min at relatively slow rate, followed by a second stage with even slower mass loss rate, in which additional ~ 25 % of the initial mass is lost in 24 h. Another interesting finding is that the fractional volume loss by evaporation is almost size-independent. Vaden et al. (2011) concluded that the nearly size-independent evaporation loss rates indicate that these type of SOA particles are not liquid-like, which was later confirmed by Abramson et al. (2013).

Here we use ADCHAM to examine which of the processes listed below that determine the observed α-pinene SOA evaporation rates. Note that while the model includes various specific mechanisms, the conclusions should be taken in terms that are more general.

ACPD
14, 769–869, 2014

1. Vapour pressures of the condensable monomers (pure-liquid saturation vapour pressure method)

2. Slow and imperfect mixing within semi-solid amorphous SOA particles

3. Oligomerization on the surface (surface oligomer) and in the particle bulk (bulk oligomer), and their reversible decomposition to monomers

4. Accumulation of low volatility oligomers at the particle surface, creating a coating material which prevents the more volatile SOA monomers from evaporating

For all simulations presented in this section the monomer SOA mass accommodation coefficients were assumed to be proportional to the particle surface area not covered by non-volatile oligomer SOA $(1 - \theta_s)$ (Eq. 18). The simulations were conducted for 23 °C, RH of 5 %, and a pressure of 1 atm. The laminar layer width adjacent to the charcoal denuder in the evaporation chamber was assumed to be 0.1 cm (see motivation in Sect. 3.1). Pure-liquid saturation vapour pressures were estimated with the SIMPOL model, except where otherwise noted. Particles of different sizes were formed by homogeneous nucleation and were allowed to grow in the presence of each other. After 1.5 h or 12 h of aging (fresh or aged aerosol) size-selected particles with concentration $\sim 100\,\mathrm{cm}^{-3}$ were introduced into the modelled charcoal denuder chamber and allowed to evaporate by continuous removal of the gas phase compounds. No wall losses were considered (see discussion in Sects. 3.1 and 3.4).

3.3.1 Evaporation of pure monomer SOA particles

Experimental evidence suggests that there are no substantial differences in chemical composition of α-pinene SOA particles upon evaporation in thermodenuders. Hence, these particles do not seem to obey absorptive partitioning theory upon evaporation. This could possibly be explained by a diffusion-limited transport of the organic compounds within an amorphous (glassy) particle phase (Cappa and Wilson, 2011). In

ACPD
14, 769–869, 2014

Vaden et al. (2011) they note that the mass spectral peak at $m/z = 201$ rapidly disappears on evaporation and that the only other change is a gradual increase in relative intensity of peaks at higher m/z. These changes suggest an increase in the relative oligomer content, which could indicate that the smaller, higher vapour pressure molecules evaporate and oligomerization continues at a slow rate during evaporation, consistent with the observed SOA hardening (Abramson et al., 2013).

To set the stage, we start by calculating if the evaporation rates can be explained by the volatility distribution of the condensing monomers formed in the gas phase, in combination with non-perfect mixing within a semi-solid amorphous particle phase. The evaporation of the more volatile organic compounds will then be controlled by the evaporation rate of the least volatile organic compounds enriched in the particle surface layer, and not by their own species specific saturation vapour pressures. The measured mass spectra and densities of small and large SOA particles formed by ozonolysis of α-pinene are undistinguishable (Zelenyuk et al., 2008). Despite this fact, we use the model to evaluate whether it gives a relative enrichment of the least volatile monomer SOA compounds in the smaller particles during their formation and growth (see e.g. Roldin et al., 2011b), and if this can explain the observed size-independent SOA evaporation.

The pure-liquid saturation vapour pressures were calculated with the SIMPOL (Pankow and Asher, 2008), Nannoolal et al. (2008) vapour pressure methods or with the semi-empirical 7-product model (VBS) parameterization from Pathak et al. (2007), which was also used by Vaden et al. (2011). In Sect. 3.2 we showed that the choice of method used to determine vapour pressures can profoundly influence the modelled SOA mass (Figs. 6 and S4 in the Supplement). Here we evaluate its influence on the modelled evaporation rates of 150 nm and 250 nm particles. The model results presented in Fig. 9 are from simulations assuming liquid-like SOA ($D_{\mathrm{monomer}} = 10^{-10}\,\mathrm{cm^2\,s^{-1}}$) or solid-like SOA particles with negligible mixing ($D_{\mathrm{monomer}} = 0\,\mathrm{cm^2\,s^{-1}}$). In Fig. 9a the results are from simulations with the VBS from Pathak et al. (2007),

ACPD
14, 769–869, 2014

Fig. 9b shows the results when we use SIMPOL and Fig. 9c results from simulations with the Nannoolal method.

In all model runs except with the Nannoolal method and solid-like amorphous particles, the evaporation rates are more than ~ 100 times faster than the observations. According to the curve fitted to the measurements only ~ 3 % of the SOA mass is lost during the first 2 min. However, in the model runs 20–80 % are lost, depending on vapour pressure method used, the particle size, and if the SOA is treated as liquid (l) or solid (s) like.

Another difference is that the observed evaporation loss rate is almost linear for the first 30 min while in all model runs the loss rate is first very rapid and then gradually slows down. This is because in the model the SOA is composed of molecules with different volatility. Hence, the most volatile molecules are lost early and the remaining compounds that are less volatile evaporate later and slower, inconsistent with observations (Cappa and Wilson, 2011 and Vaden et al., 2011). Moreover, all calculated evaporation rates are size dependent, similarly inconsistent with the observed SOA evaporation (Vaden et al., 2011; Zelenyuk et al., 2012).

When the SOA is treated as a solid the evaporation rates are much slower with the Nannoolal method compared to the other two methods, even though most of the other SOA mass is somewhat more volatile than with the SIMPOL method (see Fig. S5 in the Supplement). This is mainly because of a low-volatile compound with MCMv3.2 species name C922OOH, which before evaporation make up ~ 3 % and ~ 2 % of the particle mass in the 150 nm and 250 nm particles, respectively (see modelled mass spectrum in Fig. S6). This compound has a vapour pressure of 7.5×10^{-8} Pa (at 298 K) when calculated with the Nannoolal method, while with SIMPOL we arrive at a vapour pressure of 2.2×10^{-6} Pa (at 298 K). Hence, if the SOA particles are considered to be solid or semi-solid, and the Nannoolal method is used, this compound accumulates in the particle surface layer upon evaporation and limits the loss of the other more volatile compounds.

ACPD
14, 769–869, 2014

From the discrepancy between the model and measurement results in Fig. 9 we can conclude that it is unlikely that the observed evaporation rates can be explained purely by incomplete mixing and the vapour pressure controlled evaporation of SOA monomers. We note however, that when a nearly non-volatile component is introduced and the SOA is treated as solid like, evaporation rates significantly decrease.

3.3.2 Evaporation of semi-solid SOA particles with an oligomer coating

Here we examine whether the observed slow evaporation rate can be modelled by introducing a protective oligomer monolayer surface whose decomposition rate determines the evaporation rate. Upon monomer evaporation, the concentration of oligomers will increase at the surface (Widmann et al., 1998). The evaporation is first controlled by relatively weakly bound surface oligomers which gradually are replaced by more tightly bound oligomers from the bulk phase (bulk oligomer).

Liggio and Li (2006) found that pinonaldehyde (which is relatively volatile) is rapidly taken up on acidic aerosol surfaces due to formation of organosulfates. In the experiments by Vaden et al. (2011) no acid seed aerosol was used. However, uptake of carboxylic acids can still give a weakly acidic environment. Hence, adsorption of pinonaldehyde (or some other gas phase organic compounds) followed by acid catalysed oligomerization could potentially form a low-volatility coating. Alternatively, low-volatility dimers can form in the gas phase (e.g. R5) and then adsorb on the particle surfaces. Such a coating could possibly explain why the evaporation rate is substantially slower in the measurements than for the modelled monomer SOA particles (Fig. 9).

In order to test the general mechanism principle, we model the formation of a weakly bound oligomer surface layer coating as reactive uptake of pinonaldehyde and assuming it forms oligomer with any organic monomer molecule containing hydrogen peroxide or aldehyde functional groups (R1b and R2b). In addition, we assume that the surface layer oligomer forms a separate organic phase with a fractional surface coverage (θ_s). In this picture, the monomers do not condense on the oligomer-covered surface and the oligomers having a negligible diffusion rate remain on the surface when the par-

ACPD
14, 769–869, 2014

ticles grow. The fractional oligomer surface coverage is then mainly controlled by the formation and decomposition rates of surface layer oligomers.

We model the reactive uptake of pinonaldehyde assuming that the adsorbed pinonaldehyde concentration at the oligomer-free particle surface $(1 - \theta_s)$ is proportional to the pinonaldehyde gas phase concentration (c_{PINAL}(g) in molecules cm^{-3}. With the particle surface monolayer concentration of reactive monomers ($c_{\mathrm{m},i}$(p.s.)) in molecules cm^{-3}, the reactive uptake rate F_{f}(p.s) (surface layer dimer formation rate) is given by Eq. (33),

$$F_{\mathrm{f}}(\mathrm{p.s.}) = k_{\mathrm{f}}(\mathrm{p.s.})c_{\mathrm{m},i}(\mathrm{p.s.})c_{\mathrm{PINAL}}(\mathrm{g})(1 - \theta_{\mathrm{s}}) \quad (33)$$

and the surface oligomers decompose to monomers using a first order degradation rate constant (k_{d}(p.s.)) (see Eq. 12).

Additionally, in the first simulations we include three bulk oligomerization mechanisms: peroxyhemiacetal formation (R1a), hemiacetal formation (R3) and ester formation (R4), with one oligomerization rate constant $k_{\mathrm{f}}(p)$. The bulk oligomer concentration is determined by the formation and decomposition rates, particle age, monomer evaporation, and to less extent by the monomer composition. The monomer SOA is treated as a semi-solid tar like mixture ($D_{0,\mathrm{monomer}} = 5 \times 10^{-17}$ cm^2 s^{-1}) and the oligomer SOA as solid ($D_{0,\mathrm{dimer}} = 0$ cm^2 s^{-1}).

First order decomposition rates are $k_{\mathrm{d}} = 3/2\,\mathrm{h}^{-1}$ and $k_{\mathrm{d}} = 1/3.2\,\mathrm{h}^{-1}$, for the surface and bulk oligomers, respectively. The oligomerization rates were set to 3×10^{-15} cm^3 molecules^{-1} and 1.2×10^{-27} cm^3 molecules^{-1} for the surface and bulk, respectively. With these, $\sim 90\,\%$ of the particles' surface is coated and $\sim 3\,\%$ of bulk phase is comprised of long-lived oligomer (independent of particle size) at the time when the particles are introduced into the evaporation chamber (see Fig. S7).

In Fig. 10, we compare the modelled and observed evaporation rates of fresh and aged α-pinene SOA particles. With $\sim 90\,\%$ of the particle surface covered with oligomer, very little monomer needs to evaporate in order for the particle surface layer to be completely covered with oligomer that slows the initial evaporation rate. With the

ACPD
14, 769–869, 2014

Nannoolal method, the model substantially underestimates the initial evaporation rate. The reason for this is the small mass fraction of the low-volatility monomer C922OOH that accumulate in the particle surface layer (see Sect. 3.3.1). We have in addition, performed a simulation without surface oligomer formation using the Nannoolal method. However, for this simulation the solid-like 250 nm particles lose ~ 20 % of their mass in 2 min, which is inconsistent with the measurements (see Fig. S8 in the Supplement).

Because the gas phase is effectively removed in the evaporation chamber, the reactive uptake of pinonaldehyde stops (Eq. 33) and the surface oligomer is gradually lost during the first evaporation stage. After ~ 2 h of evaporation almost all short-lived surface oligomer is lost and replaced by the longer-lived and continuously forming bulk phase oligomer (see Fig. S7b). This is when the second slow evaporation stage starts. At this point, the evaporation rate is determined by the decomposition rate of bulk oligomer that now comprises the surface layer and is therefore almost independent of the particle size (Fig. 10). However, since the bulk-phase oligomer concentrations are nearly size independent in these simulations, a larger mass fraction of the small particles needs to evaporate in order for their surface layer to be filled with the longer-lived bulk phase oligomer. Hence, if the first evaporation stage is nearly size-independent the bulk oligomer concentration in the small particles needs to be larger.

Additionally, the differences between modelled evaporation rates of aged and fresh particles are substantially larger than observed (Fig. 10). In the model, oligomer mass concentrations continue to increase after the particles are formed (see Fig. S9 in the Supplement), such that at 12 h of aging the oligomer mass fraction reaches ~ 15 % compared to ~ 3 % at 1.5 h, requiring significantly less monomer to evaporate before the particle surface layer is dominated by oligomers formed in the bulk.

In Sect. 3.3.1 we found that the relative mass fractions of the least volatile condensable compounds increase with decreasing particle size, when SOA particles of different size are formed in the presence of each other. Hence, if low-volatility dimers are formed in the gas phase (e.g. by peroxy radical termination reactions R5), or if it is the least volatile monomers which preferentially form oligomer SOA in the particle phase, the

ACPD
14, 769–869, 2014

oligomer SOA mass fraction will increase with decreasing particle size. Low volatility organic compounds generally contain more functional groups, which can be involved in different particle phase oligomerization processes.

Below we test whether bulk phase oligomerization between the least volatile monomers can explain the size independent evaporation loss rates measured by Vaden et al. (2011).

In order to decrease the ageing effect on the particle evaporation behaviour and achieve nearly particle size independent evaporation rates, we now use a relatively rapid particle phase oligomerization formation rate ($k_f = 10^{-23}\,\mathrm{cm}^{-3}$ molecules), between the two least volatile MCMv.3.2 α-pinene oxidation products that have a substantial contribution to the SOA formation (C922OOH and C921OOH). We use a bulk oligomer degradation rate of $1/22\,\mathrm{h}^{-1}$.

Figure 11 shows the modelled evaporation rates of fresh and aged SOA particles with diameters of ~ 160 nm and ~ 250 nm, when considering oligomerization between C922OOH and C921OOH, and surface layer oligomerization by reactive uptake of pinonaldehyde (Eq. 33). In this scenario, the modelled evaporation rates are nearly identical with the observations. They are nearly size-independent and aging has only a moderate effect on the evaporation behaviour. The oligomer mass fractions in the different particle layers (for the two selected particle sizes), at the start and after 1 h of evaporation is given in Fig. S10 in the Supplement.

We can conclude that the model is able to reproduce the main features of the measured evaporation losses of SOA particles from Vaden et al. (2011) if:

1. A relatively weakly bonded oligomer coating material is formed on the particle surface layer before the particles are introduced into the evaporation chamber. This coating material may form either by condensation of dimers formed in the gas phase or by a reactive uptake process on the particle surfaces.

2. A relatively small mass fraction of low-volatility relatively long-lived oligomers, accumulate (because of negligible oligomer diffusion rates) in the particle surface

ACPD
14, 769–869, 2014

layers upon evaporation. In order to explain the observed relatively small influence of aging on the SOA particle evaporation loss rates these oligomers need to be formed by a relatively rapid and selective oligomerization mechanism.

3. The oligomer bulk phase mass fraction near the particle surface is higher in the small particles compared to the large ones. As illustrated by the model simulations, this is possible (because of the Kelvin effect) if this oligomer material preferentially is formed from the least-volatile monomer compounds. But it could also be explained by oligomer formation by a reactive uptake mechanism or by an oligomerization process in the gas phase (e.g. R5).

3.3.3 Evaporation of particles composed of equal amount of monomer SOA and oligomer SOA.

Finally, we evaluate a third possible explanation to the observed slow, particle size independent and almost particle age independent SOA evaporation loss rates. In this hypothesis, oligomers comprise significant fraction ($\sim 50\,\%$) of the particles' mass prior to the transfer of particles into the evaporation chamber (see e.g. Gao et al., 2004). In this case, monomer evaporation dominates the first evaporation stage, which leads to increased oligomer concentration at the particle surface layer, forming a high viscosity barrier that slows evaporation (modelled with the obstruction theory (Eq. 19)). The bulk phase oligomers are partly mixed by diffusion with the liquid-like monomers. The second, slow evaporation stage starts when nearly all monomers are lost and the evaporation rate is determined by the oligomer formation/decomposition rates and transport of the degradation products (monomers) to the surface layer.

In order to test this hypothesis we need to find a group of monomer compounds that can comprise $\sim 50\,\%$ of the SOA mass when they oligomerize. For this, we decided to use 26 of the least volatile organic compounds containing at least one alcohol or carboxylic acid functional group, and assume that they form oligomer by an ester formation mechanism (R4), with a formation rate of 5×10^{-24} cm^3 molecules^{-1} and

ACPD
14, 769–869, 2014

a decomposition rate of $1/11\,h^{-1}$. The MCMv3.2 names of the selected compounds are given in Table S1 in the Supplement. The diffusion coefficients for monomer and oligomer were estimated with the Stoke–Einstein relationship and a monomer SOA viscosity of 5.7×10^{5} Pa s ($D_{0,\mathrm{monomer}} \approx 10^{-14}\,cm^2\,s^{-1}$, $D_{0,\mathrm{dimer}} \approx 7\times10^{-15}\,cm^2\,s^{-1}$). The diffusion coefficients were chosen to assure dimer enriched particle surface, while allowing monomer evaporation during the first evaporation stage possible.

Figure 12 shows the modelled evaporation rates for fresh (1.5 h) and aged (12 h) ~ 150 nm and ~ 250 nm particles for this paradigm. The early evaporation rate is governed by the monomer diffusion rate to the surface. The small particles have a shorter characteristic time of mass-transport than the large particles (see Sect. 1). This is the reason why the loss rate during the first hour is somewhat larger for the ~ 150 nm particles than the ~ 250 nm particles. When most of the monomers have evaporated (after ~ 4 h for the modelled 150 nm particles and ~ 8 h for the 250 nm particles), the second slow evaporation-stage begins. This stage is determined by oligomer degradation, formation and by the diffusion of monomer to the particle surface layer. Again, because of the shorter characteristic time of mass-transport for the small particles, the evaporation losses of the small particles are somewhat larger (steeper slope of the curves in Fig. 12). This is not consistent with the measurements.

From these simulations we can conclude that the observed nearly size independent evaporation rates can probably not be explained purely by an initial particle phase mass transfer limited evaporation of the monomer SOA, followed by a slow decomposition of the remaining (~ 50 % by mass) oligomer SOA.

3.4 SOA formation from oxidation of *m*-xylene

Here we model the SOA formation from an *m*-xylene oxidation experiment (Exp. P2 in Nordin et al., 2013). The experiment was conducted in a $6\,m^3$ Teflon chamber in the Aerosol Laboratory at Lund University. The experiment started with dark conditions by adding $(NH_4)_2SO_4$ seed aerosol into the chamber (~ $20\,\mu g\,m^{-3}$), followed by ~ 40 ppb

ACPD
14, 769–869, 2014

NO and ~ 240 ppb *m*-xylene. Approximately 30 min before the UV-lights were turned on (~ 90 min after the start of the experiment), $(NH_4)_2SO_4$ particles were added a second time in order to achieve the target $(NH_4)_2SO_4$mass of ~ 20 µg m^{-3}.

The seed aerosol was formed by nebulizing an $(NH_4)_2SO_4$–water solution and then drying the droplets. Before the dry $(NH_4)_2SO_4$ particles were introduced into the chamber they were passed through a bi-polar charger in order to achieve a well-defined nearly Boltzmann distributed charge distribution (Wiedensohler et al., 2012). The experiment was performed at a temperature of 22 °C ±2 °C, dry conditions (RH of 3–5 %) and in the presence of UV-light with an experimentally derived NO_2 photolysis rate of 0.2 min^{-1}. The experimental set-up has been described in detail by Nordin et al. (2013). The measured UV-light spectrum (320–380 nm) is given in the Supplement to Nordin et al. (2013).

In the model we used a temperature of 21 °C and a RH of 5 %. The photolysis rates were calculated with the recommended cross sections and quantum yields from MCMv3.2 and the measured 1 nm resolution UV-spectrum from Nordin et al., 2013, with a total light intensity of 23 W m^{-2} which gives a NO_2 photolysis rate of 0.20 min^{-1}.

3.4.1 Particle deposition loss rates

To be able to quantify the effect of dry deposition on the estimated SOA formation from chamber experiments, the deposition losses of particles to the chamber walls needs to be evaluated. The dry deposition depends both on the friction velocity (u^*), the particle size and charge distributions, the mean electrical field strength ($\overline{E}$) in the chamber, and the chamber surface area to volume ratio (see Sect. 2.2.3). $\overline{E}$ and u^* are commonly not known, but can be estimated by fitting the model to particle number size distribution measurements. For this purpose an experiment with $(NH_4)_2SO_4$ seed particles but without condensable organic compounds was performed.

As the experiments in the chamber proceed, the chamber surface area to volume ratio increased because of instrument sampling and leakage out from the chamber

ACPD
14, 769–869, 2014

due to a small over pressure inside the chamber (see Nordin et al., 2013). We estimate the chamber volume loss rates ($\Delta V/\Delta t$) during the experiments to $0.8 \pm 0.2\,m^3\,h^{-1}$.

With a $\Delta V/\Delta t$ of $0.8\,m^3\,h^{-1}$, coagulation and deposition, and a mean electrical field strength of $50\,V\,cm^{-1}$ and a friction velocity of $0.05\,m\,s^{-1}$, ADCHAM is able to nearly reproduce the measured $(NH_4)_2SO_4$particle number size distributions (Fig. 13a), the temporal evolution of the total particle number (Fig. 13c) and volume concentrations (Fig. 13d). The coagulation has no direct influence on the particle volume concentration but is important for the particle number concentration at the end of the experiment. In the beginning of the experiment the charged smallest particles are rapidly deposited to the chamber walls resulting in a high effective wall deposition loss rate (k_w (s^{-1})) (Fig. 13b). But, as the experiment proceeds the fraction of charged particles (especially the small ones) decreases in the air. At the same time the surface area to volume ratio increases in the chamber, which in turn increases the deposition loss rates of all particle sizes (see the gradual upward displacement of the curves in Fig. 13b). Recharging of particles by collision with air ions was not considered in the model.

After the tuning of the dry deposition loss rates on the pure seed aerosol experiments we used ADCHAM to simulate the SOA formation experiment with *m*-xylene as precursor (Nordin et al., 2013). However, if we use the same ($\Delta V/\Delta t$), $\overline{E}$ and u^* as in the pure seed particle deposition experiment, the model underestimates the seed aerosol mass loss (especially during the first 2 h after the UV-lights are turned on), but substantially overestimates the particle number concentration losses before the UV-lights are turned on.

The heating of the air by the UV-lights and the air condition units which blow on the outer chamber walls can produce an increased mixing within the chamber. Therefore, before the UV-lights are turned on u^* may be smaller. By decreasing $u^*$to $0.01\,m\,s^{-1}$before the UV-lights are turned on the model better captures the measured initial particle number concentration losses.

Another important difference between the pure seed particle experiment and the *m*-xylene precursor experiment is that the latter experiment was performed during almost

ACPD
14, 769–869, 2014

twice as long time (∼ 6 h). Hence, the effect of particle recharging when colliding with air ions may be more important to consider. Furthermore, the chamber volume during the end of the *m*-xylene experiment was substantially smaller (1.5–2 m^3). This might have increased the effective mean electrical field strength within the chamber (see Sect. 2.2.3). In the model we try to account for this by calculating $\overline{E_t}$ (at time t) as the quotient between the initial mean electrical field strength $\overline{E_0}$ (50 $V\,cm^{-1}$) and the relative change of the approximate distance between the roof and ceiling (h) of the chamber (h_t/h_0) (which is approximately equal to the relative chamber volume change (V_t/V_0)) (Eq. 34).

$$\overline{E_t} = \frac{\overline{E_0}}{h_t/h_0} \approx \frac{\overline{E_0}}{V_t/V_0} \tag{34}$$

Figure S11 in the Supplement compares the modelled and measured (with AMS and scanning mobility particle sizer (SMPS)) temporal evolution of the sulphate seed particle mass concentration, particle number concentration and the particle number size distribution, and the modelled initial and final effective dry deposition loss rates. The model results are from simulations with, $\overline{E_t} = 50\,V\,cm^{-1}$ and $u^* = 0.05\,m\,s^{-1}$ or $\overline{E_t}$ calculated with Eq. (34) and with $u^* = 0.01\,m\,s^{-1}$before the UV-lights are turned on. With the latter values the model shows substantially better agreement with the measured temporal evolutions of the sulphate seed aerosol mass concentration. However, the model still overestimates the particle number concentration loss rates (especially after the UV-light are turned on). For the model simulations presented below we will use Eq. (34) to estimate $\overline{E_t}$, and $u^* = 0.01\,m\,s^{-1}$before the UV-lights are turned on and $u^* = 0.05\,m\,s^{-1}$after the UV-lights are turned on.

3.4.2 Gas - particle partitioning and heterogeneous reactions

Since the *m*-xylene experiment was performed at dry conditions the $(NH_4)_2SO_4$ seed particles will initially be in a solid crystalline phase. Therefore, we assume that no

ACPD
14, 769–869, 2014

material is mixed between the crystalline solid salt cores and the SOA coating (see e.g. Fig. 1a in Bertram et al., 2011). Hence, in the model there will be no salting-out effect (increase of the nonpolar organic compound activity coefficients caused by NH_4^+, SO_4^{2-} and HSO_4^- from the seed aerosol particles) (see discussion in Sect. 3.2 on possible salting-out effects of NH_4^+).

In total we considered 112 potentially condensable ($p_0 < 1$ Pa) non-radical organic MCMv3.2 compounds. The pure-liquid saturation vapour pressures were calculated with either the SIMPOL (Pankow and Asher, 2008) or the method from Nannoolal et al. (2008). We also used a third (semi-empirical) method to model the SOA formation. This method considers in total three oxidation products with vapour pressures and molar based stoichiometric yields (α_i) derived from the parameterizations for low and high NO conditions from Ng et al. (2007). For this we assume that the condensable organic compounds have a molar mass of 200 g mol^{-1}. The two most volatile compounds ($p_{0,1} = 6.4\times10^{-6}$ Pa, $\alpha_1 = 0.021$ and $p_{0,2} = 1.7\times10^{-4}$ Pa, $\alpha_2 = 0.061$) represent the volatility distribution of the condensable oxidation products formed through the $RO_2 + NO$ pathway. The third non-volatile product ($p_{0,3} = 0$ Pa, $\alpha_3 = 0.245$) represent the generally less volatile organic compounds formed through the $RO_2 + HO_2$ pathway. The gas phase was still modelled with the MCMv3.2. The fraction of condensable organic compounds which was formed through the $RO_2 + HO_2$ pathway (product 3) was derived with the ratio $(k_{RO_2+HO_2}[HO_2]/(k_{RO_2+NO}[NO] + k_{RO_2+HO_2}[HO_2])$ as proposed by Ng et al. (2007).

The partitioning of the condensable organic compounds to the wall deposited particles and the Teflon walls were modelled according to the procedure described in Sect. 2.2.3. The uptake onto the Teflon film and the particles deposited on the chamber walls depends on the laminar layer width adjacent to the chamber walls (Δx). The uptake (adsorption) on the Teflon film also depends on the first order loss rate from the near wall gas phase to the walls ($k_{g,w}$) and the desorption rate from the Teflon surfaces out to the thin layer next to the chamber walls ($k_{w,g,i}$) (Eq. 4). In Sect. 3.4.4 we

ACPD
14, 769–869, 2014

test different values of Δx, $k_{g,\,w}$ and $k_{w,\,g,i}$ in order to find the best possible agreement between the modelled and the measured SOA formation.

Because coagulation has a considerable influence on the modelled particle number size distribution (see Fig. 13) we will consider this process as well. However, with the current version of ADCHAM coagulation cannot be combined with the complete kinetic multi-layer model (see Sect. 2.2.2). Hence, for the simulations presented in this section the particles were only divided into a solid seed particle core, and a second (well-mixed) bulk layer and a surface monolayer which are composed of the condensable organic compounds. Additionally (if specified) we also consider the adsorption and desorption of $O_3$and NO_2, the mass transfer limited diffusion of O_3 and NO_2 from the sorption layer into the particle bulk, and the particle phase reactions between O_3 and unsaturated organic compounds (see Sect. 2.4.2) or between NO_2 and oxidized aromatic compounds (see Sect. 3.4.3).

Table 1 in Sect. 2.4.2 gives the model parameter values used for O_3 uptake. For the simulations presented here the diffusion coefficient of ozone (D_{0,O_3}) was set to values between 10^{-7} and $10^{-8}\,cm^2\,s^{-1}$ (semi-solid SOA (see e.g. Table 1 in Shiraiwa et al., 2011)), and the reaction rate constants between ozone and the unsaturated (non-aromatic carbon-carbon double bond) organic compounds (k_{O_3}) were varied between 10^{-16} and $10^{-17}\,cm^3$ molecules$^{-1}\,s^{-1}$. This can be compared with the measured k_{O_3} of $10^{-16}\,cm^3$ molecules$^{-1}\,s^{-1}$ for the heterogeneous ozonolysis of oleic and palmitoleic acid (Huff Hartz et al., 2007). The formed particle phase oxidation products were assumed to be non-volatile, which likely is an acceptable assumption if the oxidation products rapidly react and form dimer SOA (see e.g. Maksymiuk et al., 2009). Apart from increasing the SOA mass formation and changing the chemical composition of the SOA these heterogeneous reactions may also serve as an additional ozone sink (which is not accounted for by the MCMv3.2 gas phase chemistry mechanism).

Additionally, we will also test peroxyhemiacetal and hemiacetal dimer formation (Reactions R1a and R3) in the particle phase.

ACPD
14, 769–869, 2014

3.4.3 Gas phase chemistry and influence from chamber walls and heterogeneous reactions

Bloss et al. (2005a, b) have previously shown that the MCMv3.1 (without particle SOA formation and particle phase chemistry) generally overestimates the ozone concentration and underestimates the OH concentration during oxidation of light aromatic compounds (e.g. xylene and toluene). Hence, for these systems MCM also tends to underestimate the NO and hydrocarbon oxidation (loss) rates. In order to account for the missing OH source Bloss et al., 2005b had to include an artificial OH source of 4×10^8 molecules cm^{-3} s^{-1} when modelling a toluene oxidation experiment from the EUPHORE chamber.

Conversion of NO_2 to HONO on the organic particle surfaces may partly explain the discrepancy between the modelled and measured particle phase chemistry (Bloss et al., 2005b). These reactions have been observed on diesel exhaust particles (Gutzwiller et al., 2002) and on organic aerosol surfaces e.g. by George et al. (2005). Metzger et al. (2008) instead proposed that the NO_2 primarily is converted to HONO on the Teflon chamber walls.

In this work we will test the heterogeneous NO_2 to HONO conversion mechanism. Bloss et al. (2005b) modelled this mechanism using a constant reaction probability (γ_{HONO}) of 0.025 for the NO_2 molecules which collide with a particle. In this work we model this proposed mechanism in a more detailed way by considering the adsorption, diffusion and reaction of NO_2 with specific organic compounds in the particle phase. NO_2 has approximately the same Henry's law coefficient for dissolution in water (Seinfeld and Pandis, 2006) and molecule size as O_3. Hence, for these simulations, we will use the same parameter values for NO_2 (e.g. Henry's law coefficient and diffusion coefficient) as specified for O_3 in Sect. 3.4.2 and in Table 1.

Gutzwiller et al. (2002) suggested that the organic compounds which react with NO_2 in the particle phase and form HONO are oxygenated aromatics (e.g. 2-methoxyphenol). Hence, we assume that it is only the compounds that contain an

ACPD
14, 769–869, 2014

aromatic ring which will be oxidized by NO_2 and form HONO. The organic oxidation products formed from these heterogeneous reactions were assumed to be non-volatile.

The NO_2 to HONO conversion mechanism was considered both on the particles deposited on the chamber walls and in the air. We will also test an additional photo-enhanced background reactivity caused by HONO release from the chamber walls (Rohrer et al., 2005). The strength of the HONO emissions (from the walls to the near surface gas phase) in the Lund Teflon chamber (Nordin et al., 2013) was estimated to be 4.6×10^8 molecules $cm^{-2}\,s^{-1}$. This value is based on the estimated HONO wall production rate of 9.1×10^6 molecules $cm^{-3}\,s^{-1}$ in Metzger et al. (2008) and their chamber volume to surface area characteristics (Paulsen et al., 2005).

Analogous to the MCM light aromatic model simulations by Bloss et al. (2005a, b) we underestimate the OH and overestimate the maximum O_3 concentration, without tuning the MCM gas phase chemistry (Fig. 14). MCMv3.2 also underestimate the initial O_3 formation rate, the amount of reacted *m*-xylene and the rapid NO to NO_2 conversion which starts approximately 20 min after the UV-lights were turned on. Therefore, analogous to Bloss et al. (2005b) we decided to include an artificial OH source, in our case with a rate of 10^8 $cm^{-3}\,s^{-1}$ from 20 min after the UV-light were turned on until the end of the experiment. This substantially improves the agreement between the modelled and measured NO, NO_2, O_3 and *m*-xylene concentrations. However, the model still substantially overestimates the maximum O_3 concentration.

The poor agreement between the modelled and measured NO_2 in the latter half of the experiment (Fig. 14b) is because of the interference from peroxy acyl nitrates (PAN), HNO_3, HONO, N_2O_5 and other nitrate containing compounds in the chemiluminescence instrument used (see Nordin et al., 2013 and references there in).

Figure 14 also shows the results from a simulation where we additionally include HONO emissions from the chamber walls. Because the surface area to volume ratio increases during the experiments (~ 5 times) these emissions have an increasing influence on the modelled gas phase chemistry. With HONO emissions and the OH source, the OH concentration at the end of the model run is 1.5×10^6 cm^{-3}, while without these

ACPD
14, 769–869, 2014

emissions but with the OH source the concentration is 7×10^5 cm^{-3}. Hence, with HONO wall emissions more *m*-xylene reacts in the simulation than what is indicated by the gas chromatography – mass spectrometry (GC-MS) measurements. Additionally, the model O_3 concentration becomes even higher.

In order to be able to compare the modelled and measured SOA formation during the experiment it is crucial that we are able to accurately simulate both the amount of *m*-xylene which is consumed and the fraction of RO_2 which reacts with HO_2 and NO, respectively (see e.g. Ng et al., 2007 and Kroll and Seinfeld, 2008). Hence, if not otherwise specified we included the artificial OH source but not any HONO emissions from the chamber walls. With this model set-up, the cumulative fraction of the *m*-xylene first generation RO_2 oxidation products which have reacted with HO_2 at the end of the experiment is about ~ 65 %. When we also include HONO wall emissions this value is ~ 50 % and with the non-tuned MCMv3.2 chemistry we get a value of ~ 35 % (see Fig. S12 in the Supplement).

In order to test whether HONO formation from heterogeneous reactions between NO_2 and oxidized aromatic compounds can improve the agreement between the modelled and measured O_3 concentration, we performed a simulation with what we believe are upper estimates of the reaction rates between NO_2 and the oxidized aromatic compounds and the NO_2 diffusion coefficient ($k_{NO_2} = 10^{-15}$ cm^{-3} s^{-1} and $D_{0,NO_2} = 10^{-7}$ cm^2 s^{-1}). With these values ~ 60 % of the aromatic SOA was oxidized by NO_2. The formed (in the model non-volatile) oxidation products comprise 20 % of the total SOA mass in the end of the simulation (Fig. S13a in the Supplement). Still, this has only a moderate influence on the HONO concentration (Fig. S13b) and the NO_2 and O_3 decrease is equal or less than ~ 1 % (Fig. S13c and d).

Figure S13d also shows the modelled O_3(g) concentration when including heterogeneous reactions between O_3 and the unsaturated organic compounds ($k_{O_3} = 10^{-16}$ cm^{-3} s^{-1} and $D_{0,O_3} = 10^{-7}$ cm^2 s^{-1}). For this simulation ~ 98 % of the unsaturated organic compounds in the particle phase were oxidized by O_3 and the formed

ACPD
14, 769–869, 2014

non-volatile SOA products comprise 37 % of the total SOA mass. However, comparable to the heterogeneous NO_2 to HONO conversion this has a very small influence on the modelled O_3(g) concentration (~ 1 % decrease). Hence, we can conclude that it seems unlikely that heterogeneous reactions between NO_2 and oxidized aromatic compounds and/or between O_3 and the unsaturated organic compounds can explain why measurements generally gives much lower O_3(g) concentrations than MCM model. However, as will be shown in Sect. 3.4.4 these heterogeneous reactions can still be important for the amount and type of SOA which is formed.

3.4.4 SOA formation, properties and the potential influence from chamber wall effects and heterogeneous reactions

In Fig. 15 we compare the modelled and measured particle volume concentrations during the *m*-xylene experiment. The model results are from simulations with the SIMPOL vapour pressure method. The desorption of condensable organic compounds from the chamber walls was modelled with $C_w/(M_w\gamma_{w,i})$ in Eq. (4) equal to 100 µmol m^{-3}. This value is between those measured by Matsunaga and Ziemann (2010) for 2-alcoholes and 2-ketones (see Sect. 2.2.3). For the model results in Fig. 15a we used a Δx of 0.1 cm and $k_{g,w}$ was set to $1/20\,s^{-1}$ while for the results in Fig. 15b we used a Δx of 1.0 cm and $k_{g,w}$ was set to $1/6\,s^{-1}$. Hence, the model simulation in Fig. 15a represent conditions with only relatively small mass transfer limitations for the gas exchange between the air and the chamber walls and particles on the walls, and a relatively slow uptake of organic compounds directly onto the Teflon walls. The model simulation in Fig. 15b instead represents conditions where the mass transfer limitations between the air and the chamber walls and particles on the walls are substantial while the uptake of gases directly onto the Teflon walls is relatively effective.

The simulations were performed both with and without heterogeneous oxidation of unsaturated organic compounds ($k_{O_3} = 10^{-16}$ cm^{-3} s^{-1} and $D_{0,O_3} = 10^{-8}$ cm^2 s^{-1}). The oxidation products (ox. prod.) from these reactions were assumed to form one

ACPD
14, 769–869, 2014

organic semi-solid phase together with the other organic compounds ($D_{0,\text{monomer}} = 5 \times 10^{-17}\,\text{cm}^2\,\text{s}^{-1}$ and $D_{\text{ox. prod.}} = 0\,\text{cm}^2\,\text{s}^{-1}$).

In the model simulations presented in Fig. 15 it is shown that the model is able to capture the volume loss rates of the seed aerosol and the onset of the SOA formation in the experiment (~ 0.5 h after UV-lights were turned on). However, for all simulations in Fig. 15, ADCHAM underestimates the observed rapid SOA formation between 0.5 and 1.25 h for the particles suspended in air. Additionally, ADCHAM overestimates the total particle volume loss rates of the suspended particle at the end of the experiments, especially without heterogeneous ozonolysis and relatively rapid uptake of organic compounds onto the Teflon walls (Fig. 15b). According to this simulation the particle losses are not only caused by deposition but also evaporation. Heterogeneous ozonolysis or other particle phase reactions allows more gas phase monomers to partition into the particle phase and delay the time when the evaporation and deposition losses dominates over the SOA formation (see Fig. S14 in the Supplement). Additionally, the SOA formed from these particle phase reactions is less volatile (in the model non-volatile) and will therefore decrease the evaporation loss rates (see Sect. 3.3).

Opposite to the simulation results in Fig. 15b, the maximum particle volume is larger without heterogeneous ozonolysis in Fig. 15a. For these simulations the SOA formation onto the wall deposited particles is more efficient ($\Delta x = 0.1$ cm) and the gas uptake onto the Teflon walls smaller. The wall deposited particles may not always serve as a sink of SOA but can also become a source of condensable organic compounds from the walls to the air. This is especially the case if the formed SOA is relatively volatile. The more volatile the SOA is, the smaller the SOA fraction found on the wall deposited particles will be. Hence, while the formed total SOA mass (air + walls) is larger with heterogeneous reactions in Fig. 15a, the SOA mass formed on the particles in the air is smaller (see also Fig. S15 in the Supplement).

Figure S16 in the Supplement compares the modelled particle volume from simulations with the SIMPOL and Nannoolal vapour pressure method or the semi-empirical two product model parameterization (see Sect. 3.4.2). The model simulations were

ACPD
14, 769–869, 2014

performed with a Δx of 0.1 cm and $k_{g,w} = 1/20\,s^{-1}$. For the simulations with the SIMPOL and the Nannoolal method, heterogeneous ozonolysis was also considered ($k_{O_3} = 10^{-16}\,cm^{-3}\,s^{-1}$ and $D_{0,O_3} = 10^{-8}\,cm^2\,s^{-1}$). From this figure it is evident that both methods give almost identical SOA mass formation at the end of the experiment. However, with the Nannoolal method the onset of the SOA formation is approximately 15 min too late. The reason for this is that the modelled early stage SOA formation is dominated by two MCM oxidation products (MXNCATECH and MXYMUCNO3) (formed through the high NO oxidation pathway (see Sect. 3.4.3)). Both of these compounds have higher vapour pressures with the Nannoolal method (3.1×10^{-3} and 1.31×10^{-4} Pa) compared to the SIMPOL method (1.9×10^{-4} and 7.5×10^{-5} Pa).

With the semi-empirical parameterization, derived from experiments in a similar but larger Teflon chamber (28 m^3) (Ng et al., 2007), ADCHAM gives a too early onset of the SOA formation and overestimate the SOA formation when $k_{g,w} = 1/20\,s^{-1}$. The reason for this is that the three model compounds of this method all have relatively low vapour pressures (see Sect. 3.4.2). Hence, the gas phase is rapidly saturated with respect to all these three compounds and they are effectively taken up by the particles before they are lost to the Teflon wall surfaces. In order to not overestimate the final SOA mass, $k_{g,w}$ need to be much larger $\sim 1\,s^{-1}$. However, then the model substantially underestimates the early stage SOA formation rate.

We also modelled the SOA formation without losses of condensable organic compounds onto the Teflon wall (see Fig. S17 in the Supplement). With a Δx of 0.1 cm ADCHAM is now able to capture the rapid early stage SOA formation in the chamber. However, the final particle volume concentration in the air is overestimated with ~ 40 %. If we instead assume that the gas particle partitioning onto the chamber wall deposited particles is identical to the uptake onto the particles suspended in the air ($\Delta x = 0$ cm) (see Sect. 2.2.3 and references there in), the model again substantially underestimates the early stage SOA formation rate, while it gives reasonable particle volume concentrations at the end of the simulation.

ACPD
14, 769–869, 2014

Finally we also tested if a relatively rapid oligomerization process in the particle phase could improve the agreement with the modelled and measured SOA formation. For these simulations we again use the SIMPOL vapour pressure method and assume that peroxyhemiacetal and hemiacetal dimers (R1a and R3) form in the particle phase with a reaction rate coefficient of $10^{-22}\,\mathrm{cm^3\,s^{-1}}$. Additionally, in order to shift the equilibrium toward the particle phase (which might explain the rapid early stage SOA formation seen in the experiment) we assume that the oligomers and monomers form one mixed phase.

Figure 16 shows the modelled particle volume concentrations when considering peroxyhemiacetal and hemiacetal dimer formation and with $\Delta x = 0$ or 0.1 cm and $k_{\mathrm{g,\,w}} = 0$ or $1/15\,\mathrm{s^{-1}}$. Without gas phase losses onto the Teflon walls and ideal uptake onto wall deposited particles ($\Delta x = 0\,\mathrm{cm}$) the model is able to capture the rapid early stage SOA formation seen in the experiment. After this the modelled particle volume concentration in the air continues to increase slowly for additionally $\sim 2\,\mathrm{h}$, while in the experiment the measured particle volume slowly decreases.

With mass transfer limited diffusion and losses of condensable organic compounds from the near wall gas phase to the Teflon walls ($\Delta x = 0.1\,\mathrm{cm}$ and $k_{\mathrm{g,\,w}} = 1/15\,\mathrm{s^{-1}}$) the model results are in better agreement with the measurements in the end of the experiment and can nearly reproduce the rapid SOA formation in the beginning of the experiment.

Hence, these simulations indicate that relatively rapid heterogeneous reactions (either oligomerization or oxidation) are required in order to explain the observed rapid SOA formation in the beginning of the *m*-xylene oxidation experiment. Still, the model cannot fully explain the sharp transition between the rapid SOA formation between 0.5 and 1.25 h after the UV-light is turned on and the slow almost linear volume (mass) loss observed during the latter half of the experiment.

In Fig. 17 we compare the temporal evolution of the modelled SOA formation without wall losses to the chamber walls (ideal chamber), with the SIMPOL, Nannoolal or the semi-empirical parameterization method from Ng et al. (2007). The figure also

ACPD
14, 769–869, 2014

illustrates the influence from heterogeneous ozonolysis (O_3 ox.) of unsaturated organic compounds ($k_{O_3} = 10^{-16}\,cm^{-3}\,s^{-1}$ and $D_{0,O_3} = 10^{-8}\,cm^2\,s^{-1}$) and peroxyhemiacetal and hemiacetal oligomer formation ($k_f = 10^{-22}\,cm^3\,s^{-1}$). We have also included the measured wall loss corrected SOA mass (SOA mass scaled with the measured relative sulphate loss rate from the time when the UV-lights are turned on) (see Sect. 2.2.3).

The simulation with SIMPOL and no heterogeneous reactions gives best agreement with the measured final SOA mass formation (70 and 65 $\mu g\,m^{-3}$, respectively). However, this simulation substantially underestimates the SOA formation during the start of the experiment. The best agreement between the model and measurements in the beginning of the experiment is instead reached when we include relatively rapid oligomerization in the particle phase. The results from this simulation also show surprisingly good agreement with the model simulation using the semi-empirical parameterizations from Ng et al. (2007). This again indicates that heterogeneous reactions are likely to be important for the SOA formation. The larger SOA formation from these model simulations compared to the measurements can likely be attributed to substantial gas phase losses directly onto the Teflon walls in the chamber. This effect will be especially pronounced in the end of the experiment when the surface area to volume ratio is large (see Sect. 3.4.1). Hence for this experiment, the model simulations indicate that the wall corrections (which assume continued uptake of condensable organic compounds onto the wall deposited particles) do not give an upper estimate of the actual (atmospheric relevant) SOA formation (see Sect. 2.2.3).

4 Summary and conclusions

We have developed a novel aerosol dynamics, gas- and particle- phase chemistry model for chamber studies (ADCHAM). ADCHAM combines the detailed gas phase chemistry from MCMv3.2, a kinetic multilayer module for diffusion limited transport of compounds between the gas phase, particle surface and particle bulk phase, and an aerosol dynamics and particle phase chemistry module which is based on the AD-

ACPD
14, 769–869, 2014

CHEM model (Roldin et al., 2011a) but with important updates, among others process-based algorithms for: non-ideal interactions (salt effects) between water, organic and inorganic compounds, acidity catalysed oligomerization, and oxidation of organic compounds in the particle phase.

In this work we have illustrated the usefulness of ADCHAM in studying potentially influential but poorly known processes, i.e. different oligomerization mechanisms, organic salt formation, salting-out effects, heterogeneous oxidation reactions and mass transfer limitations between the gas-particle phase, between the particle surface and particle bulk phase, and within the particle bulk phase. All these processes influence the modelled SOA formation and chemical and physical properties (e.g. volatility, phase state, oxidation state and hygroscopicity).

Additionally, we have also shown how ADCHAM can be used to study the influence of the chamber wall effects on the SOA mass formation, particle number size distribution and gas phase chemistry. These effects are important to constrain because current knowledge concerning SOA formation in the atmosphere is to a large extent based on smog chamber experiments, and global climate models and chemistry transport models rely on simplified semi-empirical parameterizations on SOA formation derived from these experiments.

The most important findings from the model simulations performed in this article are:

1. The effect of NH_3(g) on the α-pinene SOA properties and formation depends on: (1) the reactive uptake of carboxylic acids and NH_3(g) from the gas phase, (2) the viscosity of the SOA particles (ammonium and organic compound diffusion rates) and (3) the salting-out effects of NH_4^+. In order to distinguish between these effects we recommend future experiments with AMS, in which the SOA particles are exposed to NH_3in the absence of gas phase carboxylic acids. In the model simulations the organic salts between ammonium and carboxylic acids are involved in the initial growth of the particles. Hence, these model simulations supports the theory that organic salts e.g. between ammonium or amines and carboxylic acids

ACPD
14, 769–869, 2014

may be important for the early stage of nanoparticle growth in the atmosphere (Smith et al., 2008; Barsanti et al., 2009 and Smith et al., 2010).

2. Our modelling of the evaporation experiments on SOA particles formed by α-pinene ozonolysis from Vaden et al. (2011) supports the recent experimental findings that these SOA particles are very viscous (tar like amorphous SOA) (Abramson et al., 2013). In these particles low-volatility oligomer SOA can accumulate in the particle surface layer upon evaporation. With the formation of this low-volatility oligomer coating material ADCHAM is able to reproduce the main features of the observed slow evaporation rates. However, in order for the model to resemble the relatively slow and particle size independent first evaporation stage the particle surface layer needs to be covered with some relatively weakly bonded oligomers already before the evaporation starts. Such an oligomer coating may either be formed by condensation of dimers formed in the gas phase or by a reactive uptake mechanism. Additionally the model simulations illustrates that the mass fraction of oligomer SOA in the bulk phase needs to increase with decreasing particle size to explain the nearly size independent evaporation rates. Because of the Kelvin effect, this may be accomplished if a considerable fraction of the low-volatility oligomers compounds is formed in the gas phase, by a reactive uptake mechanism or if the oligomer SOA generally is formed from the least volatile monomer compounds.

3. Mass transfer limitations between the smog chamber air volume and the chamber walls because of a thin laminar layer adjacent to the walls have large influence on the uptake of gases onto the wall deposited particles or directly onto the walls. If the formed SOA material is semi-volatile the SOA particles on the chamber walls may even start to evaporate and hence become a source of SOA at the end of smog chamber experiments. Paradoxically, heterogeneous reactions which give less volatile SOA and generally more SOA mass will increase the fraction of SOA

ACPD
14, 769–869, 2014

which is found on the chamber walls and can thus even decrease the detectable SOA mass suspended in the chamber air volume.

4. In order to capture the rapid SOA formation observed during the oxidation of *m*-xylene in the Lund University smog chamber we need to consider relatively rapid oligomerization and/or some other heterogeneous reactions (e.g. ozonolysis of unsaturated organic compounds). When considering peroxyhemiacetal and hemiacetal dimer formation in the particle phase, ADCHAM is able to capture both the observed early stage rapid SOA formation in our own *m*-xylene experiment and gives almost identical SOA mass formation as the semi-empirical parameterizations from Ng et al. (2007). This indicates that heterogeneous particle phase reactions are not only important for the SOA properties (e.g. volatility) but also for the amount and formation rates.

Another more general conclusion, which can be drawn from the simulations performed in this work, is that many of the parameters (processes) with large uncertainties (e.g. SOA viscosity, oligomerization rates and mechanisms, pure-liquid saturation vapour pressures, surface tension and chamber wall effects) have large influence on the SOA formation and/or the chemical and physical properties of the SOA. To be able to constrain the uncertainties related to these parameters (processes), the experiments need to be designed where as many variables as possible are varied (e.g. time of aging, temperature, RH, concentrations, dilution, oxidation agents and light intensities). Apart from evaluating experimental results, ADCHAM can be used as a valuable model tool when planning, designing and selecting which experiments and instrumentation are needed in order to be able to answer specific research questions. The *m*-xylene experiment studied in Sect. 3.4 is part of a larger experiment campaign designed in order to study aging of anthropogenic SOA precursors and gasoline car exhausts (Nordin et al., 2013). In that paper an early version of ADCHAM was used to study chamber wall effects, gas phase chemistry and SOA formation before the experiments were performed. Currently we are applying ADCHAM to study the aging of gasoline car ex-

ACPD
14, 769–869, 2014

hausts. We have also started to implement many of the detailed processes (e.g. the kinetic multilayer model, different oligomerization processes and the detailed MCMv3.2 gas phase chemistry) in the ADCHEM model which we use for detailed atmospheric process studies.

Supplementary material related to this article is available online at http://www.atmos-chem-phys-discuss.net/14/769/2014/acpd-14-769-2014-supplement.pdf.

Acknowledgements. This work was supported by the strategic research area MERGE at Lund University, Swedish Research Council for Environment, Agricultural Sciences and Spatial Planning FORMAS through projects 2007-1205, 2008-1467, 2009-615 and 2010-1678, the Swedish Research Council through project 2006-5940and by Metalund, the centre for Medicine and Technology for Working Life and Society, a competence centre at Lund University, Sweden, supported by FAS, the Swedish Council for Working Life and Social Research. Support for A. Zelenyuk was provided by US Department of Energy (DOE), Office of Science, Office of Basic Energy Sciences (BES), Chemical Sciences, Geosciences, and Biosciences Division.

The authors would like to thank prof. Gordon McFiggans research group at the University of Manchester, and especially David Topping, for helpful discussions and for providing the Python script (now a public available function called CompSysProp: http://ratty.cas.manchester.ac.uk/informatics/) to calculate Nannoolal based sub-cooled liquid saturation vapour pressures for all included organic compounds in this paper.

References

Abramson, E., Imre, D., Beránek, J., Wilson, J., and Zelenyuk, A.: Experimental determination of chemical diffusion within secondary organic aerosol particles, Phys. Chem. Chem. Phys., 15, 2983–2991, 2013.

ACPD
14, 769–869, 2014

Ammann, M. and Pöschl, U.: Kinetic model framework for aerosol and cloud surface chemistry and gas-particle interactions – Part 2: Exemplary practical applications and numerical simulations, Atmos. Chem. Phys., 7, 6025–6045, doi:10.5194/acp-7-6025-2007, 2007.

Barley, M. H. and McFiggans, G.: The critical assessment of vapour pressure estimation methods for use in modelling the formation of atmospheric organic aerosol, Atmos. Chem. Phys., 10, 749–767, doi:10.5194/acp-10-749-2010, 2010.

Barsanti, K. C., McMurry, P. H., and Smith, J. N.: The potential contribution of organic salts to new particle growth, Atmos. Chem. Phys., 9, 2949–2957, doi:10.5194/acp-9-2949-2009, 2009.

Bergström, R., Denier van der Gon, H. A. C., Prévôt, A. S. H., Yttri, K. E., and Simpson, D.: Modelling of organic aerosols over Europe (2002–2007) using a volatility basis set (VBS) framework: application of different assumptions regarding the formation of secondary organic aerosol, Atmos. Chem. Phys., 12, 8499–8527, doi:10.5194/acp-12-8499-2012, 2012.

Bertram, A. K., Martin, S. T., Hanna, S. J., Smith, M. L., Bodsworth, A., Chen, Q., Kuwata, M., Liu, A., You, Y., and Zorn, S. R.: Predicting the relative humidities of liquid-liquid phase separation, efflorescence, and deliquescence of mixed particles of ammonium sulfate, organic material, and water using the organic-to-sulfate mass ratio of the particle and the oxygen-to-carbon elemental ratio of the organic component, Atmos. Chem. Phys., 11, 10995–11006, doi:10.5194/acp-11-10995-2011, 2011.

Bloss, C., Wagner, V., Bonzanini, A., Jenkin, M. E., Wirtz, K., Martin-Reviejo, M., and Pilling, M. J.: Evaluation of detailed aromatic mechanisms (MCMv3 and MCMv3.1) against environmental chamber data, Atmos. Chem. Phys., 5, 623–639, doi:10.5194/acp-5-623-2005, 2005a.

Bloss, C., Wagner, V., Jenkin, M. E., Volkamer, R., Bloss, W. J., Lee, J. D., Heard, D. E., Wirtz, K., Martin-Reviejo, M., Rea, G., Wenger, J. C., and Pilling, M. J.: Development of a detailed chemical mechanism (MCMv3.1) for the atmospheric oxidation of aromatic hydrocarbons, Atmos. Chem. Phys., 5, 641–664, doi:10.5194/acp-5-641-2005, 2005b.

Boy, M., Hellmuth, O., Korhonen, H., Nilsson, E. D., ReVelle, D., Turnipseed, A., Arnold, F., and Kulmala, M.: MALTE – model to predict new aerosol formation in the lower troposphere, Atmos. Chem. Phys., 6, 4499–4517, doi:10.5194/acp-6-4499-2006, 2006.

Camredon, M., Hamilton, J. F., Alam, M. S., Wyche, K. P., Carr, T., White, I. R., Monks, P. S., Rickard, A. R., and Bloss, W. J.: Distribution of gaseous and particulate organic composition

ACPD
14, 769–869, 2014

during dark α-pinene ozonolysis, Atmos. Chem. Phys., 10, 2893–2917, doi:10.5194/acp-10-2893-2010, 2010.
Cappa, C. D. and Wilson, K. R.: Evolution of organic aerosol mass spectra upon heating: implications for OA phase and partitioning behavior, Atmos. Chem. Phys., 11, 1895–1911, doi:10.5194/acp-11-1895-2011, 2011.
Chapman, S. and Cowling, T. G.: The Mathematical Theory of Nonuniform Gases, Cambridge University Press, Cambridge, 1970.
Compernolle, S., Ceulemans, K., and Müller, J.-F.: Influence of non-ideality on condensation to aerosol, Atmos. Chem. Phys., 9, 1325–1337, doi:10.5194/acp-9-1325-2009, 2009.
Donahue, N. M., Epstein, S. A., Pandis, S. N., and Robinson, A. L.: A two-dimensional volatility basis set: 1. organic-aerosol mixing thermodynamics, Atmos. Chem. Phys., 11, 3303–3318, doi:10.5194/acp-11-3303-2011, 2011.
Dzepina, K., Volkamer, R. M., Madronich, S., Tulet, P., Ulbrich, I. M., Zhang, Q., Cappa, C. D., Ziemann, P. J., and Jimenez, J. L.: Evaluation of recently-proposed secondary organic aerosol models for a case study in Mexico City, Atmos. Chem. Phys., 9, 5681–5709, doi:10.5194/acp-9-5681-2009, 2009.
Ervens, B. and Volkamer, R.: Glyoxal processing by aerosol multiphase chemistry: towards a kinetic modeling framework of secondary organic aerosol formation in aqueous particles, Atmos. Chem. Phys., 10, 8219–8244, doi:10.5194/acp-10-8219-2010, 2010.
Fuchs, N. A. and Sutugin, A. G.: In Topics in Current Aerosol Research, Pergamon Press, 1971.
Gao, S., Keywood, M., Ng, N. L., Surratt, J., Varutbangkul, V., Bahreini, R., Flagan, R. C., and Seinfeld, J. H.: Low-molecular-weight and oligomeric components in secondary organic aerosol from the ozonolysis of cycloalkenes and α-Pinene, J. Phys. Chem. A, 108, 10147–10164, 2004.
George, C., Strekowski, R. S., Kleffmann, J., Stemmler, K., and Ammann, M.: Photoenhanced uptake of gaseous NO_2 on solid organic compounds: a photochemical source of HONO?, Faraday Discuss., 130, 195–210, 2005.
Greaves, T. L. and Drummond, C. J.: Protic ionic liquids: properties and applications, Chem. Rev., 108, 206–237, 2008.
Grieshop, A. P., Donahue, N. M., and Robinson, A. L.: Is the gas-particle partitioning in alpha-pinene secondary organic aerosol reversible?, Geophys. Res. Lett., 34, L14810, doi:10.1029/2007GL029987, 2007.

ACPD
14, 769–869, 2014

Griffin, R. J., Cocker III, D. R., Flagan, R. C., and Seinfeld, J. H.: Organic aerosol formation from the oxidation of biogenic hydrocarbons, J. Geophys. Res., 104, 3555–3567, 1999.

Gutzwiller, L., Arens, F., Baltensperger, U., Gäggeler, H. W., and Ammann, M.: Significance of semivolatile diesel exhaust organics for secondary HONO formation, Environ. Sci. Technol., 36, 677–682, 2002.

Hallquist, M., Wenger, J. C., Baltensperger, U., Rudich, Y., Simpson, D., Claeys, M., Dommen, J., Donahue, N. M., George, C., Goldstein, A. H., Hamilton, J. F., Herrmann, H., Hoffmann, T., Iinuma, Y., Jang, M., Jenkin, M. E., Jimenez, J. L., Kiendler-Scharr, A., Maenhaut, W., McFiggans, G., Mentel, Th. F., Monod, A., Prévôt, A. S. H., Seinfeld, J. H., Surratt, J. D., Szmigielski, R., and Wildt, J.: The formation, properties and impact of secondary organic aerosol: current and emerging issues, Atmos. Chem. Phys., 9, 5155–5236, doi:10.5194/acp-9-5155-2009, 2009.

Hansen, H. K., Rasmussen, P., Fredenslund, A., Schiller, M., and Gmehling, J.: Vapour–liquid equilibria by UNIFAC group contribution, 5. Revision and extension, Ind. Eng. Chem. Res., 30, 2352–2355, 1991.

Hildebrandt, L., Donahue, N. M., and Pandis, S. N.: High formation of secondary organic aerosol from the photo-oxidation of toluene, Atmos. Chem. Phys., 9, 2973–2986, doi:10.5194/acp-9-2973-2009, 2009.

Hirschfelder, J. O., Curtiss, C. F., and Bird, R. B.: Molecular Theory of Gases and Liquids, John Wiley, New York, 1954.

Hoffmann, T., Odum, J. R., Bowman, F., Collins, D., Klockow, D., Flagan, R. C., and Seinfeld, J. H.: Formation of organic aerosols from the oxidation of biogenic hydrocarbons, J. Atmos. Chem., 26, 189–222, 1997.

Hu, D., Tolocka, M., Li, Q., and Kamens, R. M.: A kinetic mechanism for predicting secondary organic aerosol formation from toluene oxidation in the presence of NOx and natural sunlight, Atmos. Environ., 41, 6478–6496, 2007.

Huff Hartz, K. E. H., Weitkamp, E. A., Sage, A. M., Donahue, N. M., and Robinson, A. L.: Laboratory measurements of the oxidation kinetics of organic aerosol mixtures using a relative rate constants approach, J. Geophys. Res.-Atmos., 112, D04204, doi:10.1029/2006jd007526, 2007.

Hyder, M., Genberg, J., and Jönsson, J. Å.: Application of hollow fiber liquid phase microextraction for pinic acid and pinonic acid analysis from organic aerosols, Anal. Chim. Acta, 713, 79–85, 2012.

ACPD
14, 769–869, 2014

Iinuma, Y., Böge, O., Gnauk, T., and Herrmann, H.: Aerosolchamber study of the α-pinene/O_3 reaction: Influence of particle acidity on aerosol yields and products, Atmos. Environ., 38, 761–773, 2004.

Jacobson, M. Z.: Fundamentals of Atmospheric Modelling, 2nd edn., Cambridge University Press, Cambridge, UK and New York, NY, USA, ISBN: 0-521-54865-9, 2005.

Jenkin, M. E., Saunders, S. M, and Pilling, M. J.: The tropospheric degradation of volatile organic compounds: a protocol for mechanism development, Atmos. Environ., 31, 81–104, 1997.

Jenkin, M. E., Saunders, S. M., Wagner, V., and Pilling, M. J.: Protocol for the development of the Master Chemical Mechanism, MCM v3 (Part B): tropospheric degradation of aromatic volatile organic compounds, Atmos. Chem. Phys., 3, 181–193, doi:10.5194/acp-3-181-2003, 2003.

Jimenez, J. L., Canagaratna, M. R., Donahue, N. M., Prevot, A. S. H., Zhang, Q., Kroll, J. H., DeCarlo, P. F., Allan, J. D., Coe, H., Ng, N. L., Aiken, A. C., Docherty, K. S., Ulbrich, I. M., Grieshop, A. P., Robinson, A. L., Duplissy, J., Smith, J. D., Wilson, K. R., Lanz, V. A., Hueglin, C., Sun, Y. L., Tian, J., Laaksonen, A., Raatikainen, T., Rautiainen, J., Vaattovaara, P., Ehn, M., Kulmala, M., Tomlinson, J. M., Collins, D. R., Cubison, M. J., Dunlea, E. J., Huffman, J. A., Onasch, T. B., Alfarra, M. R., Williams, P. I., Bower, K., Kondo, Y., Schneider, J., Drewnick, F., Borrmann, S., Weimer, S., Demerjian, K., Salcedo, D., Cottrell, L., Griffin, R., Takami, A., Miyoshi, T., Hatakeyama, S., Shimono, A., Sun, J. Y, Zhang, Y. M., Dzepina, K., Kimmel, J. R., Sueper, D., Jayne, J. T., Herndon, S. C., Trimborn, A. M., Williams, L. R., Wood, E. C., Middlebrook, A. M., Kolb, C. E., Baltensperger, U., and Worsnop, D. R.: Evolution of organic aerosols in the atmosphere, Science, 326, 1525–1529, 2009.

Johnson, D., Jenkin, M. E., Wirtz, K., Martin-Reviejo, M.: Simulating the formation of secondary organic aerosol from the photooxidation of aromatic hydrocarbons, Environ. Chem., 2, 35–48, 2005.

Johnson, D., Utembe, S. R., and Jenkin, M. E.: Simulating the detailed chemical composition of secondary organic aerosol formed on a regional scale during the TORCH 2003 campaign in the southern UK, Atmos. Chem. Phys., 6, 419–431, doi:10.5194/acp-6-419-2006, 2006.

Jonsson, Å. M., Hallquist, M., and Ljungström, E.: The effect of temperature and water on secondary organic aerosol formation from ozonolysis of limonene, Δ^3-carene and α-pinene, Atmos. Chem. Phys., 8, 6541–6549, doi:10.5194/acp-8-6541-2008, 2008.

ACPD
14, 769–869, 2014

Kalberer, M., Paulsen, D., Sax, M., Steinbacher, M., Dommen, J., Prévôt, A. S. H., Fisseha, R., Weingartner, E., Frankevich, V., Zenobi, R., and Baltensperger, U.: Identification of polymers as major components of atmospheric organic aerosols, Science, 303, 1659–1662, 2004.

Knopf, D. A., Anthony, L. M., and Bertram, A. K.: Reactive uptake of O_3 by multicomponent and multiphase mixtures containing oleic acid, J. Phys. Chem. A, 109, 5579–5589, 2005.

Koop, T., Bookhold, J., Shiraiwa, M., and Pöschl, U.: Glass transition and phase state of organic compounds: dependency on molecular properties and implications for secondary organic aerosols in the atmosphere, Phys. Chem. Chem. Phys., 13, 19238–19255, 2011.

Williams, I. P.: The velocity of meteoroids: a historical review, Atmos. Chem. Phys., 4, 471–475, doi:10.5194/acp-4-471-2004, 2004.

Kroll, J. and Seinfeld, J. H.: Chemistry of secondary organic aerosol: formation and evolution of low-volatility organics in the atmosphere, Atmos. Environ., 42, 3593–3624, 2008.

Kuwata, M. and Martin, S., T.: Phase of atmospheric secondary organic material affects its reactivity, P. Natl. Acad. Sci. USA, 109, 17354–17359, doi:/10.1073/pnas.1209071109, 2012.

Lai, A. and Nazaroff, W. W.: Modelling indoor particle deposition from turbulent flow onto smooth surfaces, J. Aerosol Sci., 31, 463–476, 2000.

Li, Q., Hu, D., Leungsakul, S., and Kamens, R. M.: Large outdoor chamber experiments and computer simulations: (I) Secondary organic aerosol formation from the oxidation of a mixture of *d*-limonene and *α*-pinene, Atmos. Environ., 41, 9341–9352, 2007.

Lide, D. R. (Ed.): CRC Handbook of Chemistry and Physics, 88th edn., Taylor and Francis Group, Boca Raton, FL, USA, 2008.

Liggio, J. and Li, S.-M.: Organosulfate formation during the uptake of pinonaldehyde in acidic sulphate aerosols, Geophys. Res. Lett., 33, L13808, doi:10.1029/2006GL026079, 2006.

Loza, C. L., Chhabra, P. S., Yee, L. D., Craven, J. S., Flagan, R. C., and Seinfeld, J. H.: Chemical aging of *m*-xylene secondary organic aerosol: laboratory chamber study, Atmos. Chem. Phys., 12, 151–167, doi:10.5194/acp-12-151-2012, 2012.

Maksymiuk, C. S., Gayahtri, C., Gil, R. R., and Donahue, N. M.: Secondary organic aerosol formation from multiphase oxidation of limonene by ozone: mechanistic constraints via two-dimensional heteronuclear NMR spectroscopy, Phys. Chem. Chem. Phys., 2009, 11, 7810–7818, 2009.

Marcolli, C. and Peter, Th.: Water activity in polyol/water systems: new UNIFAC parameterization, Atmos. Chem. Phys., 5, 1545–1555, doi:10.5194/acp-5-1545-2005, 2005.

ACPD
14, 769–869, 2014

Matsunaga, A. and Ziemann, P. J.: Gas-wall partitioning of organic compounds in a Teflon film chamber and potential effects on reaction product and aerosol yield measurements, Aerosol Sci. Tech., 44, 881–892, 2010.

McFiggans, G., Topping, D. O., and Barley, M. H.: The sensitivity of secondary organic aerosol component partitioning to the predictions of component properties – Part 1: A systematic evaluation of some available estimation techniques, Atmos. Chem. Phys., 10, 10255–10272, doi:10.5194/acp-10-10255-2010, 2010.

McMurry, P. H. and Rader, D. J.: Aerosol wall losses in electrically charged chambers, Aerosol Sci. Tech., 4, 249–268, 1985.

Metzger, A., Dommen, J., Gaeggeler, K., Duplissy, J., Prevot, A. S. H., Kleffmann, J., Elshorbany, Y., Wisthaler, A., and Baltensperger, U.: Evaluation of 1,3,5 trimethylbenzene degradation in the detailed tropospheric chemistry mechanism, MCMv3.1, using environmental chamber data, Atmos. Chem. Phys., 8, 6453–6468, doi:10.5194/acp-8-6453-2008, 2008.

Na, K., Song, C., Switzer, C., and Cocker, D.: Effect of ammonia on secondary organic aerosol formation from α-pinene ozonolysis in dry and humid conditions, Environ. Sci. Technol., 41, 6096–6102, 2007.

Nannoolal, J., Rarey, J., and Ramjugernath, D.: Estimation of pure component properties Part 3. Estimation of the vapour pressure of non-electrolyte organic compounds via group contributions and group interactions, Fuild Phase Equilibria, 269, 117–133, 2008.

Nash, D. G., Tolocka, M. P., and Baer, T.: The uptake of O_3 by myristic acid-oleic acid mixed particles: evidence for solid surface layers, Phys. Chem. Chem. Phys., 8, 4468–4475, doi:10.1039/b609855j, 2006.

Ng, N. L., Kroll, J. H., Chan, A. W. H., Chhabra, P. S., Flagan, R. C., and Seinfeld, J. H.: Secondary organic aerosol formation from *m*-xylene, toluene, and benzene, Atmos. Chem. Phys., 7, 3909–3922, doi:10.5194/acp-7-3909-2007, 2007.

Ng, N. L., Kwan, A. J., Surratt, J. D., Chan, A. W. H., Chhabra, P. S., Sorooshian, A., Pye, H. O. T., Crounse, J. D., Wennberg, P. O., Flagan, R. C., and Seinfeld, J. H.: Secondary organic aerosol (SOA) formation from reaction of isoprene with nitrate radicals (NO_3), Atmos. Chem. Phys., 8, 4117–4140, doi:10.5194/acp-8-4117-2008, 2008.

Nordin, E. Z., Eriksson, A. C., Roldin, P., Nilsson, P. T., Carlsson, J. E., Kajos, M. K., Hellén, H., Wittbom, C., Rissler, J., Löndahl, J., Swietlicki, E., Svenningsson, B., Bohgard, M., Kulmala, M., Hallquist, M., and Pagels, J. H.: Secondary organic aerosol formation from idling

ACPD
14, 769–869, 2014

gasoline passenger vehicle emissions investigated in a smog chamber, Atmos. Chem. Phys., 13, 6101–6116, doi:10.5194/acp-13-6101-2013, 2013.
Odum, J. R., Hoffmann, T., Bowman, F., Collins, D., Flagan, R. C., and Seinfeld, J. H.: Gas/particle partitioning and secondary organic aerosol yields, Environ. Sci. Technol., 30, 2580–2585, 1996.
Pankow, J. F.: An absorption-model of the gas aerosol partitioning involved in the formation of secondary organic aerosol, Atmos. Environ., 28, 189–193, 1994.
Pankow, J. F. and Asher, W. E.: SIMPOL.1: a simple group contribution method for predicting vapor pressures and enthalpies of vaporization of multifunctional organic compounds, Atmos. Chem. Phys., 8, 2773–2796, doi:10.5194/acp-8-2773-2008, 2008.
Pathak, R. K., Presto, A. A., Lane, T. E., Stanier, C. O., Donahue, N. M., and Pandis, S. N.: Ozonolysis of α-pinene: parameterization of secondary organic aerosol mass fraction, Atmos. Chem. Phys., 7, 3811–3821, doi:10.5194/acp-7-3811-2007, 2007.
Paulsen, D., Dommen, J., Kalberer, M., Prevot, A. S. H., Richter, R., Sax, M., Steinbacher, M., Weingartner, E., and Baltensperger, U.: Secondary organic aerosol formation by irradiation of 1,3,5-trimethylbenzene-NO_x-H_2O in a new reaction chamber for atmospheric chemestry and physics, Environ. Sci. Technol., 39, 2668–2678, 2005.
Pfrang, C., Shiraiwa, M., and Pöschl, U.: Chemical ageing and transformation of diffusivity in semi-solid multi-component organic aerosol particles, Atmos. Chem. Phys., 11, 7343–7354, doi:10.5194/acp-11-7343-2011, 2011.
Pierce, J. R., Engelhart, G. J., Hildebrandt, L., Weitkamp, E. A., Pathak, R. K., Donahue, N. M., Robinson, A. L., Adams, P. J., and Pandis, S. N.: Constraining particle evolution from wall losses, coagulation, and condensation-evaporation in smog-chamber experiments: optimal estimation based on size distribution measurements, Aerosol Sci. Tech., 42, 1001–1015, 2008.
Pun, B. K. and Seigneur, C.: Investigative modeling of new pathways for secondary organic aerosol formation, Atmos. Chem. Phys., 7, 2199–2216, doi:10.5194/acp-7-2199-2007, 2007.
Pöschl, U., Rudich, Y., and Ammann, M.: Kinetic model framework for aerosol and cloud surface chemistry and gas-particle interactions – Part 1: General equations, parameters, and terminology, Atmos. Chem. Phys., 7, 5989–6023, doi:10.5194/acp-7-5989-2007, 2007.
Pöschl, U.: Gas–particle interactions of tropospheric aerosols: Kinetic and thermodynamic perspectives of multiphase chemical reactions, amorphous organic substances, and the activation of cloud condensation nuclei, Atmos. Res., 101, 562–573, 2011.

ACPD
14, 769–869, 2014

Rader, D. J., McMurry, P. H., and Smith, S.: Evaporation Rates of Monodisperse Organic Aerosols in the 0.02- to 0.2-µm-Diameter Range, Aerosol Sci. Tech., 6, 247–260, 1987.
Ray, A. K., Davis, E. J., and Ravindran, P.: Determination of ultralow vapour-pressures by submicron droplet evaporation, J. Chem. Phys., 71, 582–587, 1979.
Ray, A. K, Lee, J., and Tilley, H. L.: Direct measurements of evaporation rates of single droplets at large knudsen numbers, Langmuir, 4, 631–637, 1988.
Rickard, A. R., Wyche, K. P., Metzger, A., Monks, P. S., Ellis, A. M., Dommenc, J., Baltensperger, U., Jenkin, M. E., and Pilling, M. J.: Gas phase precursors to anthropogenic secondary organic aerosol: Using the Master Chemical Mechanism to probe detailed observations of 1,3,5-trimethylbenzene photo-oxidation, Atmos. Environ., 44, 5423–5433, 2010.
Riipinen, I., Pierce, J. R., Donahue, N. M., and Pandis, S. N.: Equilibration time scales of organic aerosol inside thermodenuders: Evaporation kinetics versus thermodynamics, Atmos. Environ., 44, 597–607, 2010.
Rohrer, F., Bohn, B., Brauers, T., Brüning, D., Johnen, F.-J., Wahner, A., and Kleffmann, J.: Characterisation of the photolytic HONO-source in the atmosphere simulation chamber SAPHIR, Atmos. Chem. Phys., 5, 2189–2201, doi:10.5194/acp-5-2189-2005, 2005.
Roldin, P., Swietlicki, E., Schurgers, G., Arneth, A., Lehtinen, K. E. J., Boy, M., and Kulmala, M.: Development and evaluation of the aerosol dynamics and gas phase chemistry model ADCHEM, Atmos. Chem. Phys., 11, 5867–5896, doi:10.5194/acp-11-5867-2011, 2011a.
Roldin, P., Swietlicki, E., Massling, A., Kristensson, A., Löndahl, J., Eriksson, A., Pagels, J., and Gustafsson, S.: Aerosol ageing in an urban plume – implication for climate, Atmos. Chem. Phys., 11, 5897–5915, doi:10.5194/acp-11-5897-2011, 2011b.
Rudich, Y., Donahue, N. M., and Mentel, T. F.: Aging of organic aerosol: Bridging the gap between laboratory and field studies, Annu. Rev. Phys. Chem., 58, 321–352, 2007.
Saukko, E., Lambe, A. T., Massoli, P., Koop, T., Wright, J. P., Croasdale, D. R., Pedernera, D. A., Onasch, T. B., Laaksonen, A., Davidovits, P., Worsnop, D. R., and Virtanen, A.: Humidity-dependent phase state of SOA particles from biogenic and anthropogenic precursors, Atmos. Chem. Phys., 12, 7517–7529, doi:10.5194/acp-12-7517-2012, 2012.
Saunders, S. M., Jenkin, M. E., Derwent, R. G., and Pilling, M. J.: Protocol for the development of the Master Chemical Mechanism, MCM v3 (Part A): tropospheric degradation of non-aromatic volatile organic compounds, Atmos. Chem. Phys., 3, 161–180, doi:10.5194/acp-3-161-2003, 2003.

ACPD
14, 769–869, 2014

Seinfeld, J. H. and Pandis, S. N.: Atmosphere Chemistry Physics: From Air Pollution to Climate Change, 2nd edn., Wiley, New Jersey, ISBN: 0-471-72018-6, 2006.
Shiraiwa, M., Pfrang, C., and Pöschl, U.: Kinetic multi-layer model of aerosol surface and bulk chemistry (KM-SUB): the influence of interfacial transport and bulk diffusion on the oxidation of oleic acid by ozone, Atmos. Chem. Phys., 10, 3673–3691, doi:10.5194/acp-10-3673-2010, 2010.
Shiraiwa, M., Ammann, M., Koop, T., and Pöschl, U.: Gas uptake and chemical aging of semisolid organic aerosol particles, P. Natl. Acad. Sci. USA, 108, 11003–11008, doi:10.1073/pnas.1103045108, 2011.
Shiraiwa, M., Pfrang, C., Koop, T., and Pöschl, U.: Kinetic multi-layer model of gas-particle interactions in aerosols and clouds (KM-GAP): linking condensation, evaporation and chemical reactions of organics, oxidants and water, Atmos. Chem. Phys., 12, 2777–2794, doi:10.5194/acp-12-2777-2012, 2012.
Smith, J. N., Dunn, M. J., VanReken, T. M., Iida, K., Stolzenburg, M. R., McMurry, P. H., and Huey, L. G.: Chemical composition of atmospheric nanoparticles formed from nucleation in Tecamac, Mexico: Evidence for an important role for organic species in nanoparticle growth, Geophys. Res. Lett., 35, L04808, doi:10.1029/2007gl032523, 2008.
Smith, J. N., Barsanti, K. C, Friedli, H. R., Ehn, M., Kulmala, M., Collins, D. R., Scheckman, J. H., Williams, B. J., and McMurry, P. H.: Observations of aminium salts in atmospheric nanoparticles and possible climatic implications, P.. Natl. Acad. Sci. USA, 107, 6634–6639, 2010.
Smith, M. L., Kuwata, M., and Martin, S. T.: Secondary organic material produced by the dark ozonolysis of α-pinene minimally affects the deliquescence and efflorescence of ammonium sulphate, Aerosol Sci. Tech., 45, 244–261, doi:10.1080/02786826.2010.532178, 2011.
Stroeve, P.: On the diffusion of gases in protein solutions, Ind. Eng. Chem. Fund., 14, 140–141, 1975.
Surratt, J. D., Kroll, J. H., Kleindienst, T. E., Edney, E. O., Claeys, M., Sorooshian, A., Ng, N. L., Offenberg, J. H., Lewandowski, M., Jaoui, M., Flagan, R. C., and Seinfeld, J. H.: Evidence for organosulfates in secondary organic aerosol, Environ. Sci. Technol., 41, 517–527, 2007.
Svenningsson, B., Rissler, J., Swietlicki, E., Mircea, M., Bilde, M., Facchini, M. C., Decesari, S., Fuzzi, S., Zhou, J., Mønster, J., and Rosenørn, T.: Hygroscopic growth and critical supersaturations for mixed aerosol particles of inorganic and organic compounds of atmospheric relevance, Atmos. Chem. Phys., 6, 1937–1952, doi:10.5194/acp-6-1937-2006, 2006.

ACPD
14, 769–869, 2014

Tolocka, M. P., Jang, M., Ginter, J. M., Cox, F. J., Kamens, R. M., and Johnston, M. V.: Formation of oligomers in secondary organic aerosol, Environ. Sci. Technol., 38, 1428–1434, 2004.
Vaden, T. D., Song, C., Zaveri, R. A., Imre, D., and Zelenyuk, A.: Morphology of mixed primary and secondary organic particles and the adsorption of spectator organic gases during aerosol formation, Proc. Natl. Acad. Sci., 107, 6658–6663, 2010.
Vaden, T. D., Imreb, D., Beráneka, J., Shrivastavaa, M., and Zelenyuka, A.: Evaporation kinetics and phase of laboratory and ambient secondary organic aerosol, P. Natl. Acad. Sci. USA, 108, 2190–2195, 2011.
Valorso, R., Aumont, B., Camredon, M., Raventos-Duran, T., Mouchel-Vallon, C., Ng, N. L., Seinfeld, J. H., Lee-Taylor, J., and Madronich, S.: Explicit modelling of SOA formation from α-pinene photooxidation: sensitivity to vapour pressure estimation, Atmos. Chem. Phys., 11, 6895–6910, doi:10.5194/acp-11-6895-2011, 2011.
Vesterinen, M., Lehtinen, K. E. J., Kulmala, M., and Laaksonen, A.: Effect of particle phase oligomer formation on aerosol growth, Atmos. Environ., 41, 1768–1776, 2007.
Virtanen, A., Joutsensaari, J., Koop, T., Yli-Pirilä, P., Leskinen, J., Mäkelä, J. M., Holopainen, J. K., Pöschl, U., Kulmala, M., Worsnop, D. R., and Laaksonen, A.: An amorphous solid state of biogenic secondary organic aerosol particles, Nature, 467, 824–827, 2010.
Widmann, J, Heusmann, C. M., and Davis, E. J.: The effect of a polymeric additive on the evaporation of organic aerocolloidal droplets, Colloid Polym. Sci., 276, 197–205, 1998.
Wiedensohler, A., Birmili, W., Nowak, A., Sonntag, A., Weinhold, K., Merkel, M., Wehner, B., Tuch, T., Pfeifer, S., Fiebig, M., Fjäraa, A. M., Asmi, E., Sellegri, K., Depuy, R., Venzac, H., Villani, P., Laj, P., Aalto, P., Ogren, J. A., Swietlicki, E., Williams, P., Roldin, P., Quincey, P., Hüglin, C., Fierz-Schmidhauser, R., Gysel, M., Weingartner, E., Riccobono, F., Santos, S., Grüning, C., Faloon, K., Beddows, D., Harrison, R., Monahan, C., Jennings, S. G., O'Dowd, C. D., Marinoni, A., Horn, H.-G., Keck, L., Jiang, J., Scheckman, J., McMurry, P. H., Deng, Z., Zhao, C. S., Moerman, M., Henzing, B., de Leeuw, G., Löschau, G., and Bastian, S.: Mobility particle size spectrometers: harmonization of technical standards and data structure to facilitate high quality long-term observations of atmospheric particle number size distributions, Atmos. Meas. Tech., 5, 657–685, doi:10.5194/amt-5-657-2012, 2012.
Yli-Juuti, T., Barsanti, K., Hildebrandt Ruiz, L., Kieloaho, A.-J., Makkonen, U., Petäjä, T., Ruuskanen, T., Kulmala, M., and Riipinen, I.: Model for acid-base chemistry in nanoparti-

ACPD
14, 769–869, 2014

cle growth (MABNAG), Atmos. Chem. Phys., 13, 12507–12524, doi:10.5194/acp-13-12507-2013, 2013.

Zelenyuk, A., Yang, J., Song, C., Zaveri, R. A., and Imre, D.: A new real-time method for determining particles' sphericity and density: application to secondary organic aerosol formed by ozonolysis of α-pinene, Environ. Sci. Technol., 42, 8033–8038, 2008.

Zelenyuk, A., Imre, D., Beránek, J., Abramson, E., Wilson, J., and Shrivastava, M.: Synergy between secondary organic aerosols and long-range transport of polycyclic aromatic hydrocarbons, Environ. Sci. Technol., 46, 12459–12466, 2012.

Zhang, S.-H., Seifeld, J. H., and Flagan, R. C.: Determination of Particle Vapour Pressures Using the Tandem Differential Mobility Analyzer, Aerosol Sci. Tech., 19, 3–14, 1993.

Zobrist, B., Soonsin, V., Luo, B. P., Krieger, U. K., Marcolli, C., Peter, T., and Koop, T.: Ultra-slow water diffusion in aqueous sucrose glasses, Phys. Chem. Chem. Phys., 13, 3514–3526, doi:10.1039/c0cp01273d, 2011.

Zuend, A., Marcolli, C., Luo, B. P., and Peter, T.: A thermodynamic model of mixed organic-inorganic aerosols to predict activity coefficients, Atmos. Chem. Phys., 8, 4559–4593, doi:10.5194/acp-8-4559-2008, 2008.

Zuend, A., Marcolli, C., Peter, T., and Seinfeld, J. H.: Computation of liquid-liquid equilibria and phase stabilities: implications for RH-dependent gas/particle partitioning of organic-inorganic aerosols, Atmos. Chem. Phys., 10, 7795–7820, doi:10.5194/acp-10-7795-2010, 2010.

Zuend, A., Marcolli, C., Booth, A. M., Lienhard, D. M., Soonsin, V., Krieger, U. K., Topping, D. O., McFiggans, G., Peter, T., and Seinfeld, J. H.: New and extended parameterization of the thermodynamic model AIOMFAC: calculation of activity coefficients for organic-inorganic mixtures containing carboxyl, hydroxyl, carbonyl, ether, ester, alkenyl, alkyl, and aromatic functional groups, Atmos. Chem. Phys., 11, 9155–9206, doi:10.5194/acp-11-9155-2011, 2011.

Zuend, A. and Seinfeld, J. H.: Modeling the gas-particle partitioning of secondary organic aerosol: the importance of liquid-liquid phase separation, Atmos. Chem. Phys., 12, 3857–3882, doi:10.5194/acp-12-3857-2012, 2012.

ACPD
14, 769–869, 2014

Table 1. Model parameters used in the multilayer module for O_3 uptake, diffusion and reactions in the particle phase.

Parameter	Definition	Value
$\alpha_{s,0,O_3}$	Surface accommodation coefficient of O_3 on a free substrate	1[a]
τ_{d,O_3}	O_3 desorption lifetime	10^{-9}[a]
K_{H,O_3} (mol m^3 Pa^{-1})	Henry's law coefficient of O_3	4.7×10^{-3}[a,b]
D_{0,O_3} (cm^2 s^{-1})	Bulkdiffusion coefficient O_3 without obstruction	Variable
ω_{O_3} (cm s^{-1})	Mean thermal velocity O_3	3.6×10^4[a]
d_{O_3} (nm)	Effective diameter cross section O_3	0.4[a]
k_{O_3} (cm^3 molec^{-1} s^{-1})	Reaction rate constant between O_3 and organic comp.	Variable

[a] Values from Pfrang et al. (2011),
[b] Different unit than in Pfrang et al. (2011).

ACPD
14, 769–869, 2014

Table 2. Base case model set-up values for the simulation of organic salt formation between carboxylic acids and dissolved ammonium ions.

Parameter	Definition	Value[a]
$pK_{a,COOH}$	Logarithm of carboxylic acid dissociation constant	4.6
pK_{a,NH_3}	Logarithm of NH_4^+ dissociation constant	9.25[b]
$K_s^*(mol^2\,m^{-6})$	Effective solubility product (see Eq. 32)	0.1
K_H $(mol\,m^{-3}\,atm^{-1})$	Henry's law coefficient for NH_3	57.6[c]
$p_{0,i}$	Pure-liquid saturation vapour pressure comp. i	SIMPOL
γ_i	Activity coefficient for compound i	AIOMFAC
$D_{0,monomer,SOA}$ $(cm^2\,s^{-1})$	Diffusion coefficient for SOA monomers	5×10^{-17}[d]
$D_{0,ammonium}$ $(cm^2\,s^{-1})$	Diffusion coefficient for NH_3/NH_4^+	1.3×10^{-16}[d]
D_{NH_4RCOO} $(cm^2\,s^{-1})$	Diffusion coefficient of organic salts	0

[a] Base case simulation value.
[b] Lide (2008) (CRC Handbook of Chemistry and Physics) at 298 K.
[c] Jacobson (2005).
[d] Based on the Stoke–Einstein relationship and a SOA viscosity of 10^8 Pa s Abramson et al. (2013).

ACPD
14, 769–869, 2014

Table 3. Initial conditions and results from the α-pinene-O_3-NH_3 – CO experiments Na et al. (2007) and base case model simulations.

Date	Initial [α-pin.] exp. (ppb)	Initial NH_3 (ppb)	Δ [O_3] exp. (ppb)	Δ [α-pin.] exp.	Yield exp. (%)	Initial [α-pin.] model (ppb)	Δ [O_3] model (ppb)	Δ [α-pin.] model(ppb)	Yield model. (%)
25 Jan 05	221		130	218	**54.3**	222	149	216	**57.5**
11 Jan 05	221	50	150	203	**60.3**	222	149	216	**63.6**
10 Jan 05	223	100	150	206	**64.0**	222	149	216	**65.4**
06 Jan 05	224	200	151	220	**65.3**	222	149	216	**67.0**

ACPD
14, 769–869, 2014

Table A1. Nomenclature.

Symbol	Description
α_s	Surface mass accommodation coefficient
$\alpha_{0,s}$	Surface mass accommodation coefficient of surface free from adsorbing material
γ	Activity coefficient
$\gamma_{w,i}$	Activity coefficient of compound i in a Teflon wall film
δ_k	Width of particle layer k
h	Distance between the roof and ceiling of the chamber
Δx	Laminar layer width adjacent to chamber walls or charcoal denuder
θ_s	Relative surface coverage of the adsorbed species
μ	Dynamic viscosity of air
ρ_{air}	Density of air
ρ_p	Particle phase density
σ	Surface tension
τ_{d,O_3}	Desorption lifetime of O_3
ω_{O_3}	Mean thermal velocity of O_3
v_e	Characteristic average deposition velocity due to electrostatic forces
$\Omega_{AB}^{(1,1)}$	Collision integral between
A_k	Area of exchange between particle layer $k-1$ and k
$A_{chamber}$	Chamber surface area
c_d	Dimer particle phase concentration
c_{H^+}	Hydrogen ion concentration
c_m	Monomer particle phase concentration
$c_{m,i}$(p.s.)	Particle surface monolayer concentration of reactive monomers
c_{PINAL}(g)	Gas phase concentration of pinonaldehyde
C_c	Cunningham slip correction factor
C_k	Kelvin effect
C_∞	Gas phase concentration far from the particle surfaces
C_s	Saturation gas phase concentration at the particle surface
C_w	Effective wall equivalent mass concentration
d_{O_3}	Width of the O_3 sorption layer
d_i	Collision diameter of compound i
d_{air}	Collision diameter of compound air molecules
$d_{i,\,air}$	Collision diameter for binary collisions between compound $i$and air molecules
D_p	Particle diameter

ACPD
14, 769–869, 2014

Table A1. Nomencalature.

Symbol	Description
D_{va}	Vacuum aerodynamic diameter
D_{0,X_i}	Diffusivity coefficient of compound X_i without obstructing material
D_{X_i}	Diffusion coefficient of compound X_i
e	Elementary charge of a single proton
$\overline{E}$	Mean electrical field strength
$\overline{E_0}$	Initial mean electrical field strength
F	Fuchs-Sutugin correction factor in the transition region
f_p	Particle volume fraction of solid or semi-solid obstructing material
f_{ROOR}	Fraction of $RO_2 + RO_2$ reactions which give ROOR dimer
$F_f(p)$	Dimer formation rates in the particle phase
$F_f(p.s.)$	Dimer formation rates in the particle surface layer
I	Molar condensation growth rate
J_{ads,O_3}	Adsorption rate of O_3 to the sorption layer
J_{des,O_3}	Desorption rate of O_3 from the sorption layer
k_b	The Boltzmann constant
k_{charge}	First order deposition loss rate due to charge
k_d	Dimer specific degradation reaction rate constant
k_f	Dimer formation rate constant
$k_{k,k+1,X_i}$	Transport velocity of compound X_i between the layers k and layer $k+1$.
k_{Ox}	Oxidation reaction rate constant in the particle phase
k_{so,su,O_3}	Transport velocity of O_3 from the sorption layer to the surface layer
k_{su,so,O_3}	Transport velocity of O_3 from the surface layer to the sorption layer
$k_{g,\,w}$	First order loss rate from the near wall gas phase to the walls
$k_{w,\,g}$	Desorption rate from the chamber wall Teflon surfaces
k_w	Effective wall deposition loss rate
K_a	Acid dissociation constant
K_H	Henry's law constant
K_s	Solubility product of salt
K_s^*	Effective solubility product of organic salts
Kn	Non-dimensional Knudsen number
m_i	Molecular mass of compound i
m_{air}	Average air molecular mass

ACPD
14, 769–869, 2014

Table A1. Nomencalature.

Symbol	Description
M_i	Molar mass of compound i
M_w	Average molar mass of a Teflon wall film
N	Number of elemental charges of a particle
N_a	Avogadros's number
p	Total pressure
p_0	Pure-liquid saturation vapour pressure
p_s	Equilibrium vapour pressure
pH	Negative 10-logarithm of the hydrogen ion concentration
pK_a	Negative 10-logarithm of the acid dissociation constant
R	Universal gas constant ($8.3145\,J K^{-1}\,mol^{-1}$)
RH	Relative humidity in %
t	Time
T	Temperature in Kelvin
u^*	Friction velocity
V_k	Volume of particle layer k
$V_{chamber}$	Chamber volume
V_{wall}	Air volume of a thin layer adjacent to the chamber walls
x	mole fractions
x_k	Ratio between the smaller and larger of the two volume fluxes across A_k
X	Condensable organic compound
$[X_{i,g,w}]$	Concentrations of compound X_i in the thin layer adjacent to the chamber walls
$[X_{i,w}]$	Concentration of compound X_i at the chamber wall
Y	Organic compound formed by particle phase oxidation reaction

ACPD
14, 769–869, 2014

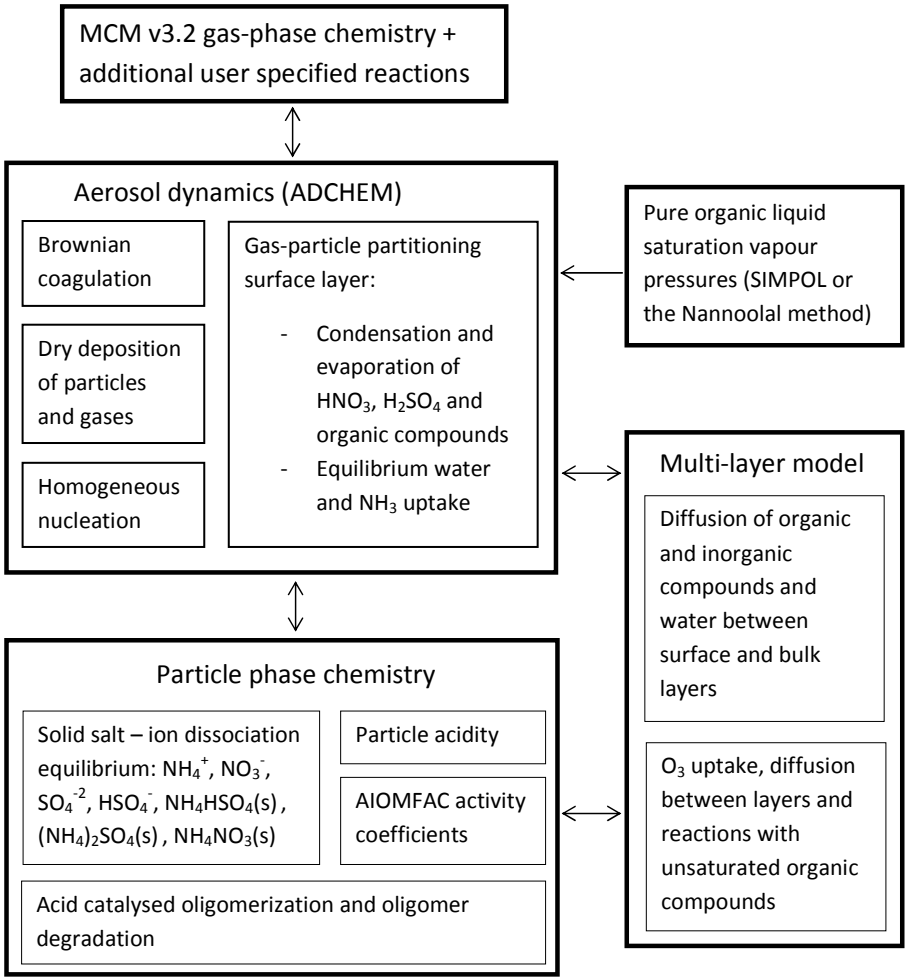

Fig. 1. Schematic picture of the ADCHAM model structure.

ACPD
14, 769–869, 2014

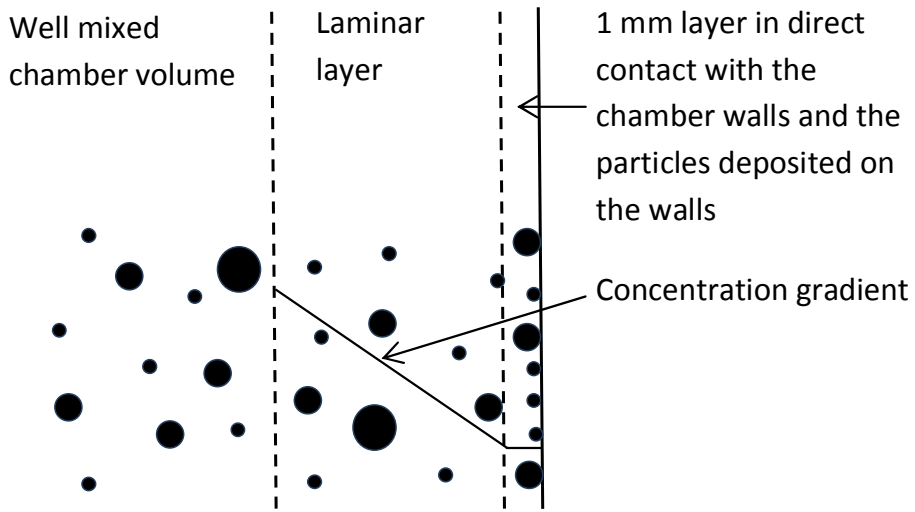

Fig. 2. Schematic figure which illustrates how ADCHAM treat the diffusion limited mass transfer of gas phase compounds across a laminar layer next to the chamber walls. The thin (1 mm thick) air layer next to the chamber walls is treated as a separate volume which exchange gas phase compounds with the well mixed chamber and the walls + wall deposited particles.

ACPD
14, 769–869, 2014

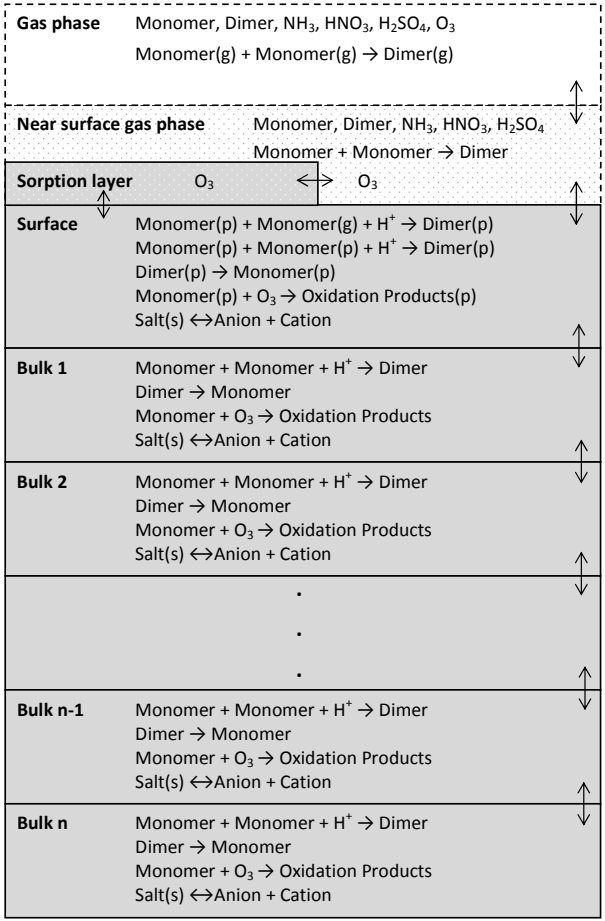

Fig. 3. Schematic picture which illustrates the model structure and processes included in the kinetic multilayer model in ADCHAM.

ACPD
14, 769–869, 2014

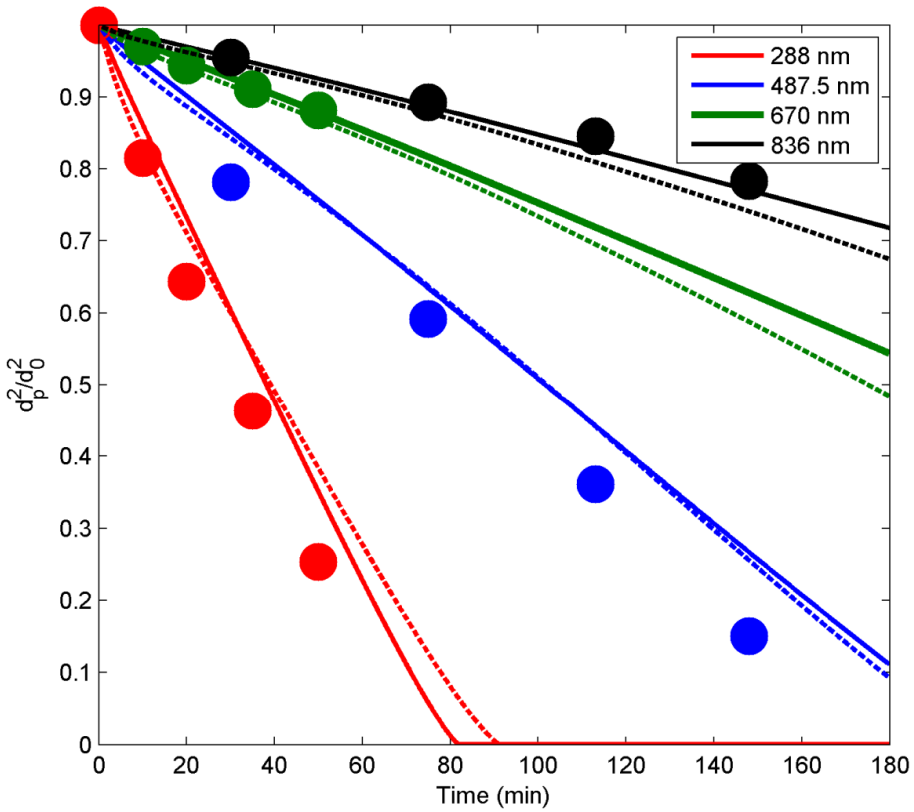

Fig. 4. Modelled and measured (Vaden et al., 2011) evaporation losses of DOP particles of different initial diameters. The model results are from simulations with (1) Eq. (30) and a laminar layer width of 0.1 cm adjacent to the charcoal denuder (solid lines), and (2) Eq. (31) and a laminar layer of 0.6 cm (dashed lines). The measurements are given by the solid circles. The DOP mass accommodation coefficient was assumed one.

ACPD
14, 769–869, 2014

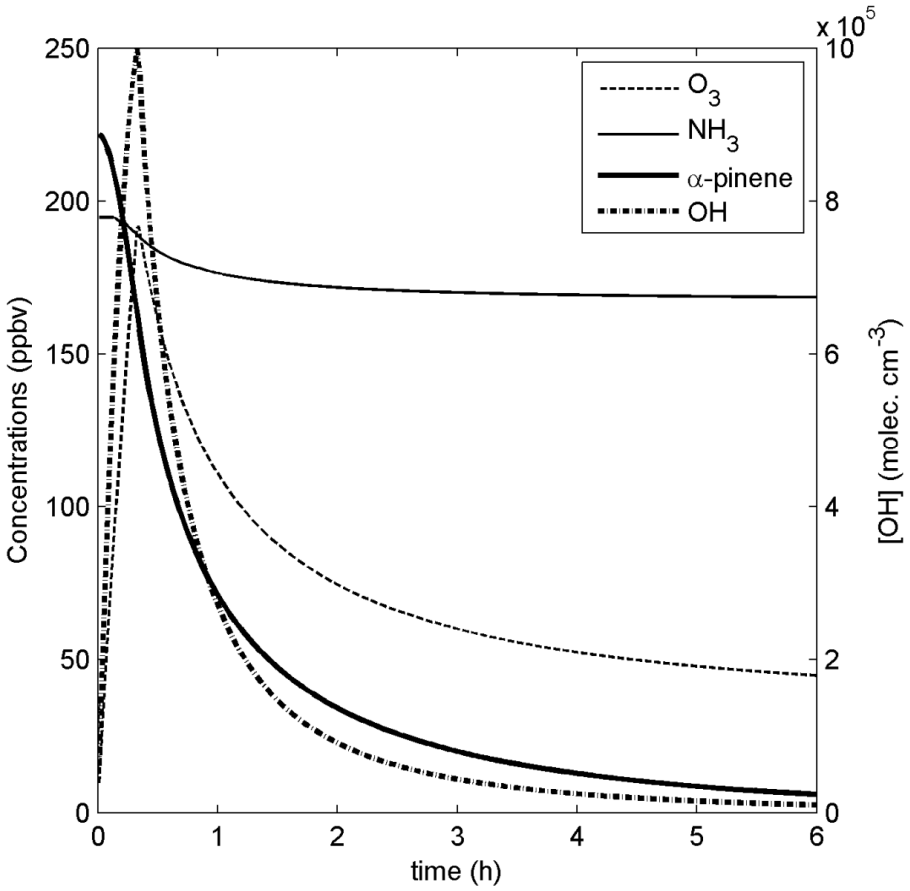

Fig. 5. Modelled NH_3(g), O_3(g), α-pinene(g) and OH(g) concentrations for the α-pinene oxidation experiments by Na et al. (2007).

ACPD
14, 769–869, 2014

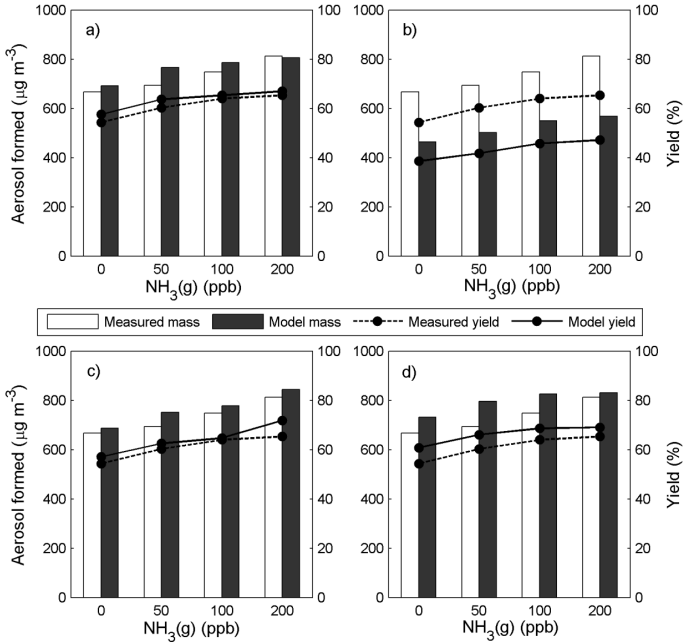

Fig. 6. Comparison of modelled and measured SOA mass and mass yields at different initial levels of NH_3(g). In **(a)** the model results are from simulations with vapour pressures from SIMPOL, activity coefficients from AIOMFAC and very slow mixing between the particle layers (base case), in **(b)** the results are from simulations with vapour pressures from Nannoolal et al. (2008), activity coefficients from AIOMFAC and very slow mixing between particle layers, in **(c)** the results are from simulations with vapour pressures from SIMPOL, unity activity coefficients (ideal solution) and very slow mixing between the particle layers, and in Fig. **(d)** the model results are from simulations with vapour pressures from SIMPOL, activity coefficients from AIOMFAC and semi-solid less viscous particles with $D_{0,\mathrm{monomer,SOA}} = 10^{-15}\,\mathrm{cm^2\,s^{-1}}$, $D_{0,\mathrm{ammonium}} = 10^{-13}\,\mathrm{cm^2\,s^{-1}}$ and $D_{0,\mathrm{NH_4RCOO}} = 0\,\mathrm{cm^2\,s^{-1}}$.

ACPD
14, 769–869, 2014

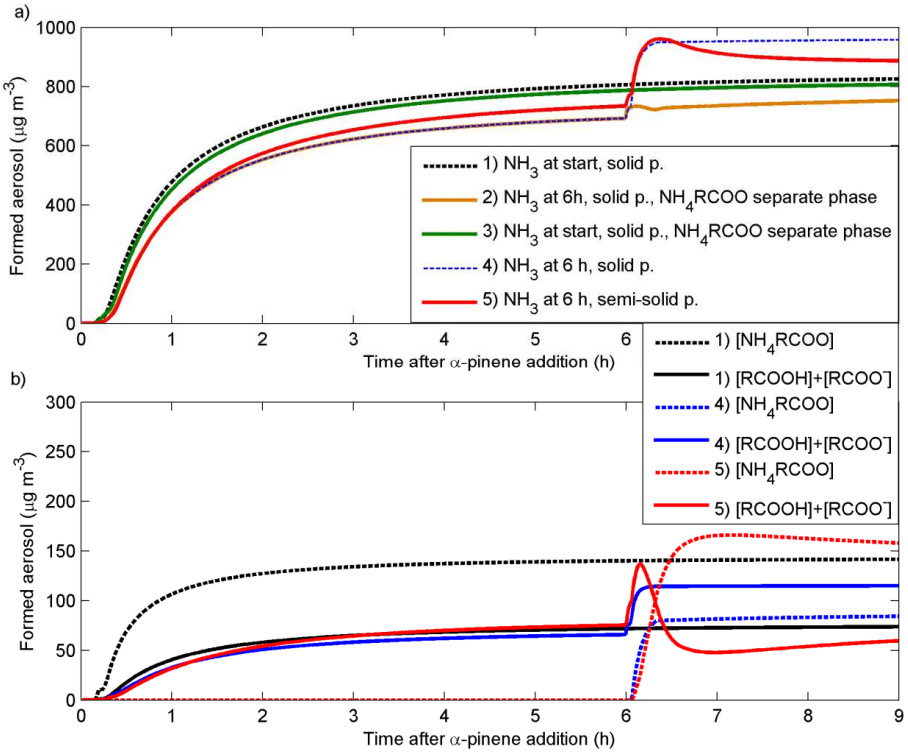

Fig. 7. Modelled SOA mass formation for α-pinene-O_3-NH_3 – CO experiments with 200 ppb NH_3 added at the start or after 6 h of aging. For all simulations SIMPOL was used to estimate the vapour pressures of the organic compounds. The SOA particles were either treated as completely solid (no mixing between particle layers) (simulation 1–4) or semi-solid with $D_{0,\mathrm{monomer,SOA}} = 10^{-15}\,\mathrm{cm^2\,s^{-1}}$, $D_{0,\mathrm{ammonium}} = 10^{-13}\,\mathrm{cm^2\,s^{-1}}$ and $D_{0,\mathrm{NH_4RCOO}} = 0\,\mathrm{cm^2\,s^{-1}}$ (simulation 5). For simulation 2 and 3 we assume that the NH_4RCOO salts form a separate phase which other organic compounds cannot dissolved into.

ACPD
14, 769–869, 2014

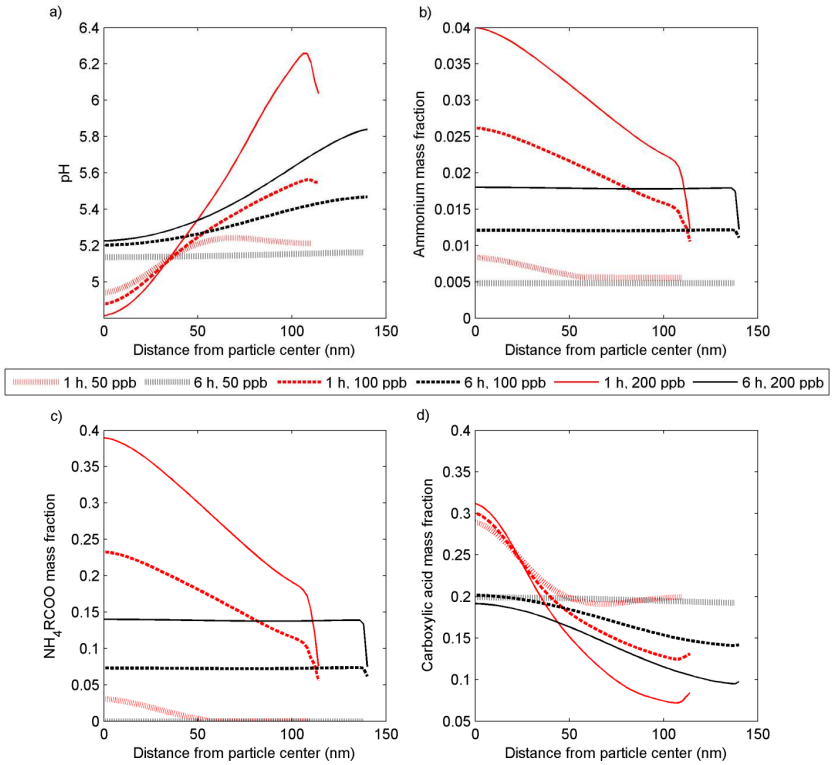

Fig. 8. Modelled **(a)** pH, **(b)** ammonium ($NH_4^+ + NH_3(l) + NH_4$ in NH_4RCOO) mass fractions, **(c)** NH_4RCOO mass fractions and **(d)** carboxylic acid ($COOH + COO^-$) mass fractions at different distances from the particle core, for α-pinene SOA particles with a diameter of approximately 240 nm after 1 h and 280 nm after 6 h of aging. The model results are from three different simulations with an initial [NH_3(g)] of 50, 100 or 200 ppb. The SOA particles were assumed to be semi-solid with $D_{0,\text{monomer,SOA}} = 10^{-15}\,\text{cm}^2\,\text{s}^{-1}$, $D_{0,\text{ammonium}} = 10^{-13}\,\text{cm}^2\,\text{s}^{-1}$ and $D_{0,NH_4RCOO} = 0\,\text{cm}^2\,\text{s}^{-1}$.

ACPD
14, 769–869, 2014

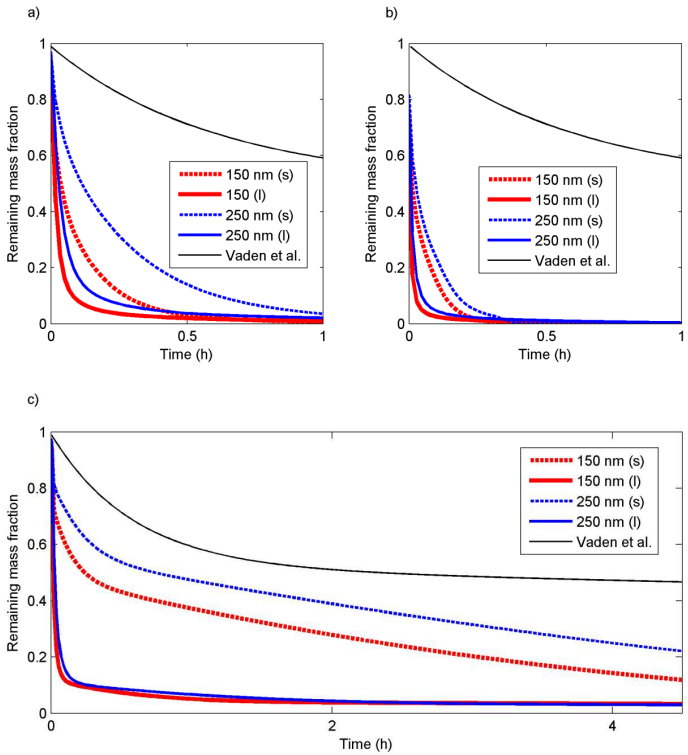

Fig. 9. Modelled and measured (Vaden et al., 2011) evaporation rates of fresh α-pinene SOA particles. **(a)** Model results for SOA particles with volatility according to the VBS parameterization from Pathak et al. (2007). **(b)** Model results are from simulations using vapour pressures of the MCMv3.2 compounds were estimated with SIMPOL. **(c)** Model results using vapour pressures estimated with the Nannoolal method. The evaporation loss rates are given for particles with a diameter of ~ 150 and ~ 250 nm, treated as liquid (l) or solid (s) (no diffusion between the particle layers).

ACPD
14, 769–869, 2014

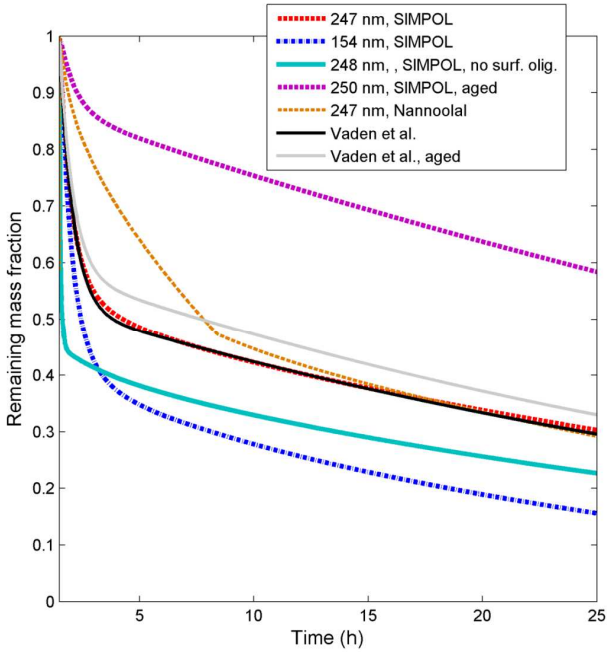

Fig. 10. Modelled and measured (Vaden et al., 2011) evaporation of α-pinene SOA particles. For the model simulations we considered three different bulk phase oligomerization mechanisms: peroxyhemiacetal formation (R1a), hemiacetal formation (R3) and ester formation (R4) ($k_f = 1.2 \times 10^{-27}$ cm^3 molecules^{-1} and $k_d = 1/3.2$ h^{-1}). We also considered surface layer oligomers formed by the reactive uptake of adsorbed pinonaldehyde (Reactions R1b and R2b and Eq. 33) ($k_f = 3 \times 10^{-15}$ cm^3 molecules^{-1} $k_d = 3/2$ h^{-1}). SOA was treated as semi-solid and the oligomer SOA as solid non mixing material ($D_{0,\text{monomer}} = 5 \times 10^{-17}$ cm^2 s^{-1}, $D_{0,\text{dimer}} = 0$ cm^2 s^{-1}). The figure shows the modelled remaining particle mass fraction for particles with an initial diameter of 154 or $\sim$ 250 nm, respectively. The results are from simulations with the SIMPOL or Nannoolal vapour pressure method, fresh or aged SOA particles, and with or without surface-layer oligomer formation by the reactive uptake of adsorbed pinonaldehyde.

ACPD
14, 769–869, 2014

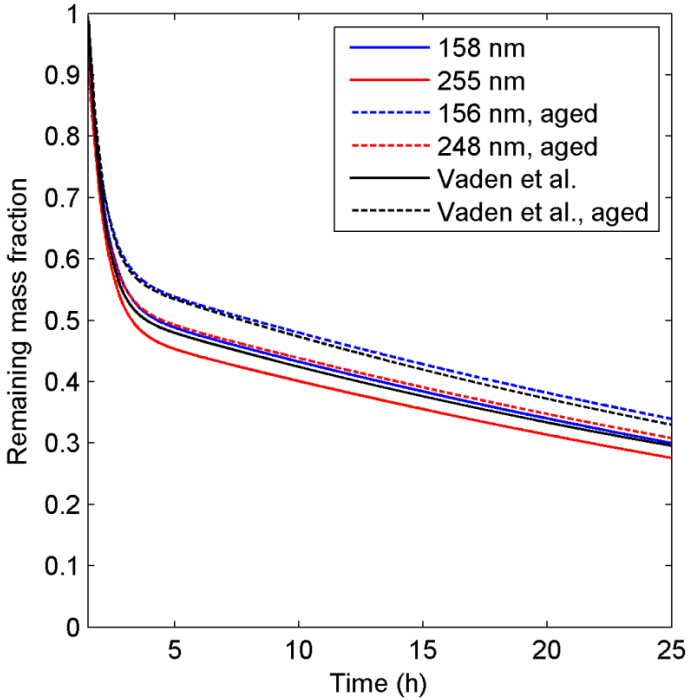

Fig. 11. Modelled and measured (Vaden et al., 2011) evaporation loss rates for semi-solid tar like particles ($D_{0,\mathrm{monomer}} = 5 \times 10^{-17}\,\mathrm{cm^2\,s^{-1}}$ and $D_{\mathrm{oligomer}} = 0\,\mathrm{cm^2\,s^{-1}}$). In the model we included oligomerization by reactive uptake of pinonaldehyde in the particle surface layer (Reactions R1b and R2b and Eq. 33) ($k_\mathrm{f} = 3 \times 10^{-15}\,\mathrm{cm^3\,molecules^{-1}}$ and $k_\mathrm{d} = 3/2\,\mathrm{h^{-1}}$) and bulk phase oligomerization between C922OOH and C921OOH ($k_\mathrm{f} = 10^{-23}\,\mathrm{cm^3\,molecules^{-1}}$ and $k_\mathrm{d} = 1/22\,\mathrm{h^{-1}}$).

ACPD
14, 769–869, 2014

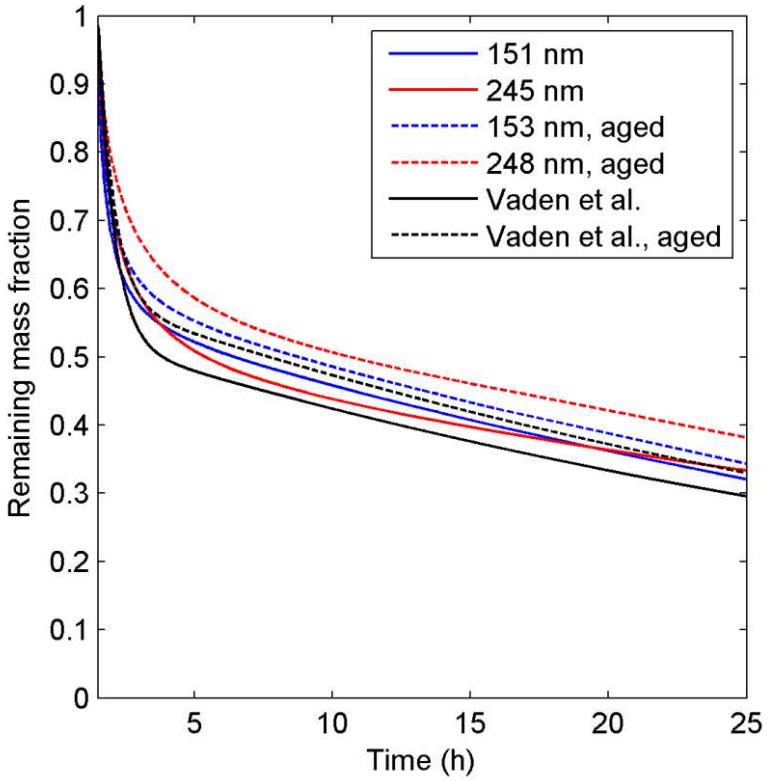

Fig. 12. Modelled and measured (Vaden et al., 2011) evaporation losses for particles composed of ~50 mass % oligomer SOA and with $D_{0,\mathrm{monomer}} \approx 10^{-14}\,\mathrm{cm^2\,s^{-1}}$ and $D_{0,\mathrm{dimer}} \approx 7 \times 10^{-15}\,\mathrm{cm^2\,s^{-1}}$. The results are given both for fresh and aged particles with a diameter of ~150 nm and ~250 nm, respectively.

ACPD
14, 769–869, 2014

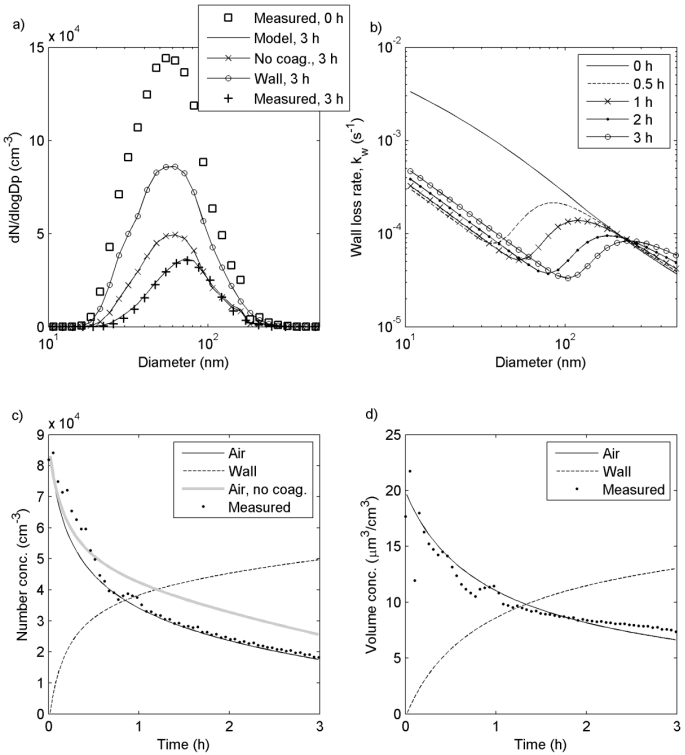

Fig. 13. Modelled dry deposition and coagulation losses of (NH4)2SO4 seed aerosol particles in the Lund University 6 m^3 Teflon chamber. We used a friction velocity of 0.05 $m\,s^{-1}$ and a mean electrical field strength of 50 $V\,cm^{-1}$. The chamber volume loss rate was set to 0.8 $m^3\,h^{-1}$. The model results gives both the particle concentrations in the air (with or without coagulation) and on the particle walls. Figure **(a)** shows the modelled and measured particle number size distributions, **(b)** effective wall loss rates (modelled), **(c)** number concentration and **(d)** volume concentration.

ACPD
14, 769–869, 2014

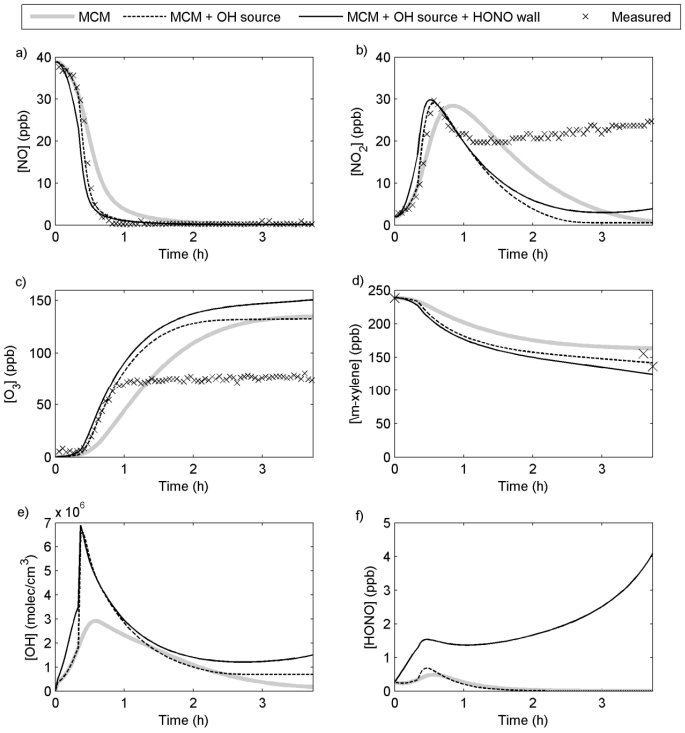

Fig. 14. Modelled and measured gas phase concentrations from the 2 *m*-xylene oxidation experiment from Nordin et al. (2013). **(a–d)** gives the modelled and measured NO, NO_2, O_3 and *m*-xylene concentration, respectively. **(e)** and **(f)** shows the modelled OH and HONO concentrations. The model results are from simulations with: (1) the original MCMv3.2 gas phase chemistry, (2) with MCMv3.2 gas phase chemistry and an artificial OH source of $10^8\,cm^3\,s^{-1}$, and (3) with MCMv3.2 gas phase chemistry, the artificial OH source and wall emissions of HONO.

ACPD
14, 769–869, 2014

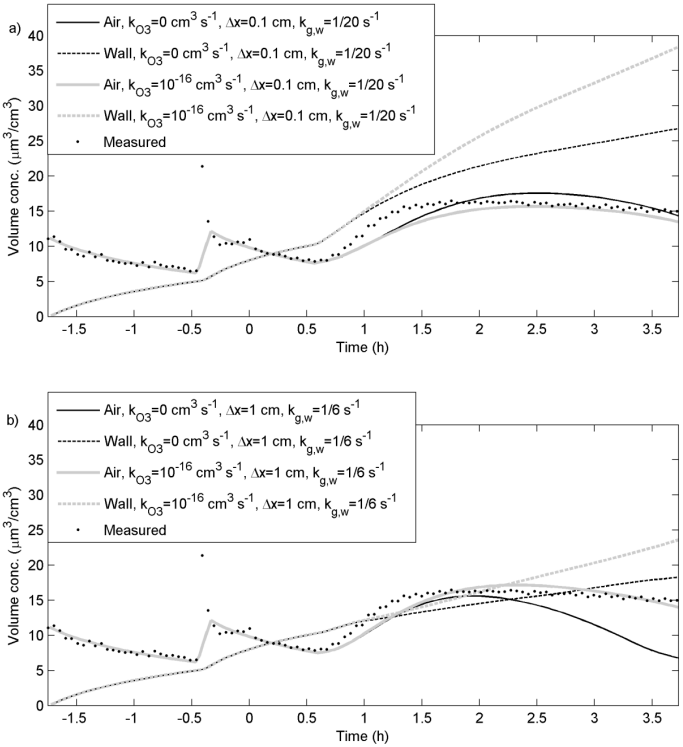

Fig. 15. Modelled and measured volume concentrations of (seed aerosol + SOA coating) during the *m*-xylene oxidation experiment by Nordin et al. (2013). The model results are given both for the particles in the air and for those that have deposited on the chamber walls. The results in **(a)** are from simulations with a laminar layer width (Δx) of 0.1 cm adjacent to the chamber walls and a first order loss rate from the near wall gas phase to the walls ($k_{g,w}$) of $1/20\,s^{-1}$. The results in **(b)** are from simulations with a Δx of 1.0 cm and a $k_{g,w}$ of $1/6\,s^{-1}$. The figures show both the results from simulations without or with heterogeneous reactions between O_3 and unsaturated organic compounds ($k_{O_3} = 10^{-16}\,cm^{-3}\,s^{-1}$ and $D_{0,O_3} = 10^{-8}\,cm^2\,s^{-1}$).

ACPD
14, 769–869, 2014

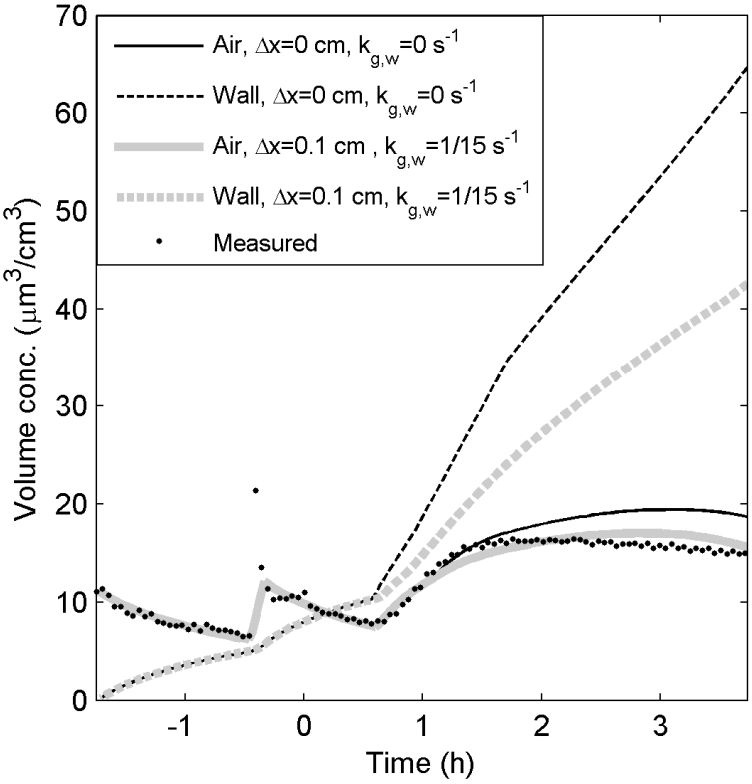

Fig. 16. Modelled and measured volume concentrations (seed aerosol + SOA coating) during the *m*-xylene oxidation experiment from Nordin et al. (2013). The model results are from simulations with relative rapid ($k_f = 10^{-22}$ cm^3 s^{-1}) peroxyhemiacetal (Reaction R1) and hemiacetal (Reaction R3) formation, $\Delta x = 0$ or 0.1 cm and $k_{g,w} = 0$ or $1/15\,s^{-1}$. The model results are given both for the particles in the air and the particles deposited on the chamber walls.

ACPD
14, 769–869, 2014

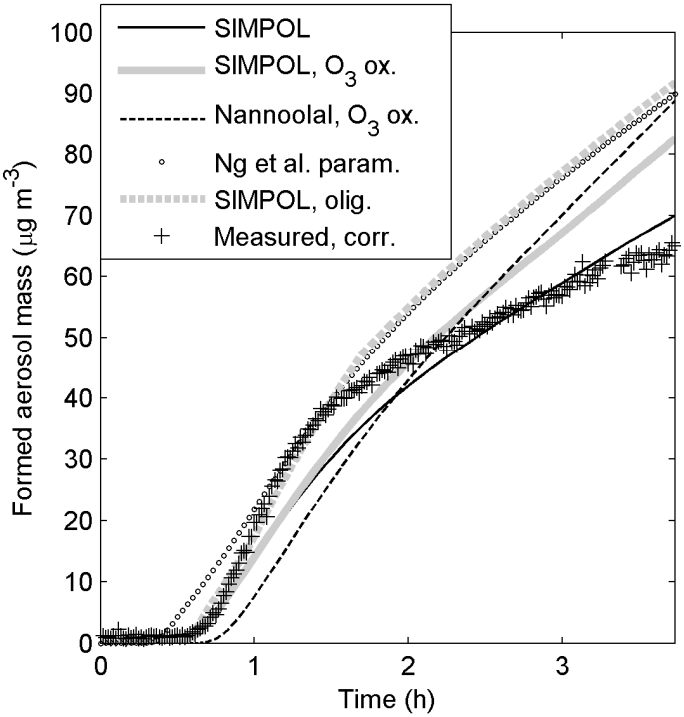

Fig. 17. Modelled and measured (wall loss corrected) SOA mass during the *m*-xylene oxidation experiment by Nordin et al. (2013). The model results are from simulations without wall losses to the chamber walls. The simulations were performed with the SIMPOL vapour pressure method without or with heterogeneous reactions between O_3 and the unsaturated organic compounds ($k_{O_3} = 10^{-16}\,cm^{-3}\,s^{-1}$ and $D_{0,O_3} = 10^{-8}\,cm^2\,s^{-1}$), the Nannoolal vapour pressure method and heterogeneous reactions between O_3 and the unsaturated organic compounds, the semi empirical parameterizations from Ng et al. (2007), and the SIMPOL vapour pressure method and peroxyhemiacetal (R1) and hemiacetal (R3) dimer formation ($k_f = 10^{-22}\,cm^3\,s^{-1}$).

ACPD
14, 769–869, 2014